Contribution to the design and development of hybrid Thermal-Vibrational Piezoelectric Energy Harvester

Neetu Kumari

To cite this version:

Neetu Kumari. Contribution to the design and development of hybrid Thermal-Vibrational Piezoelectric Energy Harvester. Thermics [physics.class-ph]. Université Bourgogne Franche-Comté, 2021. English. NNT : 2021UBFCD027 . tel-03359742

HAL Id: tel-03359742
https://theses.hal.science/tel-03359742

Submitted on 30 Sep 2021

THÈSE DE DOCTORAT DE L'ÉTABLISSEMENT
UNIVERSITÉ BOURGOGNE FRANCHE-COMTÉ
PREPARÉE À L'UNIVERSITÉ DE FRANCHE-COMTÉ

ÉCOLE DOCTORALE N°37
SCIENCES PHYSIQUES POUR L'INGÉNIEUR ET
MICROTECHNIQUES

Doctorat en Sciences pour l'Ingénieur

PAR

Neetu Kumari

Contribution au développement de récupérateurs d'énergies hybrides thérmo-vibrationnelles

Thèse présentée et soutenue à Besançon, le 15 Avril 2021
devant le jury composé de :

Thibaut Raharijaona	Rapporteur	Professeur, ENIM-Université de Lorraine, Metz
Frédéric Giraud	Rapporteur	MCF HDR, Université de Lille, Lille
Skandar Basrour	Examinateur	Professeur, Univ Grenoble-Alpes, Grenoble
Ausrine Bartasyte	Directrice de thèse	Professeure, UBFC, Besançon
Micky Rakotondrabe	Co- directeur de thèse	Professeur, ENIT-INPT, Tarbes

Doctoral Thesis of the University of Bourgogne Franche-Comté
Prepared at University of Franche-Comté

DOCTORAL SCHOOL N° 37
ENGINEERING SCIENCES AND MICROTECHNOLOGIES

Doctorate in Engineering Sciences

By

Neetu Kumari

Contribution to the design and development of hybrid Thermal-Vibrational Piezoelectric Energy Harvester

Thesis defended publicly on 15 April 2021, at Besancon
Composition of jury:

Thibaut Raharijaona	Reviewer	Professor, ENIM-Université de Lorraine, Metz
Frédéric Giraud	Reviewer	MCF HDR, Université de Lille, Lille
Skandar Basrour	Examiner	Professor, Univ Grenoble-Alpes, Grenoble
Ausrine Bartasyte	Thesis Director	Professor, UBFC, Besançon
Micky Rakotondrabe	Thesis Co-supervisor	Professor, ENIT-INPT, Tarbes

Contents

List of Figures

List of Tables

Acknowledge

Firstly, I would like to express my sincere gratitude to my advisor Prof. Micky Rakotondrabe *for the continuous support during my Ph.D. study and related research, for his patience, motivation, and immense knowledge. His guidance helped me in all the time of research and writing of this thesis. I could not have imagined having a better advisor and mentor for my Ph.D. study.*

Besides my advisor, I would like to thank the thesis director Prof. Ausrine Bartasyte and my jury members Prof. *Thibaut Raharijaona, Prof. Skandar Basrour, and Dr. Frédéric Giraud, for their insightful comments and encouragement, but also for the hard questions which incented me to widen my research from various perspectives.*

My sincere thanks also goes to Prof. Mickael Lallart, *Prof.* Paul Muralt, *and Dr. Nabil Bencheikh, who provided me an opportunity to join their teams as visiting researcher during my secondments, and who gave access to the laboratory and research facilities. Without their precious supports it would have not been possible to conduct this research. Thanks to my fellow lab mates Munir, Fawzia, Abbas, Kejun, Ishamol, Giacomo, Miereme and Sondes for the stimulating discussions, and for all the fun we have had in the last three years and for all those amazing brainstorming discussions. In particular, I am grateful to* Patrick Rougeot and Joel Agnus for all the help in the fabrication process and taking out time *by going out of their way to support my research work.*

Finally, I would like to acknowledge with gratitude, the support and love of my family – my parents, Maa and Papa, my brother Sonu, my sisters Nisha and Manjula and all my friends Mudit, Atul, Dipika Akanksha, akshma and Sakshi di. They all kept me going.

To you shibesh without you it would not be possible thank you for constantly listening to me rant and talk things out, for cracking jokes when things became too serious, thankyou for the unconditional love and support throughout the entire thesis process and every day.

“To you papa thank you for teaching me nothing is impossible when you believe”.
What do I owe my father? EVERYTHING

“Henry Van Dyke”

1. Introduction

This work is focused on Hybrid energy harvesting based on lead-free materials exploiting both piezoelectric and pyroelectric effects. To this aim, we explore the use of PVDF polymer, a lead-free piezoelectric single crystal Lithium Niobate and shape memory alloys for thermal and vibrational energy harvesting applications. First, we discuss current advancements in energy harvesting technologies as well as their future scope. A brief description is provided for all the sources of energy available for harvesting in our environment. Special attention is given to the functioning principles of pyroelectric and piezoelectric materials. A concept of hybrid energy harvesting, utilizing three different materials, is introduced. Here, we propose the coupling of piezo- / pyroelectric material and shape memory alloy. We noticed that the pure pyroelectric voltage is combined with generated piezoelectric voltage, induced by shape memory alloy transformation. An individual study is conducted for the piezo- and pyro effect. After that, the coupled piezoelectric and pyroelectric effects were studied for the same prototypes. The heat transferred from the heat source determines two effects. The thermal behavior was simulated by the finite element method using COMSOL multiphysics. Two magnets were incorporated in the system to increase piezoelectricity as the pyroelectric response dominated the piezoelectric response in low frequency.

Furthermore, a new concept has been introduced for hybrid piezoelectric, pyroelectric energy harvesting based on the Joule-Thomson effect and working at a constant temperature. Keeping in mind the real-time scenario, the device's concept is presented here along with the FEA simulation results, which show that if an automobile temperature reaches a constant value, there will be no pyroelectric energy harvesting possible. We can create an artificial environment that will be able to create a temporary temperature gradient. A model has been successfully established. Finally, we introduced a concept for an electrical circuit by which we can harvest energy from the hybrid system and power sensors in automobiles. Here we focused on the pyroelectric and piezoelectric inputs. Both of these effects work on two very different frequencies, hence a non-linear technique of electrical circuit called SECE has been used, by which this implementation can be possible. A model of the circuit has been successfully established and we designed a MATLAB based algorithm to verify the theoretical model. This work's results concern a wide range of applications, especially modern autonomous wireless sensors, and Internet of Things objects, with a low profile, high mechanical flexibility, and low maintenance cost.

1.1 Overview of the Project

Over the years, we have seen considerable interest in technology; it all started increasing since the end of the 20th century, where the first time concept of ubiquitous computing was introduced [1]. We know that the term computing involves activity where we use a computer to manage the process and communicate information, in a way it includes development both in hardware as well as software but that does not limit it for personal computers. On the contrary, by this technology we can use any device in any format, anytime, anywhere. It gives us the freedom to operate it whenever we want in the form called "smart" devices. Nowadays, we can find that there are many smart devices connected to the Internet of Things (IoT) in the market. We know that an IoT consists of web-enabled intelligent devices that use embedded systems, such as processors, sensors, and communication hardware, to collect, send and act on data they acquire from their environments. We have to mention that Most IoT devices do share the data they collect by connecting to an IoT gateway or other edge device where information is either sent to the cloud to be analyzed or analyzed locally and efficiently [2].

Here in this project named ITN-ENHANCE Network grant number 722496 [3], we are working on energy harvesting devices based on lead-free materials that can be used to power sensors in automobiles and useful in IoT.

The general focus is on "Piezoelectric Energy Harvesters for Self-Powered Automotive Sensors based from advanced Lead-Free Materials to Smart systems," which comes under Initial Training Network, the critical topics of the project include the development of energy harvesters compatible with MEMS technology and able to power wireless sensors. Applied to automobiles, such technology will allow for 50 kg of weight saving, connection simplification, space reduction, and reduced maintenance costs -all significant steps towards creating green vehicles. The project simultaneously aims to work on hybrid energy harvesting exploiting thermal, vibration, electromagnetic, and solar energies as these energies are available in abundance inside automobiles.

The ENHANCE project's main objective is to tackle the above focus through a multidisciplinary group of researchers from different scientific fields. The central target is to overcome the present limitations of micro energy harvesters by striving the obtention of high-power density and stabilized output voltage in 1-3 V range for powering autonomous sensors working in temperature ranges from room temperature (RT) to 600 °C in vehicles, the global goal of the project is depicted in Figure 1.1.

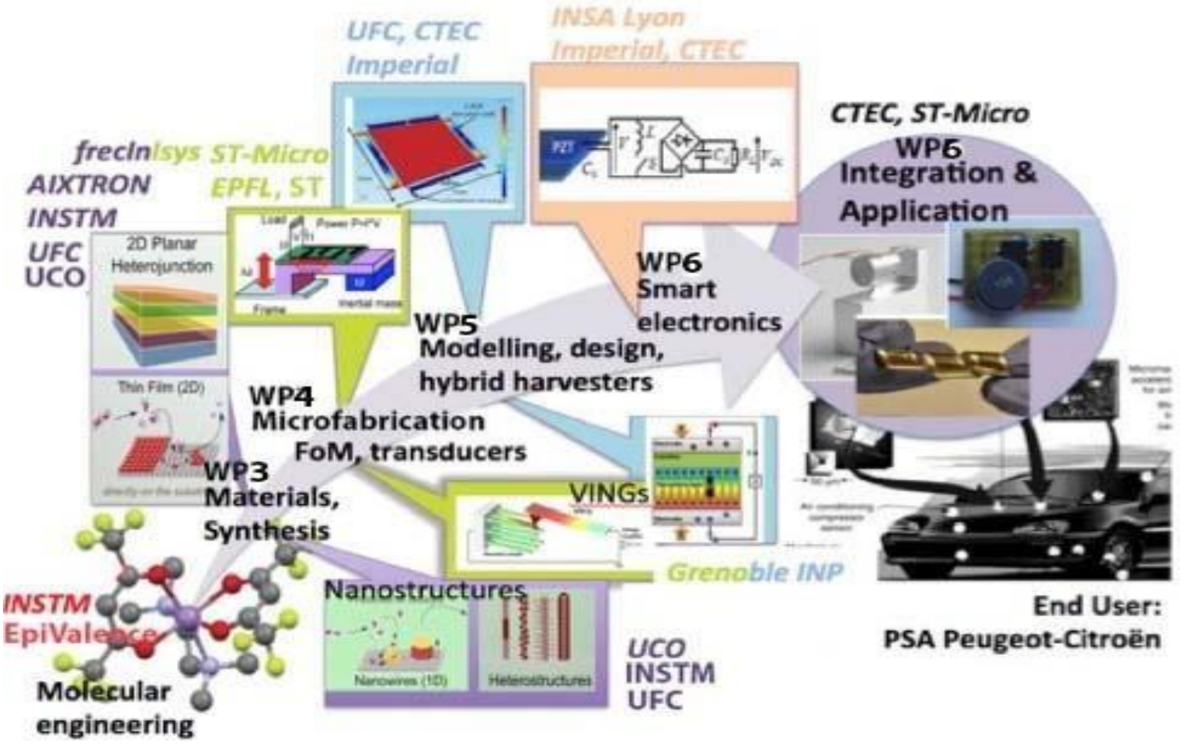

Figure 1. 1 Multidisciplinary approach in the ITN ENHANCE project [3]

1.2 Research Objectives

Hybrid energy harvesting is one of the most prominent research fields. As we can see, an abundance of wasted energies of different forms is present in our surroundings. Among them, vibrational and thermal energies are the most common in which we are interested in this following research as these energies are readily available in automobiles. For example, we can see that due to our day-to-day activities, we use so many electrical appliances that release heat as a by-product, e.g., the heat outside of refrigerators and personal computers. This heat energy, which goes into waste, can be harnessed and converted into a useful form through thermal energy harvesting. The same applies to the vibrational energy since there are several sources of kinetic energy that can be seen easily in our nearby surrounding, for e.g., human walking is one of the most common examples which can be harvested.

This research aims to achieve hybrid thermal-vibrational energy harvesting using a piezoelectric and pyroelectric material. Several studies have been conducted on piezoelectric and pyroelectric energy harvesting devices. Few reviews are being carried out on exploiting the piezo and pyro effect together, and even less for hybrid system based on lead-free materials.

This thesis studies and proposes a new approach of hybrid energy harvesting and carries out modelling and experiments on the designed device. Simple structure of various shapes depending on our requirements are designed for that.

The research work will focus on the following several objectives:

- The state-of-the-art of thermal and vibrational energy harvesting review and summarize.
- The investigation on the behavior of heat transfer distribution and vibration behavior by the finite element method.
- The building of a model to estimate the performance of the harvesting mechanism.
- The development of a hybrid harvester using piezo- and pyro-electric effects with a simple structure.
- And the Development a hybrid harvester using piezo- and pyroelectric with an electrical interface that could work in both high and low-frequency range.

This work's novel contribution is to present a newly designed structure for a multiresonant energy harvester. Moreover, a concept is offered for a hybrid harvesting mechanism that can work at a constant temperature. Finally, an algorithm is provided for the electrical circuit based on non-linear techniques. It can work on two different frequencies and can simultaneously harvest energy from various forms of energy.

1.3 Thesis Structure

This thesis composed of 6 chapters including this general introduction. The writing structure is a series of processes, which provides in-depth knowledge of the subject, and which is constantly improved based on the experience gained in the previous chapter. The outline of each one is as follows:

Chapter 1 briefly introduces the framework for this project and discusses the main objectives.

Chapter 2 gives a thorough literature review of energy harvesters. It provides a detailed overview of all the different energy sources that can be harnessed and present in our environment. An extensive survey of thermal and vibrational energy, the main objective of this research, is conducted. A thorough review of hybrid energy harvesting is provided, along with that relevant examples are presented.

Chapter 3 describes the first initial design concept of hybrid thermal energy harvesting using a Shape Memory Alloy beam (Nitinol) and Lithium Niobate ($LiNob_3$). Experiments are conducted based on this concept, and the results are presented. Heat behavior is simulated by the finite element method, and a thermal imaging camera captures the thermal image.

Chapter 4 examines the hybrid mechanism based on the results of the two effects in the initial prototype. A closed system concept is introduced, which works at a constant temperature and able to utilize both the piezo-pyro effects. Experiments are conducted, and conclusions are obtained. Comparisons of simulation and experimental results are presented.

Chapter 5 deals with the design and test of the used harvesting electrical circuit concept, the SECE circuit.

Chapter 6 summarizes the work in this thesis and provides suggestions for future work on this project.

2. Literature Review

This chapter presents a literature review of the state-of-the-art in energy harvesting. Given that, this research focuses primarily on hybrid thermal energy harvesting based on piezoelectric and pyroelectric material.

The review starts with an overview of the standard energy harvesting system first. Then, an extensive description is provided on the mechanism of hybrid energy harvesting devices. Afterwards, the following sections describe vibrational and thermal energy harvesting in detail. Starting with the thermal energy harvesting, the pyroelectric effect broadly described along with the thermodynamic cycles for the pyroelectric conversion is first presented. Thereafter, vibrational energy harvesting is introduced, in which different vibrational energy sources are discussed as well as some vibration energy techniques like electrostatic, electromagnetic, and piezoelectric. Finally, a thorough description of hybrid energy harvesting is presented along with the Survey on the hybrid system, their mechanism, and the materials used in them. The chapter ends with a perspective towards hybrid piezo-pyro harvesting based on lead-free materials, which is the target of the thesis.

2.1 Energy Harvesting from Ambient source

Ambient energy harvesting is also referred to as energy scavenging or power harvesting; it collects energy from the environment. This energy is then converted into electrical energy and stored for use in electronic or electrical devices and appliances. There are plenty of sources available for energy harvesting, including solar energy (which can be obtained from the sunlight), mechanical energy (which is present in the form of vibration and mechanical strain/stress), thermal energy (which can be easily found from the heat furnaces, heaters, friction sources, and body heat), and not to forget the radiofrequency energy (RF) (energy from wireless and broadcast networks like Wi-Fi, 2G, 3G, 4G, and Digital TV)[4].

2.2 Overview of Energy Harvesting

2.2.1 Energy sources

We know that our environmental problems are increasing due to the excessive use of fossil fuels; as they burn, they release nitrogen oxides into the atmosphere, contributing to smog and acid rain formation. The solution to this kind of problem is to use renewable energies, which can reduce our dependency on these fossil fuels and provides several valuable benefits. However, we have to keep in mind while harnessing these renewable energies, which kind of source are the most appropriate, how it will affect the mechanism, and which the one suitable for our application. This section provides an overview of energy sources.

2.2.1.1 Solar Energy

Solar energy harvesting consists of a solar cell or a photovoltaic cell; solar energy is the cheapest energy source present in our environment, readily available. Thanks to the photovoltaic effect [5], solar energy is converted into electricity.

When there is sunlight, the solar cell will absorb the light energy in the semiconductor, consisting of two layers, p-type and n-type, and transportation of charges to electrodes. This work of charge transportation is a critical factor as it decides the semiconductor's voltage generation capability. Therefore, while choosing the material, we must keep in mind the material's work function as it is a crucial parameter for high-energy conversion efficiency. If the material cannot transport charges efficiently, it will impact the device's performance [6].

The conversion efficiency (η_{solar}) of the solar cell is one of the standards in evaluating the output performance of solar cells. The conversion efficiency can be derived by

$$\eta_{solar}(\%) = \frac{P_{max}}{P_{in}} = \frac{V_{OC} \times J_{SC} \times FF}{P_{in}} \times 100 \tag{2.1}$$

Where P_{max} is the maximum output performance, P_{in} is input solar energy, V_{OC} is the open-circuit voltage, J_{SC} is the short-circuit current, and FF is the fill factor. The FF is the maximum power from the solar cell achieved from the I–V curve. In recent years, solar cells' energy conversion efficiency has drastically improved thanks to the materials' recent development, and now it reached a few percent to over 40%.

2.2.1.2 Thermal energy

Thermal energy is one of the most effortlessly available energy presents in our surroundings for harvesting. Thermal energy harvesters can harness energy from both waste and natural heat. One of the most promising advantages of using these thermal energy harvesters is low operating costs and maintenance costs compared to the ordinary heat engines [7].

Thermoelectric generators are typically used to exploit spatial temperature gradients as a continuous source. On the other side, Pyroelectric materials are known for harvesting temporal temperature gradients. By the use of fluid pumping in between the cold and hot sources, the temperature gradient can be changed into a temporal temperature variation [8].On the other hand, by using a pyroelectric element that can mechanically oscillate between hot and cold sources [9] one can also harvest thermal energy. However, the thermoelectric generator's main challenge is to maintain a constant temperature on one side of the generator. If we could keep the temperature variations at one end, then harvesting can be possible [10].

An abundance of waste heat energy comes out from automobile and electrical appliances and present in the form of a by-product in our environment. Seebeck effect is one of the most studied effects, which describes the conversion of heat energy into electricity. Carnot efficiency is used to calculate the theoretic power output, which depends on the temperature difference between the hot and cold side of the device.

2.2.1.3 Radio Frequency

Radio Frequency energy comes from electronic devices such as TV signals, satellites orbiting earth, wireless radio networks, Wi-Fi, and cell phone towers, which produce a high electromagnetic field. Energy generated by these electrical appliances can be stored for powering sensors or electric circuits[11].However, Ambient RF sources have low power density than the other ambient energy sources like solar and vibrational; nevertheless, RF signals have the advantages of being reasonably ubiquitous, and the associated energy is radiated continuously.

2.2.1.4 Wind Energy

Wind energy is another source for harvesting application. When harvested using powerful wind turbines, this wind flows or motion energy can become electricity for a large scale area [12].
Wind energy is an underutilized renewable energy source. Many people are familiar with the idea of wind power but not quite sure exactly what it is or how it is used. One can say that wind power is the use of the wind's kinetic energy to generate electricity or mechanical power. One of the oldest known processes for using wind energy is windmills.

2.2.1.5 Mechanical Energy

Mechanical energy is one of the most common and used energies present in our surroundings; however, it can be harvested from various forms such as vibrations [13], fluid flows [14], direct forces [15], and sound [16].

Mechanical sources are one of the promising alternatives known to harvest energy where the vibration source is comparatively large, e.g., ocean waves. Here we can see the vibration magnitude is high. In contrast, human motion vibration in comparison to this is small.

Many conversion techniques are present by which the vibration energy can be converted into electrical energy, for instance : magnetic field, electrostatic, strain, or piezoelectric materials [17]. The use of piezoelectric materials and their applications has been widely investigated. Since this will be the focus of this research, a thorough introduction to vibration energy harvesting will be given in section 2.4.

2.2.2 Energy harvesting systems

The energy harvesting system's main aim is to convert the present energy in our surroundings into a usable form, which can be used to power any electric appliances. Energy sources present in any state, e.g., fluid flows, direct forces, vibrations, static electricity, thermal energy, electromagnetic radiation (light, radiofrequency), etc., can be used and converted. In the last few years, it has been noticed that a lot of work and development have taken place in low-power electronics and wireless sensor networks. It has become an exciting field for many researchers and industries as well, where the main objective is to harvest energy to power specific applications. Moreover, these energy harvesting systems gives an alternative power source for electronic devices were replacing the battery is believed to be complicated: for instance, an electronic device like a pacemaker which is placed inside the human body, or wireless sensor networks located in extreme conditions locations and places. However, energy harvesting helps us keep our environment green. It uses only renewable sources of energy and eliminates harmful chemical batteries from our system. Fig. 2.1 shows a block diagram of a generic energy harvesting system. The first block, energy source, is an initial form of energy, which can be any energy appropriately.

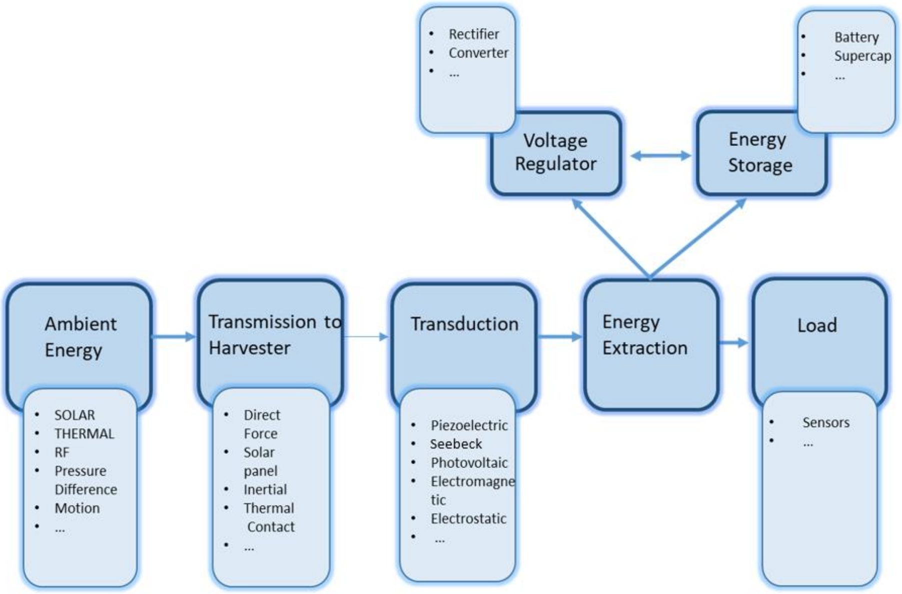

Figure 2. 1 Block diagram of a generic energy harvesting system.

The bridge between the source and the actual conversion mechanism is described in the second block. The transducer that is the generator of energy that converts the environment energy into electricity. The transduction block represents the circuitry to maintain the transducer in its optimum-energy conversion. We can say particularly in this stage, AC can be converted to DC via a rectifier. The regulator is used to convert transitory energy of converts to more stable voltage to charge lager voltage simultaneously supply loads requiring stable voltage which is usually in the range of 1.8-3.3 V for the embedded systems. Energy storage unit is used to store the converted energy and can be of many types, e.g., a battery or super-capacitor. Finally, the stored energy is applied to a specific load.

Regarding energy harvesting systems and devices, Hongye Pan et al. [18] worked on a portable wind energy harvester system based on the S-rotor and H-rotor for self-powered applications in high-speed railway tunnels, as shown as Figure 2.1. In this research, their focus was on harvesting the wind energy that is present in the tunnel when a high-speed train passes by. The S-rotor harvests natural wind energy; on the other hand, the H-rotor is used to gather the piston wind energy whenever a high-speed train passes through the tunnel. Super-capacitors in the power storage module is used to store the electrical energy. They reported a maximum electrical power output of 107.76 mW, and a maximum efficiency of 23.2% was demonstrated in the test.

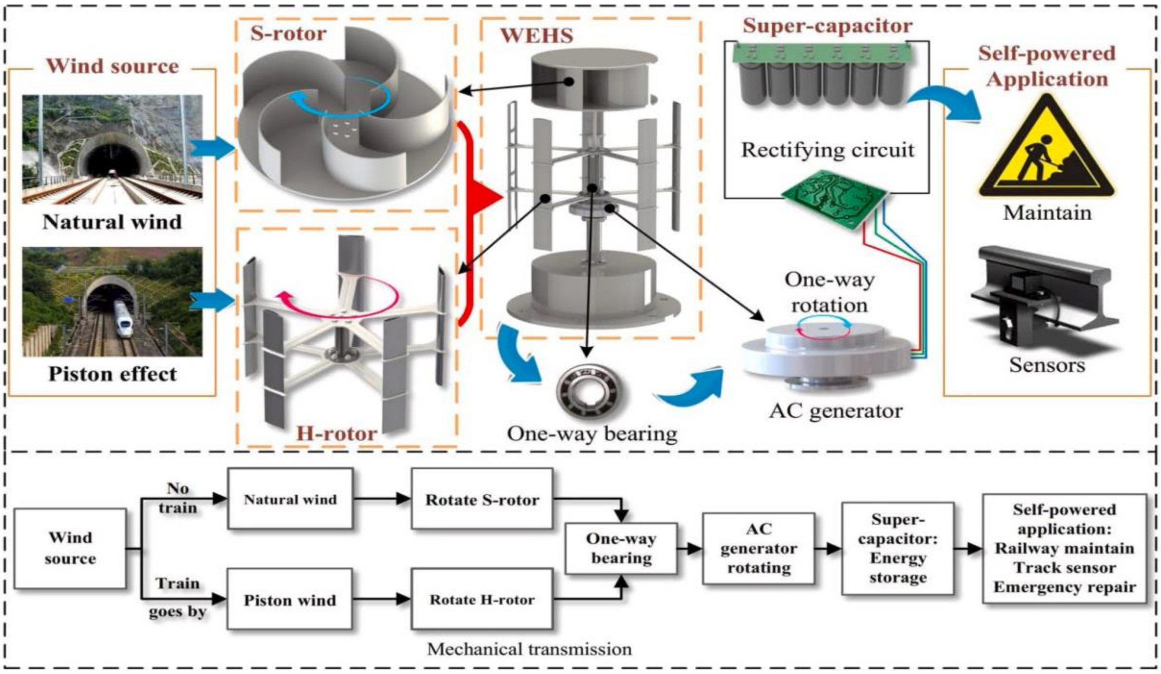

Figure 2. 2 Block diagram of the wind energy harvesting system [18].

Similarly, to wind energy, solar energy is also very knowledgeable in the field of energy harvesting as it can be found easily. Many researchers studied this field and came up with innovation in solar energy harvesting systems. For instance, Himanshu Sharma et al. [19] proposed a new solution by which the efficiency of the solar energy harvesting system is increased based on the maximum power point tracking (MPPT) for WSN nodes. The research aim was to increase the overall harvesting system efficiency, which depends upon Solar Panel Efficiency, the maximum power point tracking controls, the DC-DC converter efficiency and the rechargeable battery efficiency. See Figure 2.3 with the provided simulation results, it can be seen that the designed solar energy harvesting system had 96% efficiency (η sys).

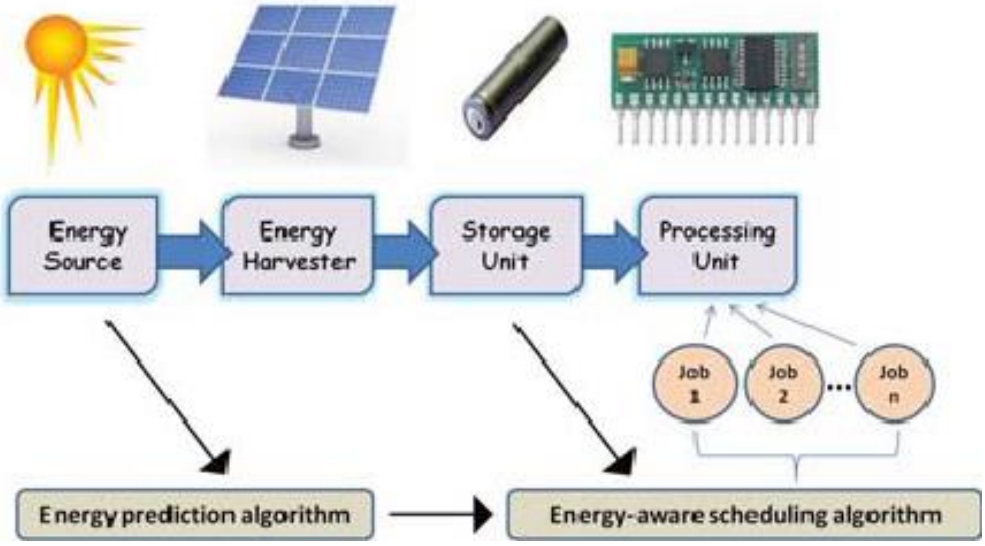

Figure 2. 3 Block diagram of a solar energy harvesting system [19].

Regarding energy harvesting systems based on Radiofrequency, we can see in recent years that more and more research has been carried out in this relative field, which turns out to be a promising one. Guo Ming Sung et al. [20] worked on the smart Integrated Circuits for Powering Wireless Sensor Networks and energy harvesting where the source of energy with Radiofrequency see Figure 2.4 . In their work, they presented a radiofrequency (RF) energy harvesting integrated circuit (IC) on a small area for powering wireless sensor networks with a wireless transmitter with an industrial, scientific, and medical equipment (ISM) of 915 MHz. In their device, they used an RF-DC rectifier circuit, a six-stage Dickson voltage multiplier circuit. They could prevent the high-voltage breakdown phenomenon from the RF front-end circuit by implementing smart voltage protection. Charging current is amplified N times by using a current mirror to rapidly and stably charge a battery in the proposed charger control circuit. With the results presented, the maximum power conversion efficiency of the proposed RF-energy-harvesting IC was 40.56% at an input power of –6 dBm, an output voltage of 1.5 V load of 30 kΩ and a power consumption of 42 µW.

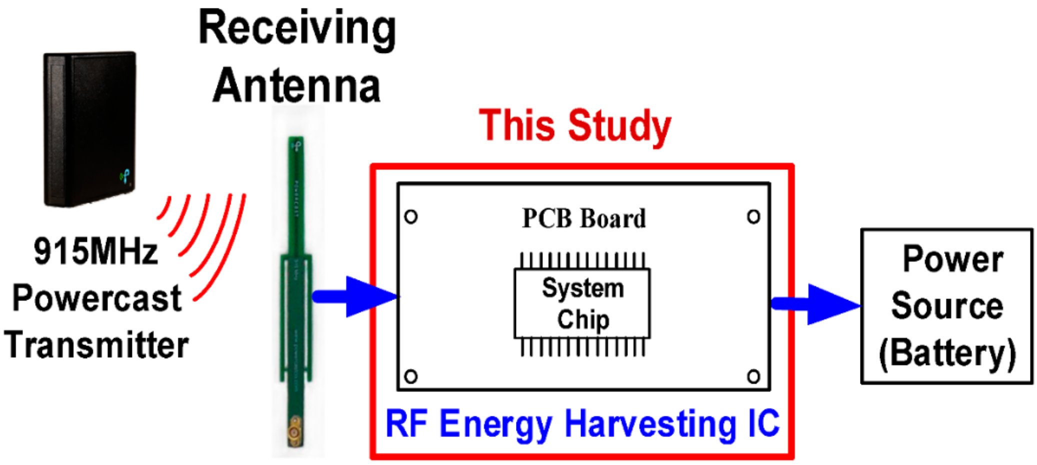

Figure 2. 4 Block diagram of a Radiofrequency energy harvesting system [20]

Electromagnetic Vibration Energy Harvesting (EM-VEH) is a lucrative alternative to batteries as they are cheap and durable. In our environments, an abundance of kinetic energy is available in machinery vibrations or human walking that can be converted into electrical power through energy harvesting techniques. These ambient vibrations are generally broadband, and multi-modal harvesting configurations can be exploited to improve the mechanical-to-electrical energy conversion. However, there is also some challenge present when it comes to the energy conditioning (AC-to-DC conversion) for that since one must have a perfect electric circuit to harvest maximum power in the given conditions, Juan Carlos Rodriguez et al. [21] presented a report on the operation of two practical IoT sensor nodes can be seen in Figure 2.5, continuously powered by the vibrations of a standard industrial compressor, using a multi-modal EM-VEH device, which is then integrated with customized power management.

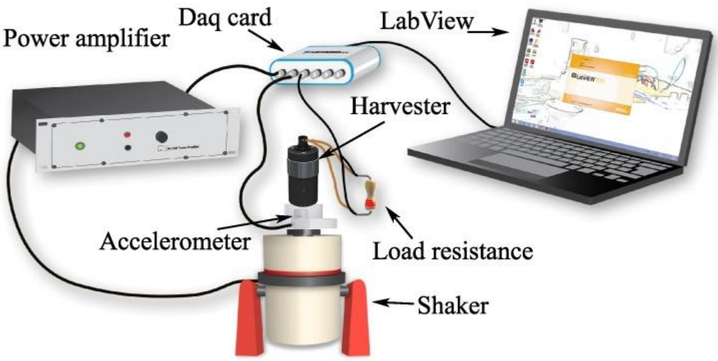

Figure 2. 5 Schematic of the experimental setup for the vibration energy harvesting system [21]

The power management circuit of the developed device provides sufficient energy to receive and transmit data at intervals of less than one minute with an overall efficiency of about 30%. There are many other VEH development afterwards, such as that of Pramod et al.[22], Huidong Li et al. [23] .Hailing Fu et al. [24]; some researchers like Deepesh et al. [25] dipcited in Figure 2.6 worked on Piezoelectric power generation.

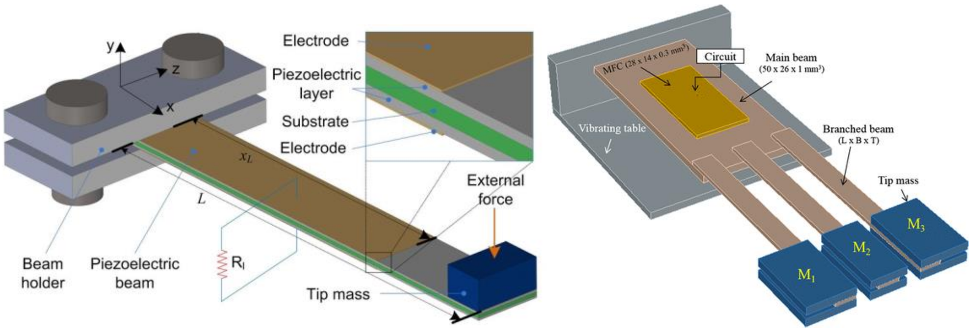

Figure 2. 6 Various piezoelectric beam harvesters [24,25]

Among the sources of vibrational energy, human body has particularly attracted interest. For instance Paradiso, provided a concept of including typical power requirements and potential body locations for energy harvesting [26] and [27] as well as Miere et al.[28] discuss energy harvesting in shoes. In the same period, some patents came upon on this concept by Smalser [29] by Kimura [30].Finally Beeby gave an insight into the different vibration sources available [31]. Whilst an interesting general overviews of the field are given by Mitcheson et al. [32] Du toit et al. [33] and Roundy et al.[34].

Thermal energy generators (TEGs) gain immense demand in recent years as thermal energy harvesting is very popular nowadays due to the growing need to generate energy by renewable means.

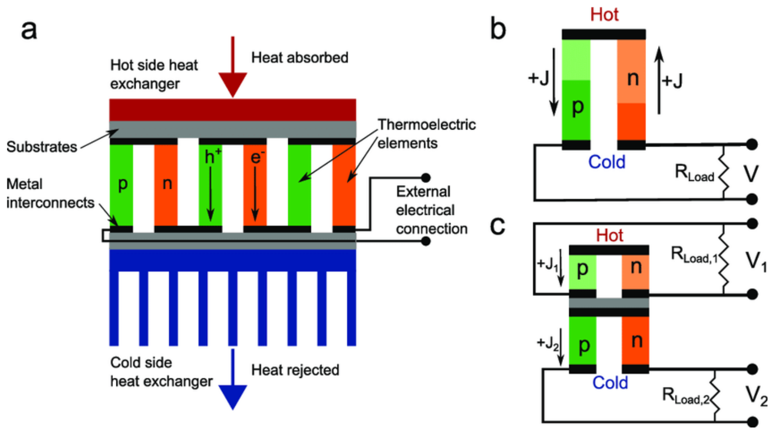

Figure 2. 7 A Schematic representation of thermoelectric energy harvesting system [35]

TEGs can extract maximum power from the available temperature gradient. Lauryn L. Baranowski et al. [35] developed a concept of an "effective thermal conductivity," which encompasses both the Fourier and thermoelectric heat transport within the device. With this concept's help, they were able to do optimization of TEGs and heat exchangers for maximum power production see Figure 2.7.

Other than the TEGs, Thermomagnetic energy harvesting is also a vital part of thermal energy harvesting. In this process, the thermal energy of any stationary heat source can be converted into a magnetic force. Kishore et al. gave an excellent review of this concept [36]. These harvesters' concept uses soft ferromagnetic materials magnetized below a specific temperature, the Curie temperature. Beyond the Curie temperature, we cannot see the magnetization, and the material becomes paramagnetic. Paramagnetic materials show a fragile attraction to an externally applied magnetic field [37]. In the past few years, many research groups have developed harvesters using a soft ferromagnet and a rigid magnet (i.e., permanent magnet) by defining a working condition so that ferromagnet can cross over its Curie temperature. Figure 2.8(a) and 2.9(b) represents a system which works on the principle of self-oscillating harvesters with magnets. Some researches have used a soft magnet along with a piezoelectric material when the soft magnet crosses its curie temperature there will be a change in the force of attraction due to which we can say this vibration will also induce the piezoelectric vibration in the system some of these devices are depicted by Carlioz et al.[38] shown in Figure 2.8 (a) and Chen et al [39] (b) similar work is done by Chun et al. [40] depicted in Figure 2.9(a) .

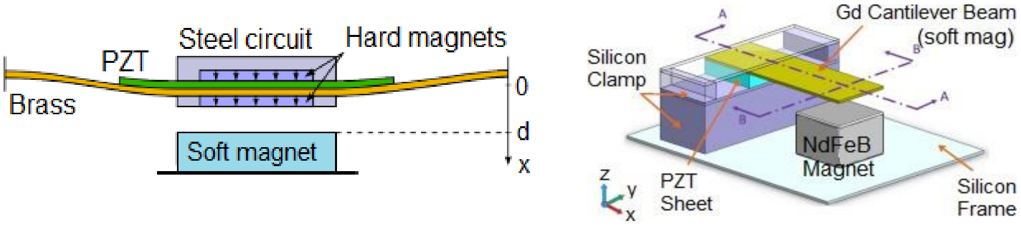

(a) Carlioz *et al.* from [38] (b) Chen *et al.* from [39]

Figure 2. 8 Schematic of the self-oscillating harvesters from Carlioz et al. And Chen et al.

Nevertheless, (b) Gueltig et al. [41] also worked on the thermomagnetic system, which was based on faraday's law. They implemented a magnetic shape memory alloy (Ni-Mn-Ga film) and a hard magnet and attached a pick-up coil at the end of the cantilever. Due to the coil oscillation around the permanent magnet, a time-varying magnetic field was generated.

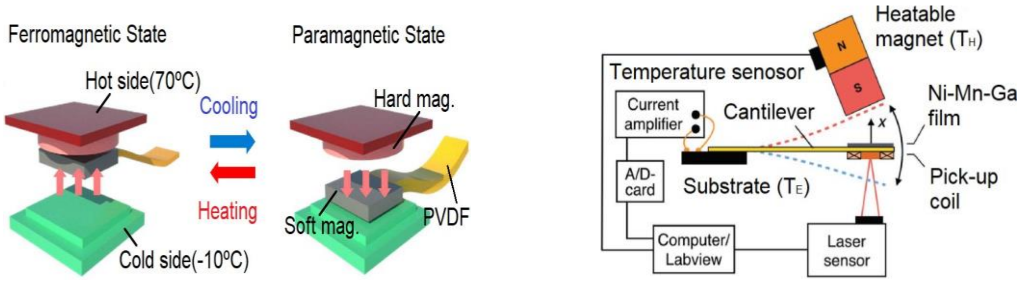

(a) Chun *et al.* from [40] (b) Gueltig *et al.* from [41]

Figure 2. 9 A pictorial representation of the self-oscillating harvesters from Chun et al. and Gueltig et al.

Some research groups also exploited the coupling effect between mechanical energy with thermal energy by incorporating bimetallic materials or shape memory alloys (SMA) in the system. These materials are known to change their shape according to temperature change. The principle of working in bimetallic material depends on the material as it consists of two different alloy layers with a massive difference in coefficient of thermal expansion (CTE). So, whenever there is any thermal load present, it will cause a deformation in the system. Puscasu et al. [42] and Zakharov et al. [43] introduced the concept of thermal energy harvesting devices by implementing bimetallic strip and a piezoelectric (PZT) membrane, as shown in Figure 2.10.

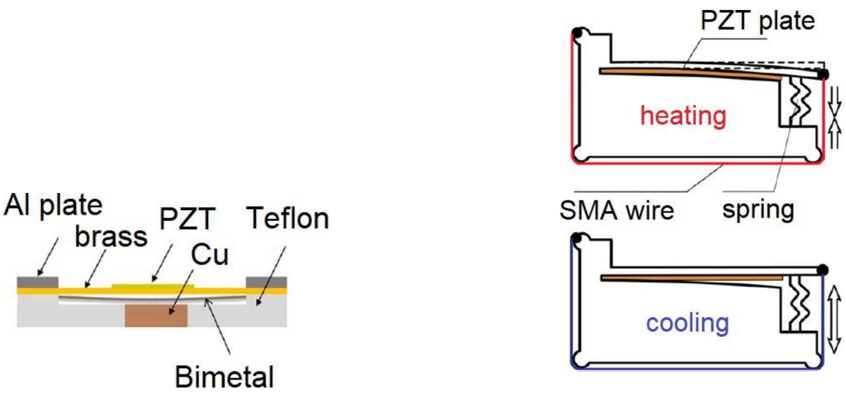

(a) Puscasu *et al.* from [42]   (b) Zakharov *et al.* from [43]

Figure 2. 10 Schematic of the self-oscillating harvesters with (a) bimetal (b) shape memory alloys.

As pyroelectric materials have the principle of working on the temperature difference, they can generate temporary voltage whenever there is a change in the system's temperature. Hunter et al. used a system that consists of a cantilever structure. One layer is the pyro layer, and the other is the substrate. The two layers have different CTE and are in contact with a stationary heat source [44], as shown in Figure 2.11 (a). The cantilever moves away from the heating source once it gets heated and returned to its positions one the cantilever's temperature goes down. This structure is similar to the other once discussed above in Figure 2.8 and Figure 2.9, instead of the piezoelectric effect, we see the pyroelectric effect. Another researcher, Ravindran et al., came up with another innovative idea where he used a thermomechanical-pyroelectric generator, an airtight system with an enclosed cavity, and a bistable membrane [45], as shown in Figure 2.11(b). Due to the temperature variation inside the system, the air gets expanded or contracted because the change in the bistable membrane's shape leads to the generator's oscillation between a heat source and sink.

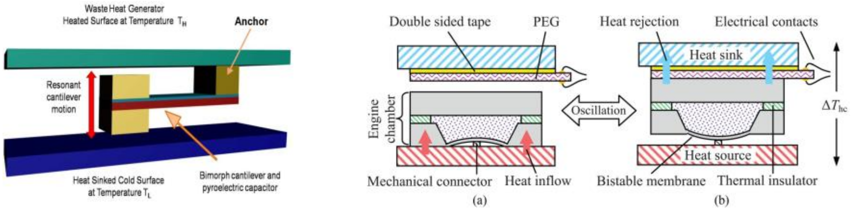

(a)Hunter *et al.* from [44]   (b) Ranvindran *et al.* from [45]

Figure 2. 11 Schematic of the self-oscillating harvesters

2.3 Thermal Energy Harvesting

One of this research's main focuses is the study of thermal energy harvesting mechanism using a pyroelectric material. For that and in order to favour lead-free materials, we will suggest using Lithium Niobate piezoelectric material, PVDF piezoelectric polymer and shape memory alloy. This section begins with the necessary information on heat sources. Then a brief description of the thermoelectric effect is presented. Afterwards a full description of the pyroelectric effect is given along with the thermodynamic cycle used in the pyroelectric conversion.

2.3.1 Heat Source

Heat energy comes from an object or substance whose molecules and atoms are moving faster due to a temperature rise. There are many examples of heat energy in your day to day life; when a stovetop burner is boiling, it is also a heat energy source. Moreover, anything that will be in close contact with the stovetop and get warm will become itself a heat energy sources. Even a hot cup of steaming water contains heat energy. Geothermal energy is a type of heat energy generated and stored beneath the surface of the earth. Nowadays, this type of energy is used to heat homes and buildings; any fire, from the smallest match to the fireplace, to the most significant forest fire ever, contains heat energy.

Even when ice is placed into a glass of water, the water's heat energy eventually melts the ice, meaning the water itself serves as a source of heat energy. If we see in our home, there are radiators or heating systems present which radiant heat energy to warm a house during those long, cold winter months is also a heat source. The most popular one present almost in every home is conventional ovens, which work on convection heat energy, causing the food to become hot and cook is also a heat source.

2.3.2 Thermoelectric effect

The thermoelectric effect is a well-known effect in thermal energy harvesting. In fact, “Thermoelectric effect “term encompasses three effects which are: Seebeck effect, the Peltier effect, and the Thomson effect. The Seeback is usually studied for understanding the mechanism of thermoelectric generation. In this effect, two types of materials: n-type and p-type semiconductors, are present in a thermoelectric generator connected electrically in series but thermally in parallel. These two semiconductors are used to produce electricity directly when their junctions are exposed to a temperature difference (Figure 2.12). Thermoelectric generators work on the concept of making voltage when there is a temperature difference between the hot and cold sides along with that it simultaneously works on the difference of Seebeck coefficients of the two materials [46].

$$V = \int_{T_L}^{T^H} S_1(T) - S_2(T)\, dT \qquad (2.2)$$

Where T_L, T_H are the low and high temperatures, S_1, S_2 are the two materials Seebeck coefficients.

Here, a thermoelectric module is depicted in Figure 2.12 commercially available [47].

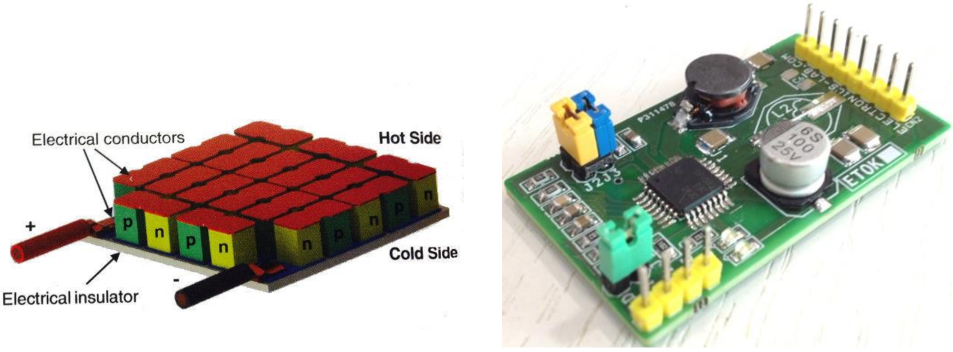

Figure 2. 12 *Left: schematic of a thermoelectric module [46], Right: thermoelectric generator with heat sink, from [47].*

The efficiency of the thermoelectric generator usually depends on the properties of the material. If the material is not a good electrical conductor nor an excellent thermal insulator, then, unfortunately, the efficiency will be low. It is challenging to find a material which is having both these properties together to estimate the thermoelectric property of any material; a figure of merit called ZT is used for that:

$$ZT = \frac{\sigma S^2}{\lambda}\left(\frac{T_H - T_L}{2}\right) \qquad (2.3)$$

Where σ is the electrical conductivity, S is the Seebeck coefficient, and λ is the thermal conductivity. Although theoretically unlimited, in practice, the *ZT* values are close to 1. Figure 2.13 compares *ZT* values for the most commonly used thermoelectric materials. The efficiency increases almost linearly with temperature [48] .

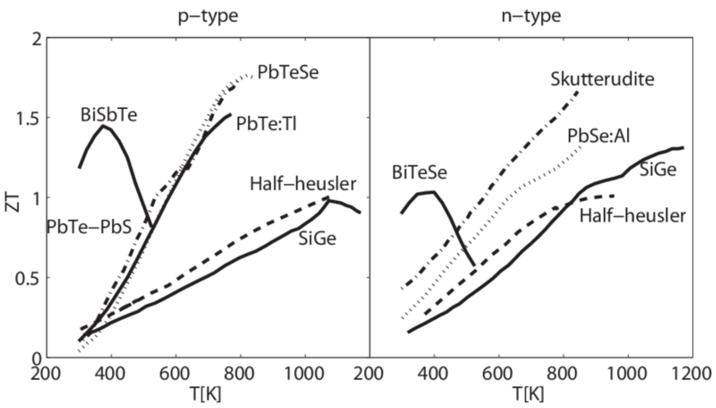

Figure 2. 13 State-of-the-art (2014) comparison of ZT from various materials [48].

There are plenty of advantages of using thermoelectric generators, namely reliability and scalability. In counterpart, their efficiency is low, and the price is relatively high.

2.3.3 Pyroelectric effect

Pyroelectric effect and materials are also used to harvest the thermal energy as described by Sebald et al.[49]; pyroelectric energy harvesting is only possible when there is a temperature gradient in time (i.e. fluctuation) present in the system. In our day to day life, we can find various sources producing wasted heat. For example, machines like computers and radiators are massive thermal energy sources.

Pyroelectricity is the property found in materials that exhibit an electric polarization ΔP when a temperature variation ΔT is applied uniformly. if there is a temporal temperature change, it results in a flow of charges on the material's surface, which is known as pyroelectric current. Such current is defined by.

$$I = \frac{dQ}{dT} = S\lambda \frac{dT}{dt} \tag{2.4}$$

Where Q is the induced charge, S is the electrode surface area, and λ is the pyroelectric coefficient given by:

$$\lambda = \frac{dP_S}{dT} \tag{2.5}$$

Where P_S is the electrical polarization vector [50].

Pyroelectric material is a subgroup of piezoelectric materials, and ferroelectric materials are a subgroup of pyroelectric materials. A relationship is established between these materials and shown in Figure 2.14 [51]. The material structure has an important significance in deciding whether it is a piezo, pyro, or ferroelectric material. Parameters like temperature, stress, or external electric field also play a vital role due to their influence on the crystal symmetry. Lead zirconate titanate (PZT), lead magnesium niobate lead titanate (PMN-PT), and polyvinylidene fluoride (PVDF) are commonly used as energy harvesting material, all of which are classified as ferroelectric materials.

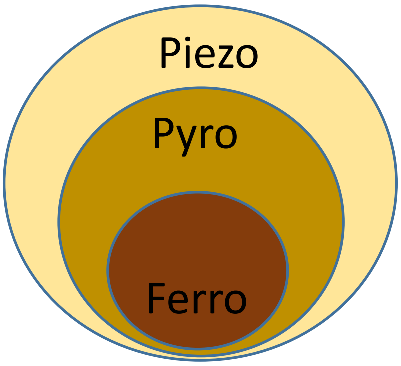

Figure 2. 14 The relationship between piezo-, pyro, and Ferroelectric materials [51]

Like any other materials, pyroelectric materials also have pros and cons. Pyroelectric materials are known for their long durability, wide dynamic range, and good sensing capabilities. On the other hand, one can observe an output charge decay towards zero the constant load. Figure 2.15 describes the behavior of a pyroelectric material when there is a change in temperature [52].In the material, electric dipoles are around their equilibrium axis.

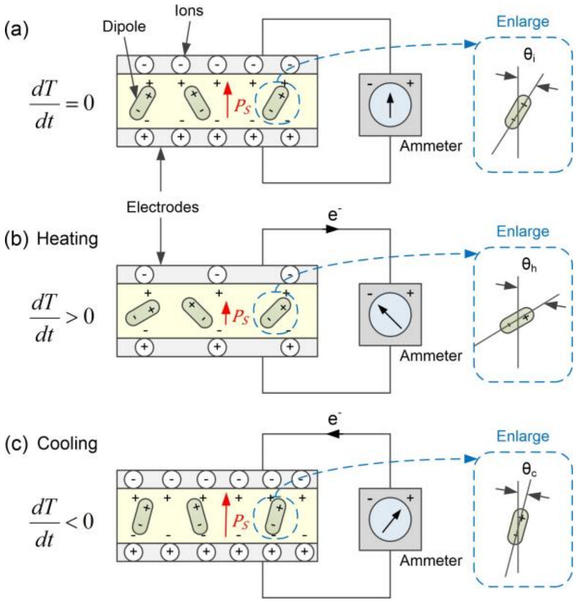

Figure 2. 15 Schematic of a pyroelectric material according to [52]

In Figure 2.15 (a), without a temperature variation, the polarisation remains stationary due to which no current flows. In Figure 2.15 (b), when the temperature starts increasing ($dT/dt > 0$), it leads to an increase in thermal energy dipoles oscillating at an angle (θ_h) which is more significant than the original angle (θ_i). Because of this, there is a decrease in the total level of spontaneous polarisation. On the contrary, in Figure 2.15 (c), when the material is cooled ($dT/dt < 0$), the dipoles oscillate with a small angle (θ_c) as there is low thermal energy. This ($\theta_i > \theta_c$) starts increasing the level of spontaneous polarisation. We can conclude that the pyroelectric material generates an alternating current when there is a temperature change.

This research aims to study and develop the hybrid energy harvesting system based on the pyroelectric and piezoelectric effect and materials. Both piezoelectric and pyroelectric effect and material will be discussed in the next chapter.

2.3.4 Thermodynamic cycles for pyroelectric conversions

Pyroelectric conversion is based on the thermodynamic cycles. The pyroelectric transformation needs an electric form of thermodynamics as the material's electric polarisation depends on the temperature change [53] .

2.3.4.1 Olsen cycles

The Olsen cycle is one of the most common thermodynamic processes used to describe the pyroelectric conversion. This thermodynamic cycle is modified so that it shows the behavior of hysteresis due to polarisation. Here we can also calculate, the net electrical energy of the process which is as follows [54] :

Electrical energy = the total energy - the hysteresis loss

This is represented in Figure 2.16. With the colored area under the curve in the figure, we can observe the mechanism of the Olsen cycle. It consists of two isoelectric fields and two isothermal processes in the electric displacement (D) versus electric field (E) diagram [55]. This figure also discusses the achieved cycle of energy harvesting when a pyroelectric material is operated between T_{cold} and T_{hot}.

- Process 1 → 2: Isothermal charging from E_L to E_H at a low-temperature T_{cold}.
- Process 2 → 3: Isoelectric heating from T_{cold} to T_{hot} at a constant electric field E_H.
- Process 3 → 4: Isothermal discharging from E_H to E_L at a high-temperature T_{hot}.

- Process 4 → 1: Isoelectric cooling from T_{hot} to T_{cold} at a constant electric field $_{\mathrm{EL}}$.

The area enclosed by the cycle 1-2-3-4, i.e. the colored area, in the D-E diagram of Figure 2.16 represents the net harvested output electrical energy density per cycle N_D and defined as [53]:

$$N_D = \oint EdD \tag{2.6}$$

Ashcon Navid et al. presented three different types of 60/40 (polyvinylidene fluoride trifluoroethylene) [P(VDF-TrFE)] copolymer samples, namely commercial, purified, and porous films, which were able to get a maximum energy density of 521 J l−1 and 426 J l−1 per cycle, with a purified film that was about 50 μm thick.

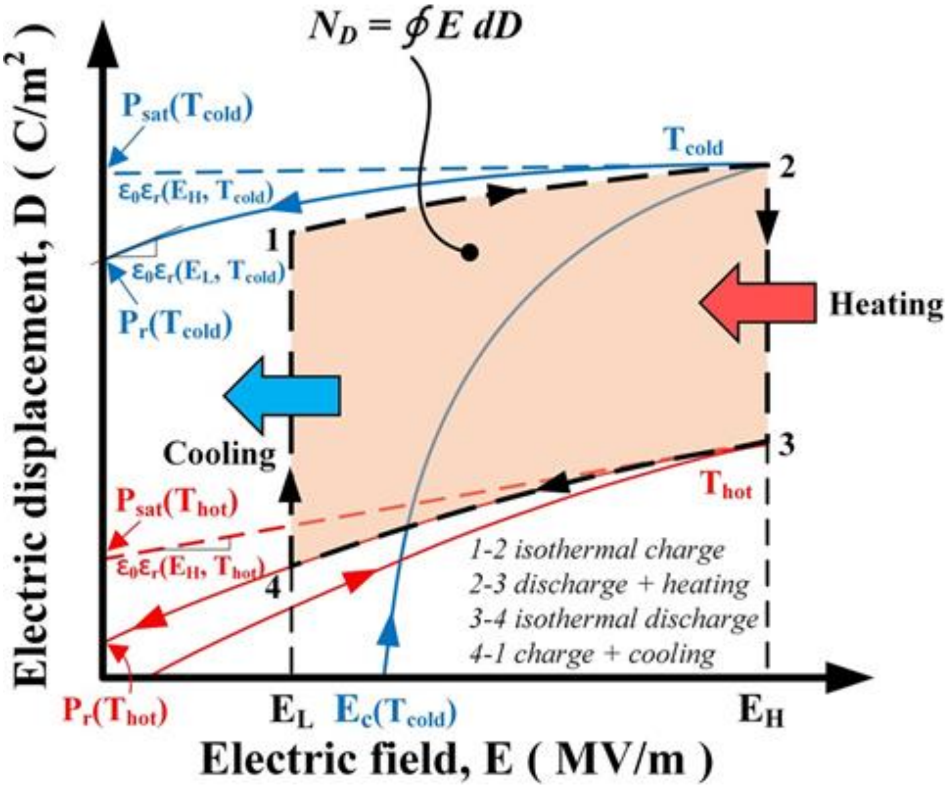

Figure 2. 16 Olsen cycle: D-E hysteresis loop at temperatures T_{hot} and T_{cold} from [53.]

2.3.4.2 Ericsson cycles

The Ericsson cycle consists of two isothermal and two isobaric processes, as shown in Figure 2.17.

However, the Ericsson cycle for a pyroelectric generator consists of two isothermal processes and two constant electric field processes in the electric displacement (D) versus electric field (E). The electric displacement is defined as $D = \varepsilon_0 E + P$ where ε_0 is the vacuum permittivity, and P is the electric polarization.

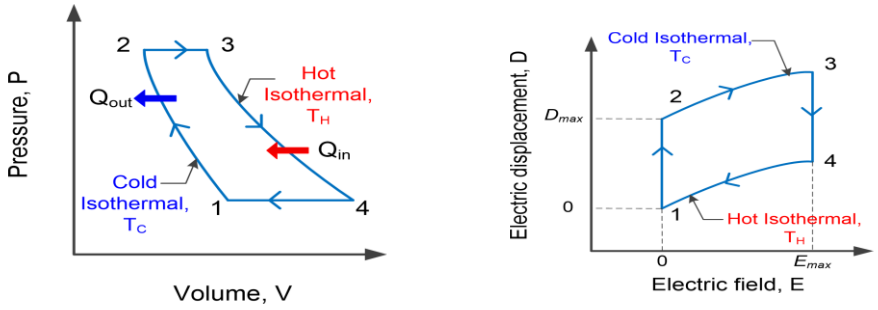

(a) Ideal Ericsson cycle

(b)Ericsson cycle for pyroelectric conversion

Figure 2. 17 Ericsson cycles.

The Ericsson cycle for pyroelectric conversion is as follows

- Process 1 → 2: Constant electric field heat removal.
- Process 2 → 3: Isothermal increasing the electric field from zero to E_{max}.
- Process 3 → 4: Constant electric field heat addition.
- Process 4 → 1: Isothermal decreasing the electric field from E_{max} to zero field.

The following equation can calculate the net electric work [49] .

$$W_{out} = -(T_H - T_C) \int_0^{E_{max}} p \, dE \tag{2.7}$$

Where T_H is a hot reservoir, T_C is a cold reservoir, E_{max} is an electric field, and p is the pyroelectric coefficient. The heat source's net heat energy transferred to the pyroelectric generator is given by Equation (2.8)

$$Q_{in} = c(T_H - T_C) + \int_0^{E_{max}} p T_H d_E \tag{2.8}$$

The Ericsson efficiency of the pyroelectric generator, η_E, can be calculated by equation. (2.9) where c is the heat capacity.

$$\eta_E = \frac{|\, W_{out} \,|}{Q_{in}} = \frac{\int_0^{Emax} pdE}{c + \frac{T_H}{(T_H - T_C)\int_0^{Emax} pT_H dE}} \tag{2.9}$$

2.4 Vibrational Energy Harvesting

Along with thermal energy harvesting, vibration energy harvesting was also studied extensively in this research. Mechanical vibrations will be the second source of energy studied for the hybrid energy harvesting concept for this research.

Vibration and Electrostatic energy harvesting are the approach's where energy from exploitative vibrations can be converted into electrical energy by using piezoelectric or electromagnetic transducers. This study aims at a low-frequency range (1-500) Hz, as this range of frequency is readily available in automobiles for harnessing. This section begins with the necessary information of vibration sources. After that, a full description of the electrostatic, electromagnetic, and piezoelectric energy harvesting effect is presented.

2.4.1 Vibration Source

Vibration is the most prevalent energy source as it is available in abundance in our surroundings, including buildings, roads, bridges, vehicles, ships, moreover, human activities like human walking and riding bicycles are also a source of vibration energy[56].

2.4.2 Electrostatic energy harvesting

Electrostatic energy harvesting devices uses a variable capacitor structure to generate charges from a relative motion between two plates and an energy transfer circuit. The electrostatic effect takes place between the parallel plates of the capacitor on which the charges are stored. The process of harvesting the electrical energy is attained by keeping one plate fix and moving the other by an external mechanical motion to one of the variable capacitor parameters: either plate or the plate separation. This will allow the mechanical movement to be converted into the electrical energy. The electrical energy can be stored and utilized by a load [57], as shown in Fig.2.18.

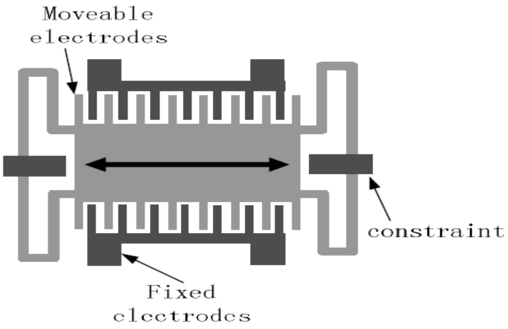

Figure 2. 18 Representation of a typical electrostatic harvester vibrating horizontally. [59].

The basic concept behind moving electrode electrostatic transduction is the available gap or overlap between two parallel capacitor plates. The main advantage of these designs is that they are very suitable for integration in MEMS devices, and due to well-known processing steps, miniaturization is very easy. But there are some disadvantages present for this kind of device, such as the need of high priming voltage to achieve the necessary transducer forces while having a gap size between the plates that can still be fabricated. Some researchers like Mitcheson et al. presented a device in [58] working on this principle. Nevertheless, some researchers like Suzuki and Tsutsumino et al.[59], [60]and Boisseau [61] found out that by using electret materials, we can eliminate the need of priming voltages in electrostatic energy harvesting.

2.4.3 Electromagnetic energy harvesting

Electromagnetic energy harvesting devices are based on using a permanent magnet and a coil to convert mechanical energy into electrical energy. The electromagnetic energy harvesting is based on Faraday's law of electromagnetic induction. Faraday discovered that if an electric conductor is moving through a magnetic field, a potential difference will be induced between the ends of the conductor. The Principle of the faradays law is that a voltage or electromotive force induced in a circuit will be proportional to the time rate of change of the magnetic flux linkage of that circuit. One of the main disadvantages of this kind of devices is that the cost of these energy harvester can be high when compared with the overall cost of a wireless sensor. Nevertheless, the advantages of these devices are that

their principle works perfectly fine for larger-scale applications. They are commercially available [62], they can provide high output currents and they have a long lifetime.
In the past, many researchers explore energy harvesting based on electromagnetics. For instance Saha et al. [63] gave an introduction to electromagnetic energy harvesting, while P. D. Mitcheson et al. [64] showed the basic principle of the electromagnetic system. Overall, the operating principle is based on Faraday's Law. Further, an exciting concept with a levitating magnet is given by Wang et al.[65] . Beeby et al. [66] worked on a micro electromagnetic generator the generator was able to delivers 30% of the power supplied from the environment to useful electrical power.

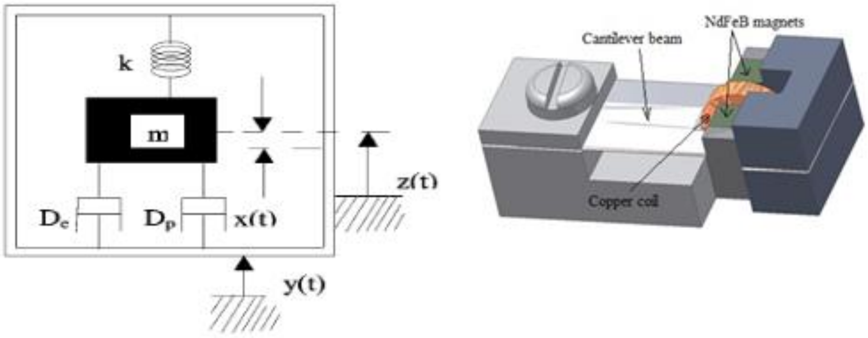

Figure 2. 19 (a) Schematic diagram of the electromagnetic generator. m - Mass, k- spring D – damping [63], (b) representation of a micro electromagnetic transducer [65].

2.4.4 Piezoelectric energy harvesting

The piezoelectric effect is a phenomenon that can be seen in certain solid materials, can generate an electric charge in response to applied mechanical stress. Conversely, an applied electric field produces a mechanical strain, as shown in Fig.2.20. Jacques and Pierre Curie were the first who discovered the piezoelectric effect in 1880 [67].

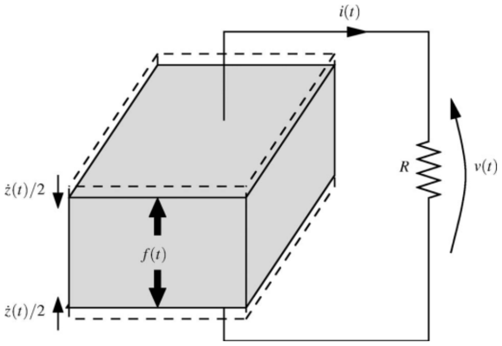

Figure 2. 20 the principle of operation of the piezoelectric transducer [68].

The IEEE Standard on Piezoelectricity provides a theoretical background [68]. The concept of piezoelectric energy harvesting became very popular over the years. Mohsen Safaei et al. [69] presented a lengthy description of piezoelectric transducers. In piezoelectric energy harvesting, the most used designs are the unimorph and bimorph structures. Often, an inertial mass is added to the tip of beam harvesters to decrease or tune the resonant frequency of the system as well as to improve the mechanical response and output power in low amplitude excitations [70] (Figure 2.21(a)). Various configurations having different shapes and sizes have been implemented in piezoelectric energy harvesting. Based on the application the piezoelectric devices configuration like in various application we need a miniature for that the device must be smaller in size simultaneously in some applications they must be working in a particular range of frequency in order to harvest the maximum energy. There are many shapes and sizes have been implemented in piezoelectric energy harvesting so far. Here a detailed review is depicted in Figure 2.21 starting with the most standard design that have been implemented was a beams shape cantilever. Other structures like non-rectangular profiles, such as triangle-shaped beams [71] are also represented in (Figure 2.21(b)) which had been widely used, by incorporating these profiles, the output energy along with the maximum tolerable excitation of the cantilever harvesters can be improved. Other methods like changing the mechanical boundary conditions and different beam configurations, including designs with dynamic amplifier support instead of a fixed end also depicted in (Figure 2.21(c)), as well as an asymmetric tuned mass can also play a significate role in improving the out power of the harvester [72] (Figure 2.21(d)), simultaneously by implementing an auxiliary beam can tune the frequency of the harvester [73] (Figure 2.21(e)). Lee et al. in 2007 [74] presented a slider mechanism with multiple super elastic shape memory alloy ridges with low-frequency movement, which is used to excites a piezoelectric bimorph at the natural frequency [75] (Figure 2.21(f)). Jung et al. in 2010 [76] proposed a novel concept which consisted of four buckled slender bridges with a proof mass and multiple piezoelectric cantilever beams working based on a snap-through mechanism (Figure 2.21(g)). Halim and Park in 2014 [77] include a compliant driving beam which periodically impacts one or two piezoelectric beams to excite the generator beams at their resonant frequency (Figure 2.21(h)). Using a pair of spiral piezoelectric beams, two permanent magnets, and a resonator mass, Galchev et al. in 2012 [78] developed another impact-driven energy harvester package which can produce noticeable power from low-frequency vibration (Figure 2.21(i)).

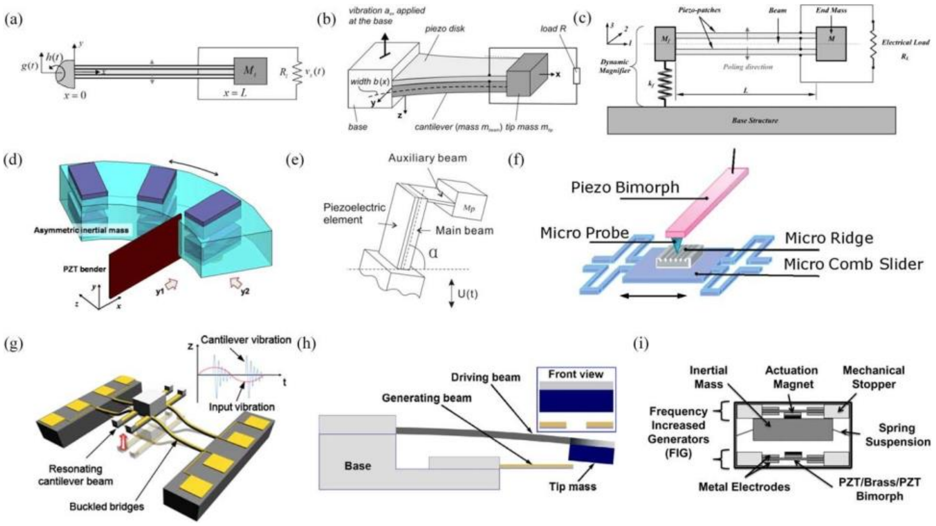

Figure 2. 21 Various piezoelectric beam harvesters with (a) tip mass [70],(b) non-rectangular profile [71], (c) dynamic amplifier support [72], (d) asymmetric tip mass [73],(e) added auxiliary beam [74], (f) slider mechanism [75]), (g) snap-through mechanism [76], (h) compliant driving beam [77], and (i) impact driven mechanism [78]).

Figure 2.22 shows the perovskite crystal structure of PZT. This material exhibits an electric dipole below the Curie temperature due to the distortion of the ideal perovskite structure. After the PZT ceramic sintering process, these dipoles are all in random orientation, and the material does not have any piezoelectric behavior yet. They are aligned by applying a large electric field during the polarisation process and heating the material just below the Curie temperature. This alignment persists after cooling down. The linear constitutive Equations (2.10) describe the linear constitutive model of an unbounded piezoelectric continuum, the parameters being assumed to be constant regardless of mechanical or electrical load follows [79]:

$$\begin{aligned} S_{ij} &= s_{ijkl}^{E} T_{kl} + d_{kij} E_k \\ D_i &= d_{ikl} T_{kl} + \varepsilon_{ik}^{T} E_k \end{aligned} \tag{2.10}$$

Where T_{kl} are the stress components, S_{ij} the strain components, E_k, the electric field component, D_i is the electric displacement component, d_{kij} and d_{ikl}, piezoelectric constants, and ε_{ik}^{T} permittivity constants, and s_{ijkl}^{E}, elastic compliance constants. These two equations show the interaction between the electrical and the mechanical properties of piezoelectric materials. The perovskite structure of PZT is shown in Figure 2.22 [80].

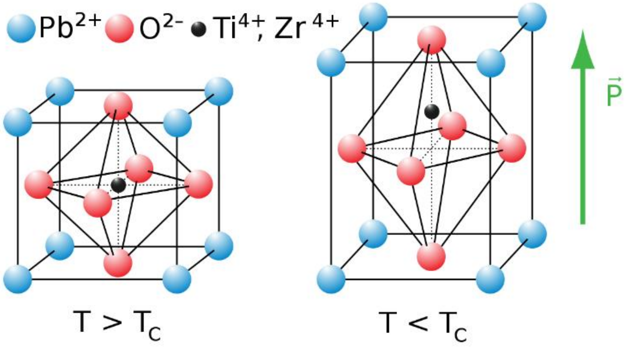

Figure 2. 22 Perovskite structure of PZT [80].

2.5 Hybrid thermal-vibrational Energy Harvesting

This research aims to develop a hybrid thermal-vibrational energy harvester based on piezoelectric and pyroelectric effects. The Proposed approach which will be presented in the next chapters consists in using both piezo- and pyroelectric effects from the same materials. Hence the literature survey here is mainly focused on hybrid thermal-vibrational energy harvesting. The review begins with an overview of the generic thermal-vibrational energy harvesting, starting first by generic existing approaches, and then continuing with basic mechanisms of hybrid piezo-pyro harvesters. Finally, a brief description is provided of the materials that can be used for hybrid thermal-vibrational energy harvesting.

2.5.1 Survey on thermal-vibrational energy harvesting

The existing hybrid harvester were mainly based on the PVDF, PZT, and PMN-PT piezoelectric materials, which are ferroelectric. Among them Lee et al. [81], Chen et al. [82], and You et al. [83] presented harvesters utilizing both piezo- and pyroelectric effects. In Lee et al. team's research, the harvester was based on poly (vinylidene fluoride-co-trifluoro ethylene) [P (VDF-TrFE)] polymer for the pyroelectric material. In this, the bottom electrode was based on

Polydimethylsiloxane (PDMS)-carbon nanotubes (CNTs) composite while the top electrode based on graphene with high thermal conductivity was used. Chen et al. presented a flexible generator using single-crystal $(1- x) P b (Mg, Nb) O3 - xP bT iO3$ (PMN-PT) for the pyroelectric material, which has high piezo- and pyroelectric coefficients. Finally, You et al. used PVDF for the pyroelectric material where the bottom electrode was made up of thermoplastic polyurethane (TPU) nanofiber membranes-carbon nanotubes (CNTs) composite. The upper electrode, electrospun poly (3, 4- ethylene dioxythiophene): poly (styrene sulfonate)-polyvinyl pyrrolidone (PEDOT: PSS-PVP) conductive nanofiber membranes. The main advantage of using a hybrid energy harvesting device is that they can harvest more energy than the individual harvesting element.

2.5.2 Hybrid thermal-vibrational energy harvesting

The literature survey shows that there were not many studies focusing on mechanism or design of hybrid thermal-vibrational energy harvesting .Gusarov et al. proposed polyvinylidene fluoride (PVDF) with shape memory alloys (SMA) [84]. In this research, the authors used a composite that was laminated with SMA on both sides of the PVDF polymer. With the change of temperature, strain due to SMA's deformation is induced by the phase transition and imposes deformation to the piezoelectric material. As a result, from the direct piezoelectric effect, the output voltage was improved by 77% than from the structure without SMA. On the other hand, Kim et al. presented a wearable hybrid generator based on the pyroelectric effects and thermoelectric using heat from human skin [85].

2.5.3 Materials used for hybrid piezo-pyro energy harvesting

Various properties modifications have been made to improve the material's energy harvesting performance. These modifications include doping technique, or also porosity alignment of PZT ceramics [86]. These kinds of aligned pore channels significantly increased the generated energy as they reduced the material's volume-specific heat capacity and permittivity. It can be found that the pyroelectric coefficient of PZT is about 320 μC m−2 K^{-1} under an optimal condition. Other researchers like Kim et al. presented a P (VDF-TrFE)-based generator [87]. It can be noticed that the output performance was significantly improved in a high dipole moment solvent by enhancing the crystallinity and dipole alignment of the polymer. The pyroelectric coefficient of a material out in the solvent reached about 50 μC m−2 K^{-1}. This lead to an increase in the pyroelectric voltage was improved by 40%. Tang et al. carried research with $Bi_4Ti_3O_{12}$ (BiT) ceramics and enhanced its properties by doping with tungsten or manganese [88]. The use of the dopants decreased the electric conductivity of ceramics at the same time. The dielectric loss was also reduced. This modification enhanced both the piezo- and pyro-electric coefficients.

2.6 Towards lead-free hybrid piezo-pyro energy harvester

Lead based piezoelectric materials for energy harvesting devices cause severe pollution to the environment and are toxic. On the other hand, polymer-based hybrid harvesters are attractive because of their simple fabrication process, cost-effectiveness, and mechanical robustness. Still, at the same time, the realization of these polymer-based harvesters is challenging as they generate low output power.

In this thesis research we aim to develop a hybrid energy harvester based on lead-free materials as they will make our environment green and clean and, at the same time, will reduce our dependency on lead-based materials like lithium-ion batteries. To this aim, we will use Lithium niobate and PVDF to have both the piezoelectric and pyroelectric properties for this research. Lithium niobate is compatible with high-temperature applications (up to 1000 °C) .We will also use SMA (shape memory alloy) as they allow a relatively large strain (about 8%) when deformed [89]. In a way, it will increase the piezo effect. Finally, in this study, we aim to make prototypes capable of working at high temperatures and low-frequency range (1-500) Hz.

As mentioned in the previous section the literature on lead-free hybrid energy harvesters is very few. Sun et al. [90] presented tribo-, pyro-, and piezoelectric hybrid harvesters based on lead-free materials like PDMS, PVDF, and silver nanowires. The PVDF layer was for pyro- and piezoelectric, and PDMS is for the triboelectric effect. Ji et al. [91] presented a nanogenerator using barium titanate ($BaTiO_3$). $BaTiO_3$ is a ferroelectric material and exhibits the photovoltaic effect. Therefore, this device used for pyro-, piezo-, tribo- and photo-electric effects. Ding et al. [92] presented a hybrid thermogalvanic and pyroelectric generator by generating pyroelectricity from photothermal effect. In the study, the authors used PVDF and a block of polyurethane sponge. The sponge was soaked with ferric/ferrous chloride solution to obtain the temperature gradient as it will act as a thermogalvanic electrolyte for the thermogalvanic effect. The PVDF film was coated with carbon nanotubes and cellulose (CNC) nanocrystals nanocomposite as electrodes.

2.7 Conclusion

This chapter briefly introduces generic information regarding energy harvesting system as well as various energy sources available for that. The harvester's installation environment determines the energy source, and for the best results, the appropriate mechanism or principle of harvesting must be selected accordingly. Among the various energy sources, the review focuses mainly on thermal and vibrational energies, which are the main objective of this study. To this aim, this study will exploit both pyro and piezoelectric effects using lead-free ferroelectric materials as we know that lead based materials are not good for environment considering this factor we focused on lead-free materials.

The basic mechanism of hybrid energy harvesting is presented. Firstly, a study is done for exploiting the individual piezoelectric and pyroelectric effect and then a coupled piezoelectric and pyroelectric effect study is conducted. Simultaneously finite element analysis is also presented for the individual piezoelectric and pyroelectric effect and coupled piezoelectric and pyroelectric effect.

A concept of closed system is also introduced to exploit both the piezo-pyroelectric effect at a constant temperature, and its performance has been investigated using COMSOL Multiphysics® finite element method (FEM) software for rapid validation of the proof of concept and for visualization of the transducer functioning. The proposed hybrid harvester can convert both vibrational mechanical energy and constant temperature energy into electrical energy. The principle behind the constant temperature conversion is based on the Joule-Thomson physical principle.

Finally, the possibility of an energy harvester application is presented in various environments for wireless sensor networks, which mainly aim at powering sensors present in automobiles with different energy sources working at different frequencies.

3. Design and fabrication of structures for thermal and vibrational energy harvesting

3.1 Introduction

This Chapter presents the harvester's initial design and mechanism used for harvesting vibrational and thermal energy. The experimental implementation for each effect 1. vibrational (piezo effect) 2. thermal (pyro effect) is individually presented. The initial setup is based on the cantilever beam structure. Then, a new design in the form of a circular ring that embeds the cantilevers to create nonlinear behavior when excited with ambient vibration is also presented. The finite element simulation for both the harvester designs is demonstrated as well.

In an automobile, which is the application targeted by the project, the temperature keeps changing (from a few degrees °C to over (100°C-200°C) [93]*) due to heat generated by the engine during its starting or switching off, which is therefore, an ideal environment for the pyroelectric materials for thermal energy harvesting.*

For the fabrication process, we have used three different materials, a single crystal piezoelectric material (Lithium Niobate), a piezoelectric polymer (PVDF), and a Shape Memory Alloy (Nitinol). The purpose of using these materials will be discussed in detail in the coming sections.

3.2 A lead-free piezoelectric E.H. with a cantilever structure

The proposed mechanism consists of single-crystal (Lithium Niobate 128°Y), a Piezoelectric polymer (PVDF), and a Shape memory alloy (Nitinol). Several types of lead-free piezoelectric materials are available, like KNN films, which have one of the highest power density values (1.6 $mW.cm^{-3}$) among the micro-PiViEHs [94]. However working with some materials like KNN is difficult as the alkaline oxide composition is challenging to control [95] and not readily available. On the other hand, Lithium Niobate ($LiNbO_3$) crystal is an entirely known piezoelectric material that is toxic-free and readily accessible in the form of wafers. For instance Lithium Niobate is widely used in fields like acoustics and optical devices [96]. There are several advantages of using $LiNbO_3$ over lead-based materials like PZT, as LiNbo3 is a chemically inert material. It can withstand high temperatures due to very high Curie temperature. Researchers' first choice when it comes to lead-free piezoelectric energy harvesting is based on high temperature working conditions. Regarding PVDF in energy harvesting, it has high flexibility compared to a ceramic-like PZT to withstand large deformation. PVDF is a lead-free material, which makes it suitable for this research. It can be coated on substrates or parts by several coating methods, making it compatible with micro-electro-mechanical systems (MEMS) technology.

Using a shape memory alloy (SMA) element, the mechanical stiffness of the cantilever structure under vibration can be tune in order to fit the resonant frequency to increase the output power [97]. Nevertheless, due to the sizeable mechanical deformation of shape memory alloys (SMA) in the vicinity of their thermally induced phase transition, it can convert this mechanical energy into electrical energy with relatively good efficiency by coupling SMA with piezoelectric materials [98] .

3.2.1 Initial Design and operating principle

To build cost-effective piezoelectric energy harvesters, prior modelling is needed. For this purpose, different software packages like ANSYS or COMSOL Multiphysics can be used. Usually, the initial design gives an idea of how the developed PEH configuration will perform. Thus, one of this research's objectives was to create a general and universal finite element (F.E) model of PEH, which could be easily changed based on our requirements. A cantilever configuration is one of the most promising piezoelectric structure to acquire high output power [99]. This can be noticed due to a large amount of strain applied to the vibration condition elements. Due to this reason and for simplicity, we started our initial design as a cantilever beam. There are three types of cantilever beam structures classically used as piezoelectric generator: unimorph, bimorph series, and bimorph parallel. The working principle based on the d31 (transversal mode) and d33 (longitudinal mode) is the most exploited coupling mode in energy harvesting with cantilever configuration. In mode-31 the force is applied in a perpendicular direction towards the poling direction, while in mode-33 the force is applied in the same direction as the poling direction [100] shown in Figure 3.1.

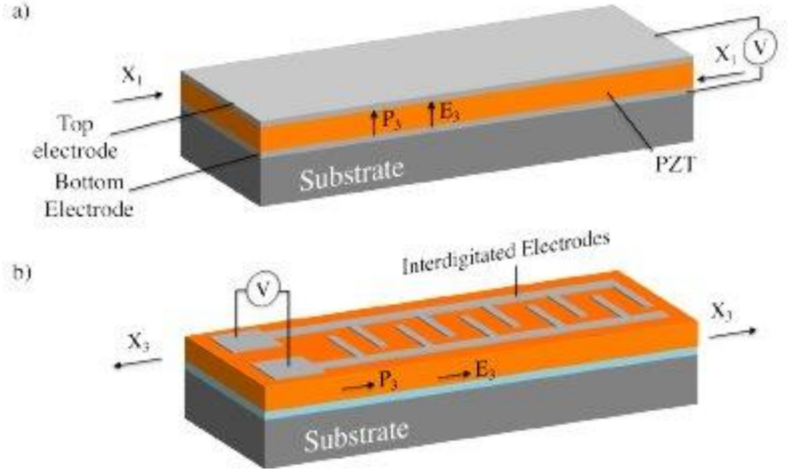

Figure 3. 1(a) d31 mode piezoelectric material operation, (b) d33 mode piezoelectric material operation [100].

A piezoelectric cantilever can be defined as a structure with one end fixed and another end free to vibrate. It can be composed of one or more layers of piezoelectric material bonded to an elastic metal called a substrate. Primary purpose of using this substrate is to increases the structure's sensitivity helps in reducing the brittleness of the piezoelectric layer [101]. Let us focus on the behavior of the piezoelectric layer when a mechanical stress is applied. The IEEE/ANSI standard on piezoelectricity [67] has given different form of piezoelectric constitutive Equations to express the resulting electricity. Equation (2.8) is one of them which is described in the previous section. Mathematical equations are provided for calculating the Piezoelectric Charge Constant and Piezoelectric voltage constant.

In Equation (2.8) which expresses the direct piezoelectric effect:

$$D = d \times T \tag{2.8}$$

The piezoelectric charge constant d is the amount of electric displacement D that is induced in the material for the applied mechanical stress T under zero electric field.

Two subscripts are used in the piezoelectric charge constant. The first subscript is used to represent the direction of the electric displacement or polarization. The second one is used to denote the order of the applied mechanical stress. The numbers 1, 2 and 3 in the subscripts represent the x, y, and z-axis. In most cases, the usual z-axis is the poling axis. For instance, d_{31} represents that the electric displacement is induced along axis 3 when stress is applied along axis 1.

Another form in the IEEE/ANSI standard on piezoelectricity is the piezoelectric voltage constant which is as follows:

$$E = -g \times T \tag{3.1}$$

Here the piezoelectric voltage constant g is the amount of electric field E generated per unit of mechanical stress applied T. As discussed above, similarly, like the charge constant d, the voltage constant is also represented with subscripts. For instance, g_{31} denotes the electric field is induced along axis 3 when stress is applied along axis 1.

The piezoelectric charge constant and the voltage constant are related to each other as represented in Equation (3.2):

$$g = \frac{d}{\in} = \frac{d}{\in_r \in_0} \tag{3.2}$$

Where, $\in_0$ is the permittivity of free space and $\in_r$ is the relative permittivity. Both these constants are temperature dependent. The piezoelectric charge constant increases with an increase in temperature, while the piezoelectric voltage steadily decreases with the temperature rise.

Coupling coefficient

One of the most critical parameters in piezoelectric energy harvesting is the coupling coefficient. It shows how much the mechanical/electrical energy is converted into electrical/mechanical energy.

$$k^2 = \frac{\text{Mechanical Energy Converted into Electrical Energy}}{\text{Input Mechanical Energy}} \tag{3.3}$$

Equation (3.3) represents the coupling coefficient for the direct piezoelectric effect. The product of the piezoelectric charge constant (d) and the piezoelectric voltage constant (g) plays a critical role in energy harvesting application. It is used to calculate the energy density of a piezoelectric material. Energy density is the measure of the amount of energy stored in the material per unit volume. A material with a higher (d·g) product will generate higher power, and the material has a higher energy density [102].

$$U_e = \frac{1}{2}(d.g)\left(\frac{F}{A}\right)^2 \tag{3.4}$$

Where F is the applied force, A is the area, and U_e is the energy density.

The resonant frequency is the most crucial parameter of a vibration energy harvesting device. It is calculated by using the given Equation (3.5).

$$f_n = \frac{v_n^2}{2\pi}\frac{1}{L^2}\sqrt{\frac{D_p}{m}} \tag{3.5}$$

Where $V_n = 1.875$ for the first mode, m is the mass per unit area, and D_p is the bending modulus, which is a function of Young's modulus and thickness of the substrate and expressed by Equation (3.6), here Equation (3.6) is for a two layers cantilever: one passive layer and one piezo layer:

$$D_p = \frac{E_p^2 t_p^2 + E_S^2 t_S^2 + 2E_S E_p t_p t_S \left(2t_p^2 + 2t_S^2 + 3t_S t_p\right)}{12\left(E_S t_S + E_p t_p\right)} \tag{3.6}$$

Hence the variation of resonant frequency can be written as Equation (3.7).

$$f_n \propto \frac{1}{L^2}\sqrt{t_p}\sqrt{t_s} \tag{3.7}$$

Where L is the length of the harvester, t_p is the thickness of the piezoelectric layer, and ts is the substrate layer's thickness, here the p and s subscripts define the piezo layer and passive layer. The electrical output voltage is highest when stress is maximum, which is occurs at the resonance frequency [103].

3.2.1.1 Initial Design and operating principle for VEH

As described above, the cantilever structure is the simplest but most used design. We suggest therefore to exploit this structure for our first design of hybrid energy harvester. Here the design consists of Lithium Niobate (128°Y), a metallic beam made up of Shape memory alloy (Nitinol), and a polymer thin film. The schematic of the harvester is shown in Figure 3.2. Again, one end of the cantilever beam was fixed, and the other end was free to vibrate.

For a better understanding of the mechanisms, the modelling is provided. For simplification, the modelling is done, keeping in mind a thick layer of piezoelectric material is bonded on a substrate. This thick layer will not change the cantilever's shape, but it will increase the whole system's bending stiffness.

As discussed above, piezoelectric energy harvesters typically work in two modes, either 33 mode or 31 mode in which the first digit is used to denote the direction of the generated polarization, and the second digit is used to represent the direction of stress or strain.

The IEEE/ANSI [67] shows the linear constitutive equations of a piezoelectric material, which can be written in a tensor form as below:

$$S_i = S_{ij}^{\in}\sigma_j + d_{mi}\epsilon_m \tag{3.8}$$

$$D_m = d_{mi}\sigma_i + \varepsilon_{ik}^{\sigma} \in_k \tag{3.9}$$

Here S_j is the strain $S_{ij}^{\in}$ are the elastic compliance constants, σ_j are the stress components, $\in_m$ and $\in_k$ are the electric field components, D_m is the electric displacement component, which shows the effects of electric charges, d_{mi} are the piezoelectric strain coefficients, and $\varepsilon_{ik}^{\sigma}$ are the dielectric constants. Here, since piezoelectric material operates in 33 mode, Equation (3.8) and (3.9) can be simplified as:

$$S_3 = \frac{\sigma_3}{E} + d_{33}\epsilon_3, \tag{3.10}$$

$$D_3 = d_{33}\sigma_3 + \varepsilon \in_3 , \tag{3.11}$$

Where E represents Young's modulus of the material, and ε is the dielectric constant. Similarly, when a piezoelectric material is operating in 31 mode, the linear constitutive equations become

$$S_1 = \frac{\sigma_1}{Y} + d_{31}\epsilon_3, \tag{3.12}$$

$$D_3 = d_{31}\sigma_1 + \varepsilon \in_3 , \tag{3.13}$$

For a piezoelectric material subjected to uniform stress σ, the open-circuit voltage which is generated can be derived from Equation (3.11) and (3.13) by assuming zero electric charges on the material, as below Equation (3.14),

$$V_{open} = -\frac{d\sigma}{\varepsilon} t_p \tag{3.14}$$

Here t_p is the thickness of the piezoelectric material, and d represents the piezoelectric coefficient in 33 or 31 modes. When a unimorph cantilever bends, it results in the stress distributions to which the above and below the neutral plane will generate opposite signs. Assuming the neutral axis to be centered in the cross-section of the structural element, the polarization above the neutral line due to tension is expected to substantively cancel the polarization below the neutral axis due to compressive strains. Nevertheless, to avoid charge cancellation problems, piezoelectric transducers can be developed using two piezoelectric unimorphs to form a piezoelectric bimorph beam. In this kind of structure, each layer operates in 31 mode, where two separate unimorphs are bonded directly to each other or with a metal shim in between. The bimorph is fixed at one end, and the other end is usually free to vibrate and forms a cantilever beam. As the cantilever bends down, the top layer exhibits expansion, and the bottom layer exhibits compression, and both generate voltage as output. These responses are obtained from the two layers and then combined carefully to get the output voltage.

There can be two ways to work with the piezoelectric unimorph. If the poling direction is vertical, then the electrodes on the top and bottom surfaces results in a vertical alignment of the domains and the cantilever works in d31 mode. However, a back-and-forth in-plane poling direction can be attained with the interdigitated electrodes. Bimorph beam is typically made up of two unimorph layers with vertical poling directions stacked together. Usually, this type of bimorph has electrodes on the top and bottom surfaces. Figure 3.2 shows the two kinds of piezoelectric bimorph series and parallel type bimorph. In series type, the top and bottom layers have opposite directions of polarization.

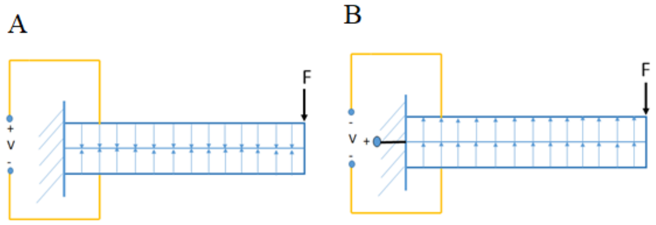

Figure 3. 2 Schematic diagram of piezoelectric series type bimorph operation using a series connection (a) and parallel type bimorph function using the parallel connection (b).

In series type bimorph requires that the piezoelectric layers are oppositely poled, such that when acceleration is applied, charge of one polarity exists on one of the outer electrodes while charge of the opposite polarity exists on the other outer electrode. However, parallel connection requires that the piezoelectric layers are poled in the same direction so that, when subjected to acceleration from a vibration source, charge of the same polarity appears on the outer electrodes of the device. Thus, the outside electrodes are connected to make one electrical output terminal, and the centre layer constitutes the other electrical output terminal, as shown in Figure 3.2. The Series type bimorph can produce almost twice the voltage as the parallel type bimorph under the same displacement amount. A series type bimorph cantilever, as in Figure 3.2 (a), can be modelled as a uniform beam based on the Euler-Bernoulli beam theory. The stress inside the beam can be expressed as

$$\sigma = -\frac{M_{(x)}y}{I_c} \tag{3.15}$$

Here, $M_{(x)}$ is the bending moment at the location x along the beam length, I_c is the moment of inertia of the beam's cross-section, and y is the distance from the beam's neutral axis to the location of interest along with the beam thickness. Therefore, the average stress of the cantilever beam with a rectangular cross-section can be written as

$$\overline{\sigma_s} = \frac{1}{l}\int_0^1 \frac{M_{(x)}\frac{t}{2}}{I_c}dx \tag{3.16}$$

Where l is the length of the cantilever beam and t is the thickness of the entire bimorph. The moment along the beam length can be derived by using the tip force given in Equation (3.17) as

$$M_{(x)} = F_t x = \frac{ma}{2\zeta_t}x = \frac{kY_0x}{2\zeta_t} \tag{3.17}$$

Where ζ_t is the total damping coefficient, and a is the acceleration of the ambient vibration with an amplitude of Y_o. The mass of the beam m equals $\frac{k}{\omega_n^2}$ in which k is the stiffness of the cantilever and ω_n is the cantilever's structure frequency. By using Equation (3.16) and the value for $k = \frac{3EI}{l^3}$ equation (3.15), the average surface stress can be derived as

$$\overline{\sigma_s} = \frac{3EY_0t}{8\xi_t l^2} \tag{3.18}$$

Where E is the elastic modulus of the cantilever.

3.2.1.2 Initial design and operating principle for Th-EH

For the presented initial design in this research, the concept of pyroelectric effect is described in terms of a coefficient, the pyroelectric coefficient p, given by the rate of change of polarization *Ps* with temperature (T) as shown in Equation (3.19):

$$p = \frac{dP_s}{dT} \tag{3.19}$$

Polarization *P* is the electric dipole moment per unit volume. The other expression for the polarization P can be referred to as the bound surface charge per unit area of a free surface normal to the direction of P. Hence, polarization can be related to the electric displacement D through the linear expression.

$$D_i = P_i + \varepsilon_0 E_i \tag{3.20}$$

The derived constant εo value is 8.854×10-12 C/V·m (permittivity of free space), E_i represents the applied field, D_i is the electric displacement, and P_i is the polarization. In pyroelectric materials, both D and P are nonlinear functions of E, and it may also depend on the material's property. If we neglect the term $\varepsilon_o E_i$ in the above Equation compared to the P, D is nearly equal to P. Henceforth, the D versus E and P versus E plots of the hysteresis loop become equivalent. Simultaneously, the permittivity is referred to as the gradual increase in electric displacement per unit of electric field when the measuring area's magnitude is minimal compared to the coercive electric field. The small-signal relative permittivity, κ, is equal to the absolute permittivity ratio ε to the permittivity of free space ε_o in Equation (3.21).

$$k = \frac{\varepsilon}{\varepsilon_0} \tag{3.21}$$

Even after removing the applied field, the remaining polarization is known as remanent polarization and represented as P_r. Sawyer Tower Circuit can measure the remanent polarization shown in Figure 3.3.

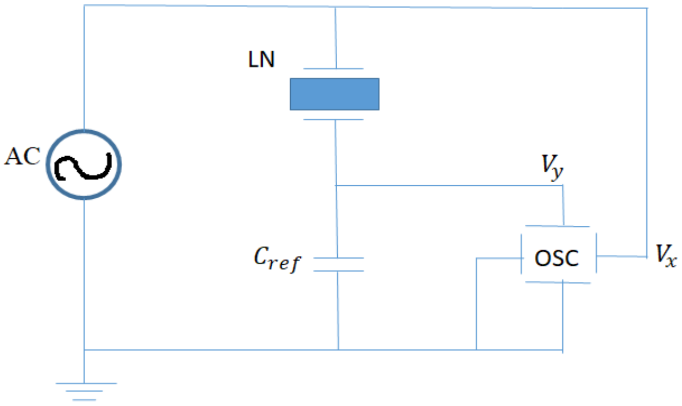

Figure 3. 3 Sawyer-Tower circuit for observing hysteresis loops of pyroelectric materials

3.2.1.2.1 Polarization against electric field hysteresis loop

Polarization-electric field hysteresis is an important property of ferroelectric material. To know Lithium Niobate behavior concerning temperature it was crucial to perform the polarization-electric field hysteresis measurement. Lithium Niobate is a ferroelectric material. A ferroelectric material shows spontaneous electrical polarization, this polarization can be converted by applying an external electric field. The P-E loop shows the developed charge or polarization against the area devoted to that material at a given frequency. The loop can be measured using the Sawyer-Tower circuit, as shown in Figure 3.3. The measurement setup consists of a function generator. In the first step, this function generator is used to supply an alternating electric signal to the circuit, which changes the circuit's charge. Two capacitors are present in the circuit. One is the Lithium Niobate, which will be measured, and the other one is a reference capacitor. The reference capacitor is charged the same as Lithium Niobate in the second step since it is connected in series. Therefore, as the voltage across the Lithium Niobate increases, reference capacitor voltage decreases. Due to this reason, the capacitance of the reference capacitor, C_{ref}, should always be more extensive than that of the piezoelectric material, C_p. The Lithium Niobate layer voltage, Vx, can be larger than the reference's, V_y, by the formula $V_x = Q/C_p$ and $Vy = Q/C_{ref}$. For example, the reference capacitor is 1000 times larger; the reference capacitor's voltage drop is about 0.1% [104]. We can see that by applying voltage, Vy, to the reference capacitor, C_{ref}, the charge can be $Q = C_{ref} \times Vy$. The charge of the Lithium Niobate material can be deduced from the reference capacitor. The polarisation, P, of the Lithium Niobate is given below.

$$P = \frac{Q}{A} \tag{3.22}$$

Where Q is the charge developed on the material, and A is the area of the material. The polarization is proportional to the voltage Vy. As a result, the Lithium Niobate polarisation can be seen by combining two voltages: the applied voltage to the Lithium Niobate on the x-axis and the Lithium Niobate charge y-axis. The electric field, E, of the Lithium Niobate, is given by the applied voltage, Vx.

$$E = \frac{V_x}{d} \tag{3.23}$$

Where d is the thickness of Lithium niobate. The polarization, P, is proportional to the charge Q. Since we know that Q can be represented as Q = CV, Q is proportional to the applied for any voltage (V) and the electric field (E). Due to this, the polarisation and current are 90 degrees out of phase. The P-E loop of an ideal linear capacitor appears as a straight line. In the perfect capacitor, the current leads the voltage by 90 degrees. The P-E loop of an ideal resistor is shown as a circle centred at the origin since the current and voltage are in phase with the resistor. Figure 3.4 shows a diagonal ellipse P-E loop of the Lithium Niobate layer, equivalent to a capacitor and resistor in parallel. This response of the capacitor can be called a lossy reaction [105]. Usually, according to the traditional thermodynamic theory of ferroelectric materials, the remnant polarization and the coercive field decrease with the temperature increase.

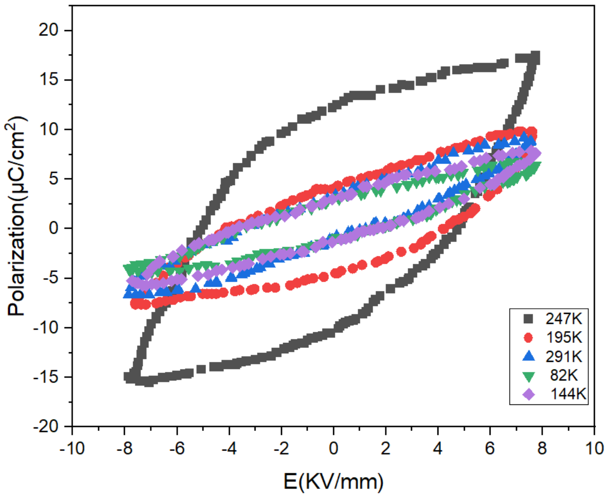

Figure 3. 4 P-E loop for single crystal L.N.

Here in Figure 3.4, we can see the electric current is generated by a temperature change. The P-E loop was measured when the Lithium Niobate material was subjected to a temperature change from 76 K to 247 K. The polarisation shifts can be noticed under the influence of temperature, which is a material property. Generally, the saturation polarization decreases as temperature increases, but some materials have an opposite trend. Even the same material can behave differently depending on the temperature range [106]. When the generator supplied 2600 V, loops with different slopes were achieved, as shown in Figure 3.4. The loop measured at 247K (black) is steeper than that measured at 82K (green). As the temperature increases to 247K, we noticed that the loop's slope becomes steeper in this experiment. However, the obtained slope is proportional to the capacitance, which means that with the temperature rise, the capacitance of this Lithium Niobate increases. With the Olsen cycle's help, we know the estimate of the area enclosed under the curve, and with that, the electrical energy density, N_D., can be calculated by Equation (3.24) [55].

$$N_D = (T_{hot} - T_{cold}) \int_{E_L}^{E_H} PdE \tag{3.24}$$

N_D is net harvested output electrical energy density [mJ/cm^3] per cycle, T_{hot} is the absolute temperature of the hot reservoir, T_{cold} is the absolute temperature of the cold reservoir, E_H is the high electric field, and E_L is the low electric field, P is polarisation and E is the electric field.

3.2.2 Finite element method COMSOL simulation

3.2.2.1 Vibrational simulation

The constitutive equations of a linear piezoelectric material is given by Equation (3.25) which represents the material behavior and used in the FEM software for simulation [107].

$$T = c_E S - eE, \tag{3.25}$$

$$D = e^T S + \varepsilon_S E,$$

where T is the stress vector, D is the electric flux density vector, S is the strain vector, E is the electric field vector, c_E is the elasticity matrix (evaluated at the constant electric field); e^T is the piezoelectric stress matrix; ε_S is the dielectric matrix (estimated at constant mechanical strain). Here equations (3.26) represent the material behavior for which the FEM software solves. The finite element discretization is performed by establishing nodal solution variables and the element shape functions over an element domain which approximates the following solution [108] :

$$\boldsymbol{u_c} = \boldsymbol{N_u^T}\,.\,\boldsymbol{u}, \qquad (3.26)$$
$$\boldsymbol{V_c} = \boldsymbol{N_V^T}.\boldsymbol{V},$$

Where u_c is the displacement within the element domain in the x, y, z directions, V_c is the electrical potential within the element domain, Nu is the matrix of displacement shape functions, N_V is the vector of the electrical potential shape function, u is the vector of nodal displacements, and V is the vector of nodal electrical potential. Using (3.26), the strain S and electric field E are thus related to the displacement and potential by (3.27) and (3.28), respectively. Consider

$$\boldsymbol{S} = \boldsymbol{B_u}.\boldsymbol{u}\,, \qquad (3.27)$$
$$\boldsymbol{E} = -\boldsymbol{B_V}.\boldsymbol{V}, \qquad (3.28)$$

Where,

$$\boldsymbol{Bu} = \begin{bmatrix} \frac{\partial}{\partial x} & 0 & 0 & \frac{\partial}{\partial y} & 0 & \frac{\partial}{\partial z} \\ 0 & \frac{\partial}{\partial y} & 0 & \frac{\partial}{\partial x} & \frac{\partial}{\partial z} & 0 \\ 0 & 0 & \frac{\partial}{\partial z} & 0 & \frac{\partial}{\partial y} & \frac{\partial}{\partial x} \end{bmatrix}^T, \qquad (3.29)$$

$$\boldsymbol{B_y} = \begin{bmatrix} \frac{\partial}{\partial x} & \frac{\partial}{\partial y} & \frac{\partial}{\partial z} \end{bmatrix}^T,$$

After implementing the finite element discretization, the coupled finite element matrix equation is

$$\begin{bmatrix} \boldsymbol{M} & 0 \\ 0 & 0 \end{bmatrix} \begin{bmatrix} \ddot{\boldsymbol{u}} \\ \ddot{\boldsymbol{V}} \end{bmatrix} + \begin{bmatrix} \boldsymbol{C} & 0 \\ 0 & 0 \end{bmatrix} \begin{bmatrix} \ddot{\boldsymbol{u}} \\ \ddot{\boldsymbol{V}} \end{bmatrix} + \begin{bmatrix} \boldsymbol{K} & \boldsymbol{K_z} \\ \boldsymbol{K_z^T} & \boldsymbol{K_d} \end{bmatrix} \begin{bmatrix} \boldsymbol{u} \\ \boldsymbol{V} \end{bmatrix} = \begin{bmatrix} \boldsymbol{F} \\ \boldsymbol{L} \end{bmatrix}, \qquad (3.30)$$

$$\boldsymbol{M} = \int \boldsymbol{\rho N_u N_u^T dv} \qquad (3.31)$$

The damping matrix (C) may be used in harmonic, damped modal, and transient analyses and substructure generation. In its most general form, it is:

$$\boldsymbol{M} = \boldsymbol{\alpha M} + (\boldsymbol{\beta} + \boldsymbol{\beta_c})\boldsymbol{K} + \sum_{j=1}^{N_m}\left[\left(\boldsymbol{\beta_j^m} + \frac{2}{\Omega}\boldsymbol{\beta_j^\xi}\right)\boldsymbol{K_j}\right] + \sum_{k=1}^{N_e}\boldsymbol{C_k} + \boldsymbol{C_\xi} \qquad (3.32)$$

Where: $\boldsymbol{\beta_j^\xi}$ frequency-independent (constant stiffness matrix coefficient for material j, Ω - circular excitation frequency) and K_j the portion of structure stiffness matrix based on material j; Ne is the number of elements with specified damping (C_k - element damping matrix, C_ξ - frequency-dependent, damping) ,C is the structural damping matrix, a is the mass matrix multiplier; M is the structure mass matrix; β is the stiffness matrix multiplier; β_c is the variable stiffness matrix multiplier; K is the mechanical structure stiffness matrix; N_m is the number of materials with $\boldsymbol{\beta_j^m}$(stiffness matrix multiplier for material j).

For structural analysis one of the main parameter is mechanical structural stiffness it is a matrix method that makes use of the members' stiffness relations for computing member forces and displacements in structures which is depicted in Equation (3.33) :

$$\boldsymbol{K} = \int \boldsymbol{B_u^T}\, \boldsymbol{cB_u dv} \tag{3.33}$$

Dielectric conductivity:

$$\boldsymbol{K_d} = -\int \boldsymbol{B_V^T}\, \boldsymbol{\varepsilon B_V dv} \tag{3.34}$$

Piezoelectric coupling matrix:

$$\boldsymbol{K_z} = -\int \boldsymbol{B_u^T}\, \boldsymbol{eB_V dv} \tag{3.35}$$

Where K_d is dielectric conductivity, K_z is piezoelectric coupling matrix, F is a vector of nodal forces, surface forces, and body forces. The electrical load vector L is a vector of nodal surface and body charges.

3.2.2.1.1 Vibrational simulation Results

The proposed piezoelectric cantilever beam was designed using COMSOL Multiphysics, as shown in Figure. 3.5. The cantilever beam structure consisted of three materials. Shape memory alloy as a substrate, PVDF, and Lithium Niobate as piezoelectric layers. The substrate material was in the middle position, while PVDF and Lithium Niobate were put on the substrate's top and bottom surfaces. The properties of all the materials have been shown in Table 1. The dimension (length × width × thickness in mm) of Lithium niobate piezoelectric layers was 60 × 10 × 0.5. The size (length × width × thickness in mm) of shape memory alloy substrate was 60 × 10 × 0.17. The dimension (length × width × thickness in mm) of PVDF was 55 × 10 × 0.028. The cantilever beam was clamped for 5 mm in the length direction on the fixed end, and the free end's thickness became 55 mm. All the different parts, the substrate, piezoelectric layers, and the base of the beam were assembled using union operation in COMSOL.

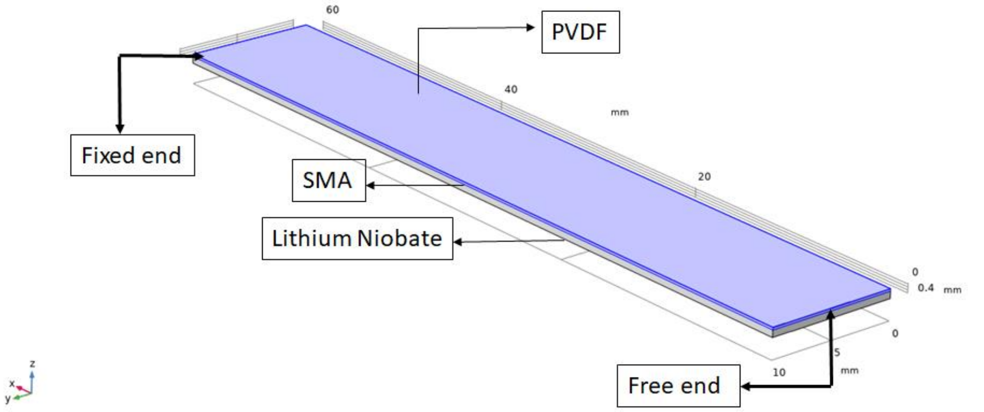

Figure 3. 5 Tri-layered piezoelectric cantilever beam.

The mechanical and electrical properties of the cantilever were analyzed with COMSOL Multiphysics. In solid mechanics physics, the beam's boundary conditions, such as free end, fixed end, applied vibration, and damping of the beam materials, have been set up. The base part of the beam was kept fixed. At the same time, the rest of the cantilever beam was under free conditions. We noticed that while applying vibration, the free part showed displacement. Here the value for the Mechanical damping for all three layers was chosen as 0.001 as it is the smallest damping value that can be used in COMSOL Multiphysics. At the same time, the acceleration level was set to be 2 g. During the boundary conditions of electrostatics physics, the piezoelectric layers' top and bottom surfaces were used as a terminal. The two rest faces of the layers were used as ground. To get the electrical response, the electrostatics physics was coupled with electrical circuit physics.

Then for meshing, tetrahedral mesh with adequate element size was used for the discretization of the beam. To determine the eigenvalue of the beam, the eigenfrequency analysis was performed. Finally, two frequency domain analyses were conducted for the cantilever beam: frequency dependence and load dependence.

Table 3.1: Material properties

Properties	Materials		
	Lithium niobate	PVDF	SMA
Young’s modulus (GPa)	170	2.45	83
Poission’s ratio	0.25	0.34	0.33
Density (Kg/m^3)	4700	1780	6450

The energy conversion from mechanical energy to electrical energy will be maximum when the piezoelectric cantilever beam is driven at its resonant frequency. Mechanical properties of the beam, such as displacement and stress, were analyzed. In the displacement analysis, the beam's vertical displacement was measured in the frequency domain of 250 Hz- 600 Hz, as shown in Figure 3.6(a). The Figure presents the maximum displacement curve of the beam's free peak at 372 Hz, which is 17.2 µm Figure 3.6 (b) shows Vertical displacement contour at the resonant frequency.

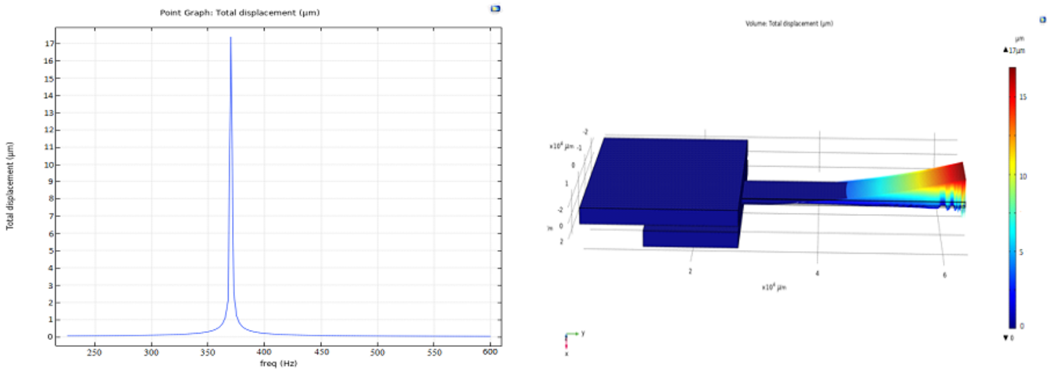

Figure 3. 6 a) Vertical displacement curve of the beam, b) Vertical displacement contour at the resonant frequency of 372 Hz

The measured stress generated in the beam was 4.06×10⁴ N/m² at the resonant frequency of 372 Hz. The beam's electrical properties, such as voltage output versus the frequency range and output power regarding load resistance, were analyzed. As the piezoelectric cantilever beam was driven under vibration force, a voltage output can be provided due to the piezoelectric effect. The generation of voltage output was analyzed in the frequency domain analysis of 250 Hz – 600 Hz at vibration acceleration of 2 g, as shown in Figure. 3.7(a). The output voltage was around 15 V at 372 Hz. Also, at a lower acceleration level (1g), the voltage response is in a good range of values, with the peak voltage around 6V. We also noticed that the output voltage was increased with increasing acceleration. Moreover, the power output was analyzed with the load resistance under the acceleration of 2g, as shown in Figure. 3.7(b). We observe that the power output was dependent on the load resistance as the load was increased up to 180 kΩ. A maximum power output of 16 µw was achieved with a load resistance of 180 kΩ at a resonant frequency of 372 Hz. After that peak point, output power decreases. So, the optimal resistive load for the harvester is 180 kΩ.

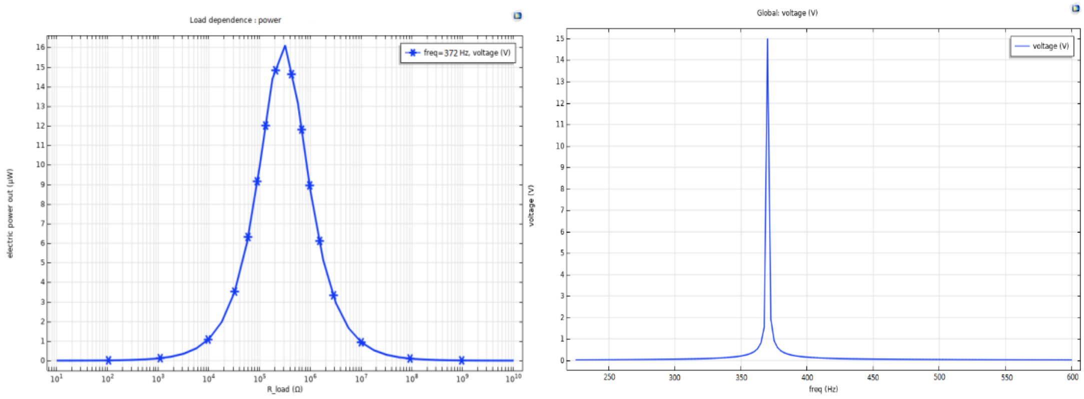

Figure 3. 7 a) Output power versus the load, b) Output voltage versus the frequency.

3.2.3 Thermal simulation

One of the significant studies in this research is to observe the effect of heat transfer on the energy harvesting device. We performed an analysis to see the temperature distribution using COMSOL Multiphysics. For this specific study, we used the model which consists of heat transfer and a laminar flow module. For that, heat transfer in solids in the heat transfer module was used. The time-dependent energy equation is as follows:

$$\boldsymbol{d_z\rho C_p\frac{\partial T}{\partial t} + d_z\rho C_p.u\nabla T + \nabla T.q = d_zQ + q_0 + d_zQ_{ted}} \tag{3.36}$$

Where C_p is the heat capacity (J/ (kg ·K)), ρ is the density (kg/m^3), T is the absolute temperature (K), u is the velocity (m/s), Q is the power density (W/m^3), Q_{ted} is the thermoelastic damping and q represents the heat flux vector which is described by:

$$\boldsymbol{q = -d_z\nabla T} \tag{3.37}$$

Where k is the thermal conductivity (W/ (m · K)). This is Fourier's law of heat conduction. The laminar flow module is based on Navier-Stokes equations as follows:

$$\boldsymbol{\frac{\partial\rho}{\partial t} + \nabla.(\rho u_2) = 0} \tag{3.38}$$

Where $\boldsymbol{\rho}$ is pressure (P a), u_2 is the velocity (m/s), I is the unity tensor, μ is the dynamic viscosity (P a · s), F is the volume force vector (N/m^3), g is the acceleration of gravity. Equation (3.38) is the continuity equation representing the conservation of mass, and Equation (3.39) represents the conservation of momentum.

$$\rho\partial u_2/\partial t + \rho(u_2.\nabla)u_2 = \nabla.\left[-pI + \mu(\nabla u_2 + (\nabla u_2)^T) - \frac{2}{3}\mu(\nabla.u_2)I\right] + F + \rho g \tag{3.39}$$

3.2.2.2.1 Thermal simulation results

This section will give insight into the thermal simulation as heat transfer is one of this research's main study. We conducted this study in two-dimensional space instead of three-dimensional that consists of a model composed of heat transfer and a laminar flow module for heat transfer simulation. We assumed a closed atmosphere filled with air for this model. We have used the heat transfer module in solids and fluids for this study. In Figure 3.8, we can see the result conducted for heat transfer study, which was done from 85 °C of the heat source to 20 °C of the Cantilever beam, and the mode of heat transfer was through the air by both convection and conduction in three-dimensional space at a stationary condition.

We conducted two studies. One study was stationary study, and the other was a time-dependent study. In the static analysis, we calculated the change in temperature of the whole system. In the time-dependent study, we focused on the shift in temperature of the cantilever with time. It is worth mentioning that as the time-dependent research was a time-consuming process and very complicated, we conducted this study in two-dimensional space. For this heat transfer study, a closed atmosphere was created.

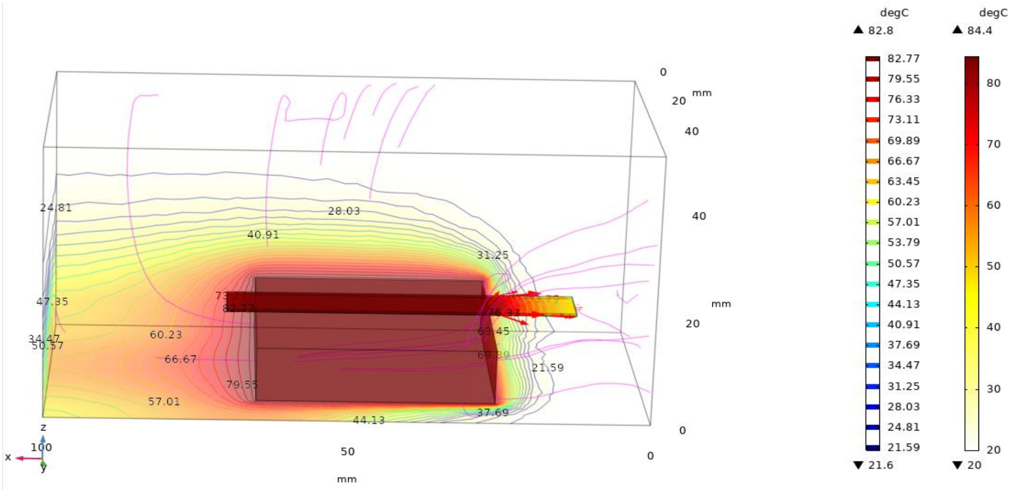

Figure 3. 8 Simulation of temperature distribution inside the box.

To define a closed system's boundary conditions, the outer box in Figure 3.8, is assumed as an arbitrary enclosure for the air where both inlet and outlet of fluid flow were defined. After determining the inlet-outlet requirements for the fluid (air), The meshing between the heat source and beam is particularly paramount to ensure heat transfer through the fluid, for meshing physics-controlled extra-fine meshing was used. Figure 3.9 shows meshes in the time-dependent simulation of the whole system in two-dimensional space. The heat source's temperature represents the temperature at the point indicated by the yellow square and beam temperature in the red square.

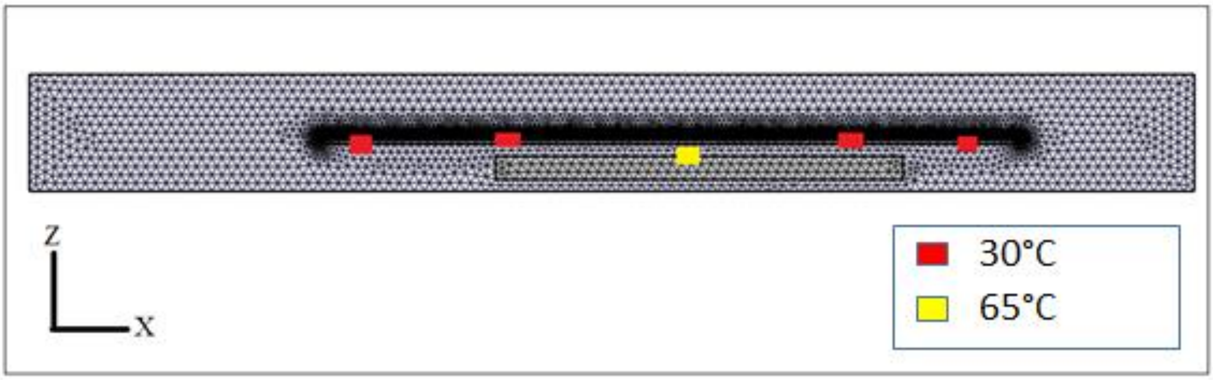

Figure 3. 9 Two-dimensional meshes for a time-dependent simulation.

Table 3.2: Detail of simulation

	Figure 3.8	Figure 3.9
Domain	Three-dimensional space	Two-dimensional space
Study	Stationary	Time-dependent
Mesh	Tetrahedral	Triangular
Number of degrees of freedom	82,026	37,430

Another important parameter was to design a heating source that can continuously heat and cool down the cantilever. The designed heating sources temperature was continuously fluctuating between 20 ◦C to 85 ◦C at 0.01 Hz for 100 seconds. After that, we calculated the temperature change both on the heating source and the cantilever's whole surface. Figure 3.10 shows the temperature over the time at the heat source point and of the beam. Conditions of simulations are given in Table 3.2.

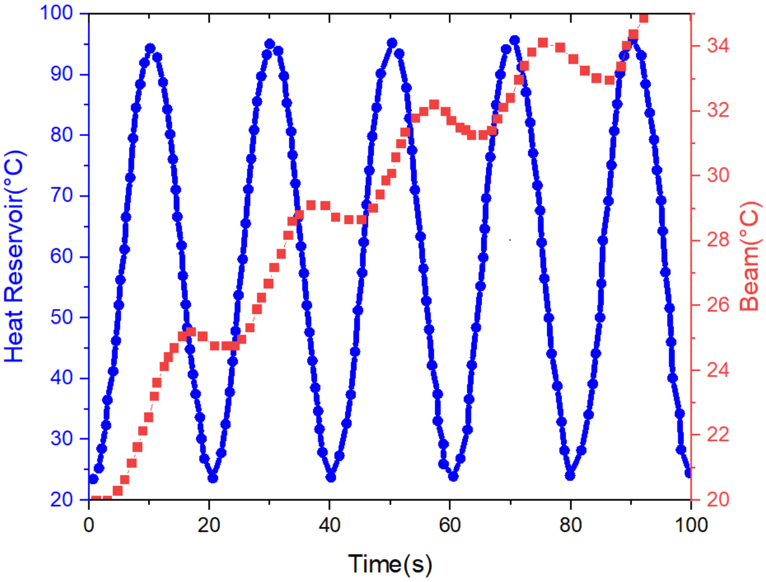

Figure 3. 10: Simulation of time-dependent change in temperature.

3.2.4 Fabrication Process

The fabrication process started by gluing three different layers together with different properties. The three layers are: polymer PVDF (from Piezo Systems Inc.,), single-crystal $LiNbO_3$ (from Roditi Systems Inc.), and metal Shape memory alloy (Nitinol- 55:45 Ni: Ti from Nexametals). To make a hybrid structure with all three materials to serve as a single beam, a mixture of silver glue and epoxy is used. The resulting tri-layer plate is heated inside an oven at 120 degrees Celsius for one hour and then cooled down to solidify the bond. After that, a laser machine (Siro Lasertec GmbH, Pforzheim, Germany) is used to cut each design following its CAD model. To measure charge output, wires were attached to the beam on top and bottom of the cantilever with the conductive silver epoxy glue on both sides of the cantilever and the series connection of the cantilever.

Three prototypes were fabricated,Figure.3.11, illustrates all three of them, the structures of the piezoelectric cantilevers in terms of materials arrangement have been compared LSP (Lithium Niobate as the top layer Shape memory as middle and PVDF as the bottom layer), LPS (Lithium Niobate as the top layer PVDF as intermediate and Shape memory alloy as the bottom layer) PLS (Shape memory alloy as the top layer Lithium Niobate as the middle and PVDF as the bottom layer). It is incredibly attached to a rectangle domain to clamp the prototype on the experimental bench support. The fabricated cantilever with the different placing of the material could resonate under 400 Hz of the frequency range.

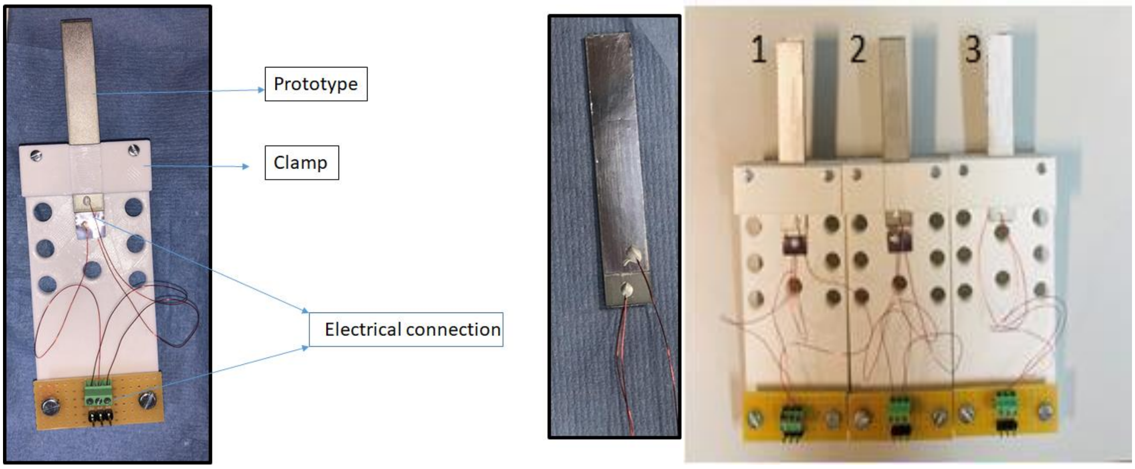

Figure 3. 11 Final prototypes with the electrical connection with three different configurations 1) LSP 2) SLP 3) LPS.

3.2.5 Vibrational energy harvesting experiments

This section presents the experimental benchmarks used to characterize the three configurations of piezo energy harvesting. This study was conducted to see how placing the materials plays a significant role in the harvester's output. In the literature survey, several design parameters have been studied to maximize the energy conversion from mechanical vibrations to electrical output. For obtaining the maximum output power the harvester's resonant frequency must match the frequency of the applied vibration source signal. These design primary parameters to be investigated involve as follows: 1) Material selection .2) Geometry and structure of different layers .3) Mode of operation d_{31} and d_{33}. 4)Fixation of piezoelectric cantilever. Which can see in the respective Figure.3.12, the experimental setup consists of a shaker used to produce the mechanical vibration.

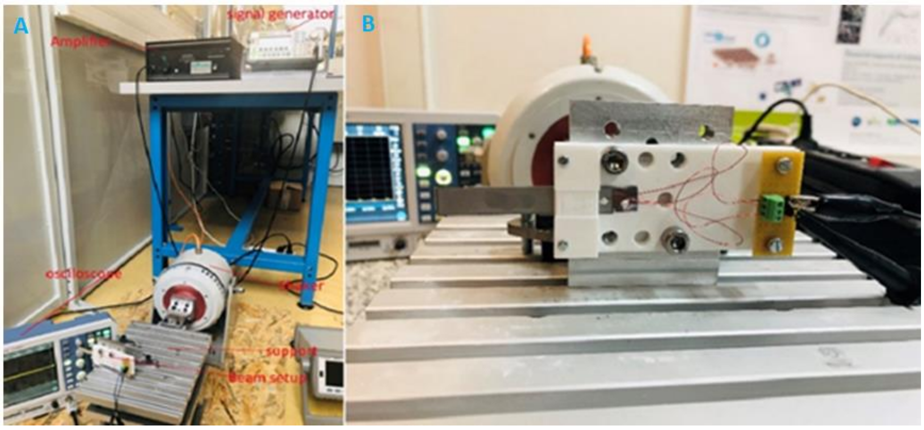

Figure 3. 12 A) The whole experimental setup B) Image of the transducer.

The shaker is excited at the natural frequency of each cantilever and driven by a sine wave from a function generator (RIGOL Technologies DG1022 20 MHz waveform generator) amplified by a power amplifier (RESONANCE FG Power Amplifier). The output voltage of the three cantilevers are measures and displayed by an oscilloscope with 4 inputs. The designs are clamped by a 3D printed support designed with AutoCAD.

To test the harvester's prototypes, the cantilever beams were clamped to the electromagnetic shaker. The shaker is excited by an amplifier module to generate vibrations. Under this vibration excitation, the harvester produces A.C. electrical output. Then, the output signal from the harvester are each connected to a Resistive variable load. The 4-channel oscilloscope is still used to perform real-time measurements. The vibration frequency and its excitation level (amplitude) are varied to test the harvester's performance. The maximum voltage and maximum power are used to evaluate the system's performance. Each harvester produces the maximum voltage when it works under the excitation frequency that is close to its resonant frequency. Figure.3.13 shows the generated voltage from one harvesting system (LSP) without any tip mass. It is observed that the resonant frequency of the configured harvester is under 370 Hz. Under this excitation frequency, the output power and voltage reached their best maximum value equal to 1 µW and 12.2 $V_{p-p,}$ (RMS voltage is 4.24 V) respectively.

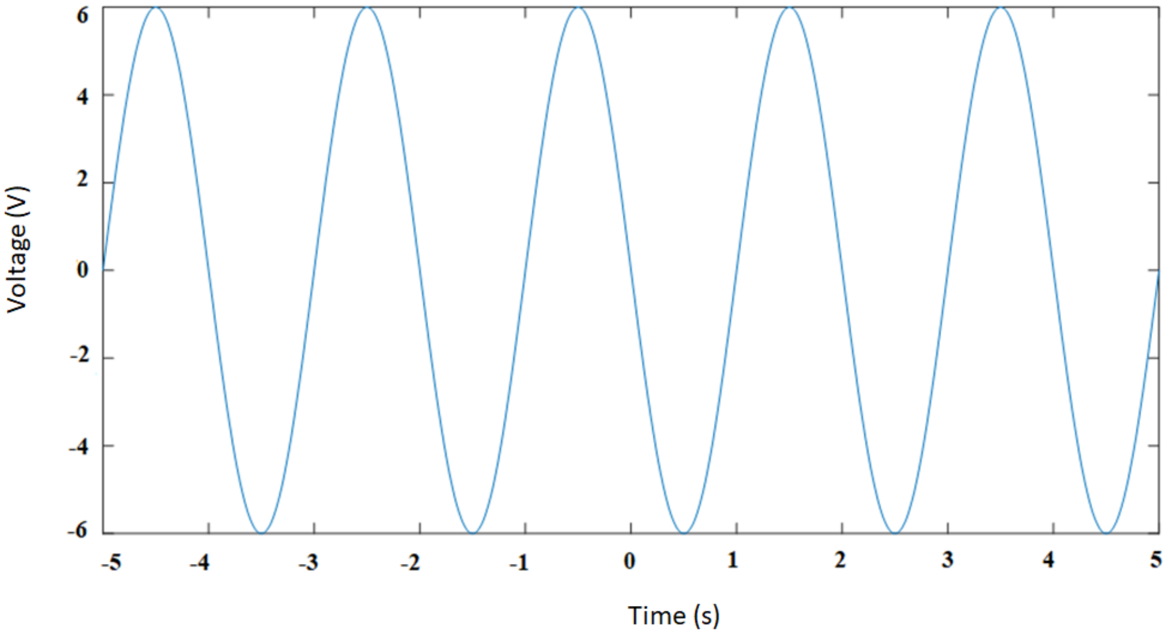

Figure 3. 13 Experimental output voltage.

Formula (3.40) also calculates the output power. With this output power, we calculated the RMS current, the results are presented in Figure 3.14.

$$P = I_{RMS} \times V_{RMS} \tag{3.40}$$

Where I is the output Current, and V is the output Voltage, and RMS is Root Mean Square

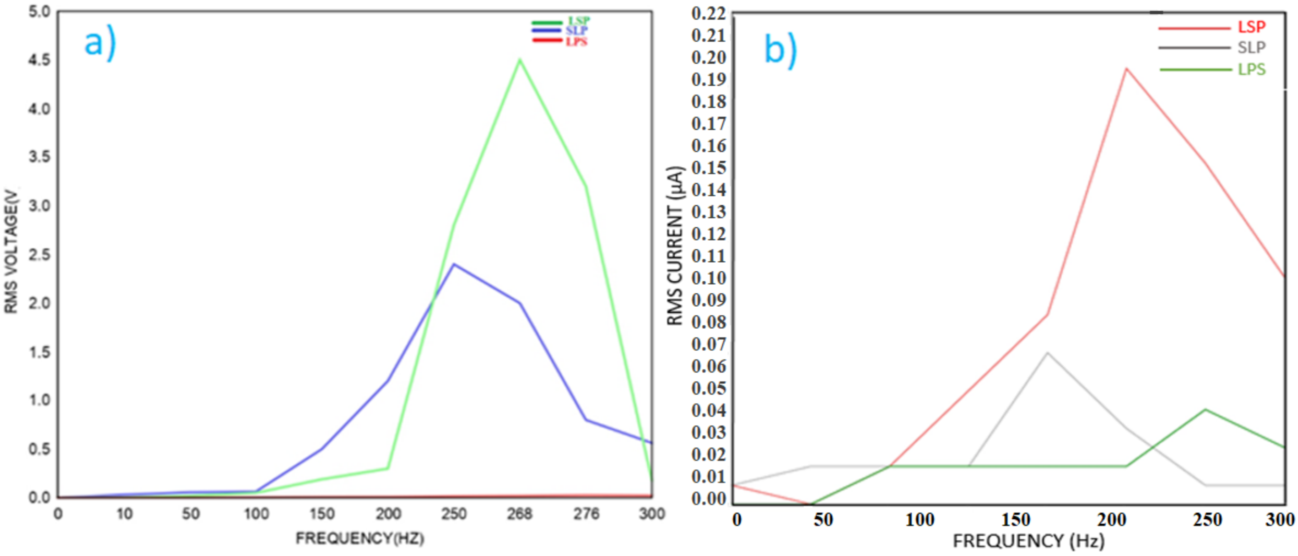

Figure 3. 14. a) RMS Voltage, b) RMS current for all the three different configurations.

Besides calculating the output voltage and power, we also measured the device's internal impedance. We have used an impedance analyzer to investigate the equivalent circuit parameters at resonance to obtain the properties of the piezoelectric element. In Figure.3.15, we can see the measured values for the clamped cantilever in terms of impedance for the LSP configuration.

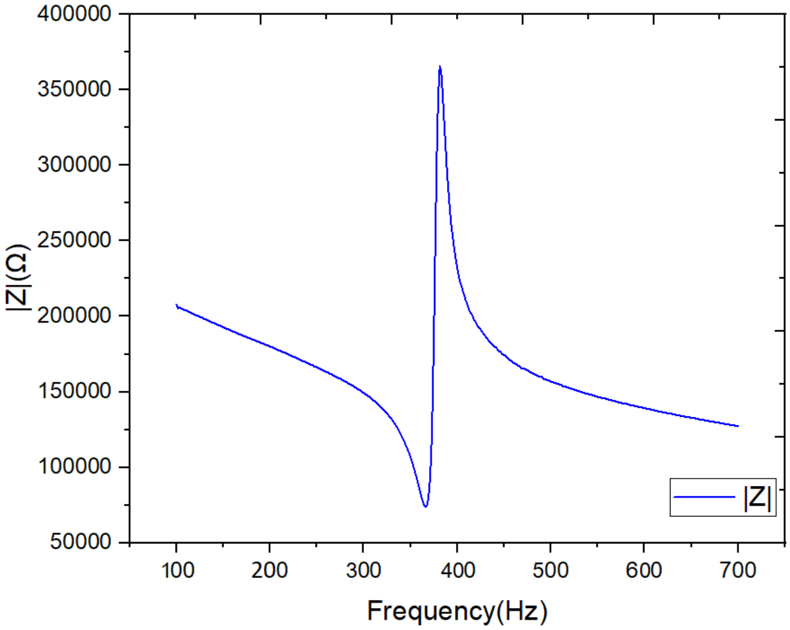

Figure 3. 15 Measurement of impedance and phase.

The dielectric loss was minimal (<5%), confirming the excellent quality of the materials has been used, as we have used single-crystal lithium niobate shown in Figure.3.16. The measured were done at room temperature.

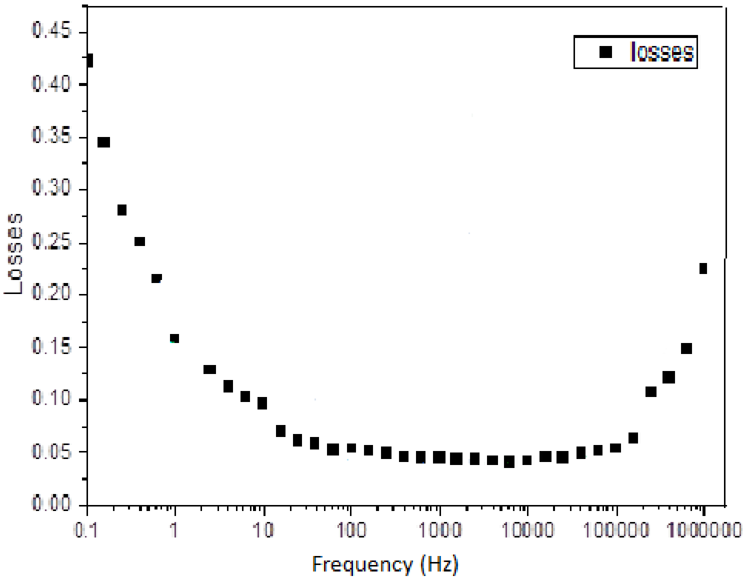

Figure 3. 16 Losses calculation for the harvester.

The cantilever configuration characterized showed 0.9 nF capacitance. To calculate the cantilever's maximum charge, we have used a setup consisting of a force sensor and a piezoelectric stack actuator to apply a dynamic strain with a 0.5 Hz frequency and an amplitude range of 1.5 - 4.5 MPa, presented in Figure.3.17.

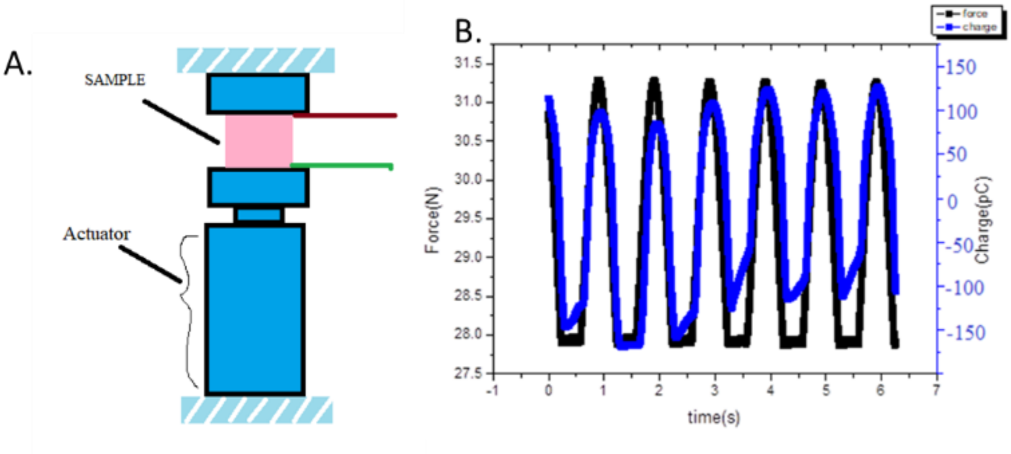

Figure 3. 17 a) Force Sensor. B) Measurement of generated Charges on the surface of the cantilever.

In this experiment, no tip mass is mounted on the cantilever. We experimented with all three cantilevers with different configurations (LSP, SLP, LPS) and compared the cantilevers' results. Figure 3.18 shows the frequency dependence of the dielectric constant and the loss of LSP configuration measured at room temperature. The dielectric constant of the LSP configuration increased to approximately 15, as shown in Figure 3.18. Moreover, the dielectric loss of the LSP configuration shown low values at frequencies depicted in Figure3.18.

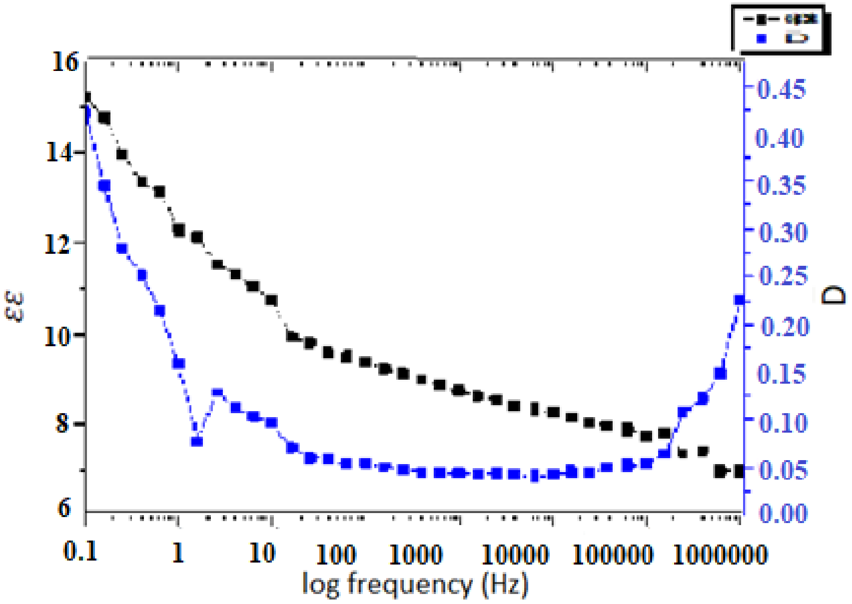

Figure 3. 18 *Dielectric constant and loss of LSP configuration as a function of measure frequency.*

3.2.6 Thermal energy harvesting experiments

A specific thermal oven was used to characterize the thermal energy harvesting functioning of our designs for the Pyro measurements. The humidity, the temperature and the temperature velocity can be controlled very precisely with this machine", for instance Figure.3.19 illustrates a desired evolution of the temperature that will be applied to the harvesters. The machine has a Multi-Touch-Display in the front where one can see buttons for elementary functions such as start/stop, fixed-value/automatic operation, interruption, light, etc. the machine is connected to a computer where one can use USB for saving data. While working with this machine, we can choose the heating rate and temperature range, which gives us the freedom to design our heating and cooling cycles. The temperature range is -40°C to 300°C which is sufficient for the expected range of temperature of our application and limitation. For, instance, with PVDF in our system work till 100°C, and it starts degrading beyond this. In case of Lithium Niobate, which is stable even at high temperatures. For future work, a different design without PVDF to can be studied to work in very high temperatures.

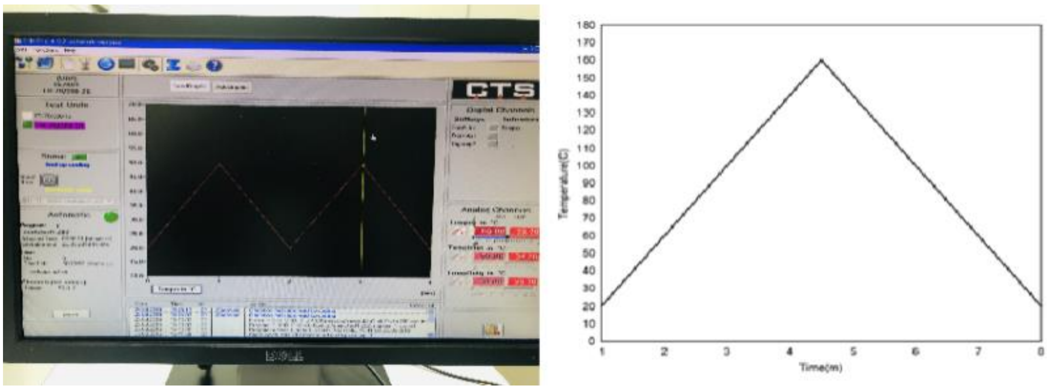

Figure 3. 19 *Display of the machine and proposed thermal cycle of the characterization.*

Firstly, we put the sample inside the machine and lock the doors. Then proposed heating and cooling cycle in Figure 3.19 with 30°C/min is applied: starting from 20°C, increasing up to 160°C and cooling again down to 20°C. The CID software was used for programming and documentation on the machine.

Once the cycle is defined, the machine runs during the time specified by the user during the programming. In our case we used an experimental duration of 8 min. Once the experiment is started, the output voltage can be observed in real-time with the oscilloscope connected with the sample. We observed that the voltage fluctuated with the machine's temperature change, and we tried to measure the maximum output voltage for the defined cycles. For all the three samples, i.e. LSP, LPS and PLS, we applied the same thermal processes to compare their pyro effect with the temperature excitation. The samples were tested in an air dryer atmosphere while a water-cooled cooling compressor was used in the machine. Figure.3.20. A) and B) Shows machine and its interior space respectively Figure.3.20. C) shows the bending cycle of the beam. Where (a) the beam and source are at the cooling stage, (b) the source and the beam are at the heating stage leading to the deflection of the beam, (c) the beam and source are at the cooling stage, and (d) the source and the beam are at the heating stage again.

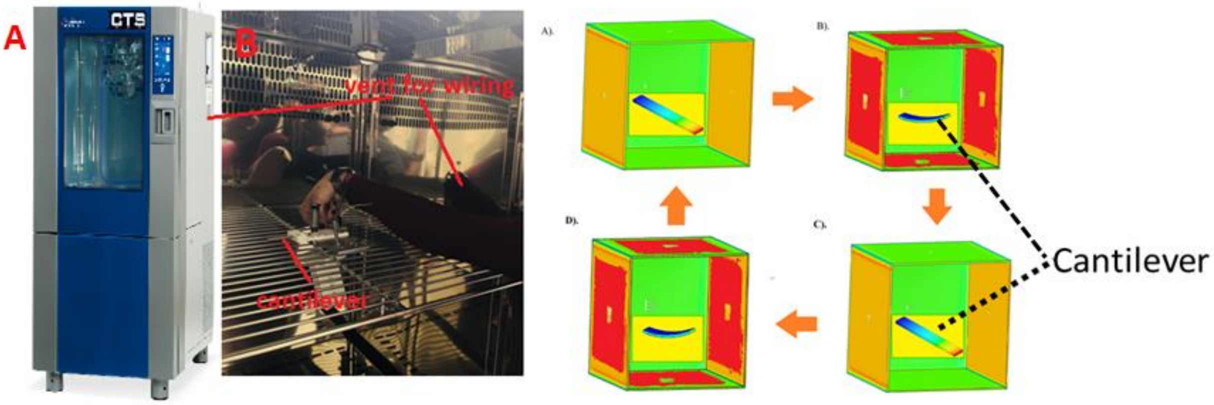

Figure 3. 20 a) CTS Machine, b) placing of the cantilever inside the machine, c) Schematic of the heat cycle of the beam.

Figure 3.21 shows the device's open-circuit output voltage and the temperature cycle designed in the CTS as a function of frequency. We noticed that with the rise in frequency, the output voltage started decreasing. It can be concluded that with an extended heating period, the cantilever was able to give better output as it can stay in contact with the heating source for a more extended period. Here in Figure 3.21. a filtered open-circuit output voltage graph is represented.

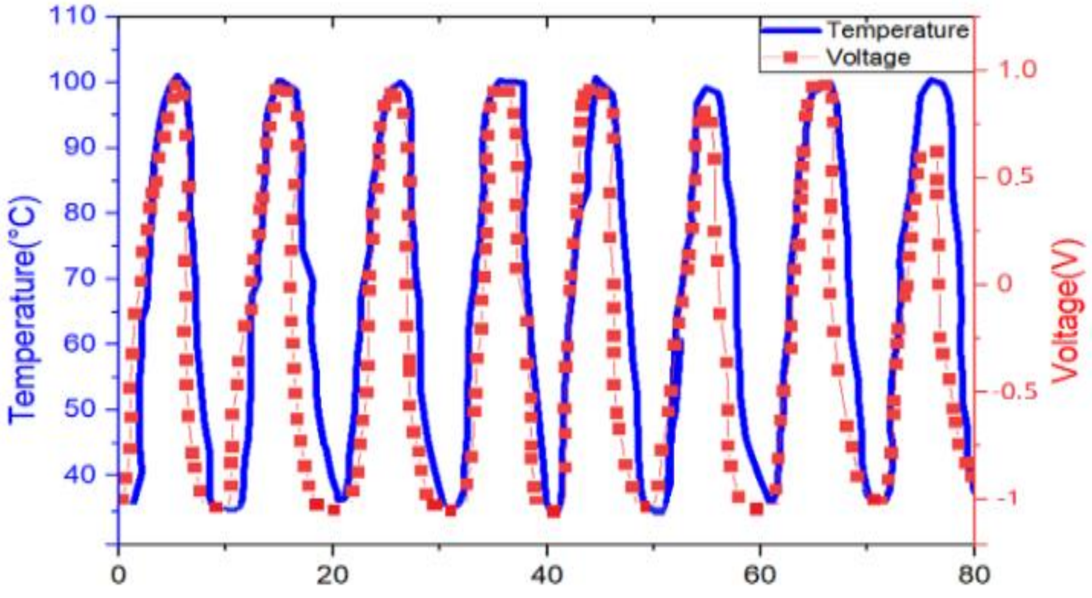

Figure 3. 21 Output voltage (red) and temperature (blue) for different (a) 0.1 Hz.

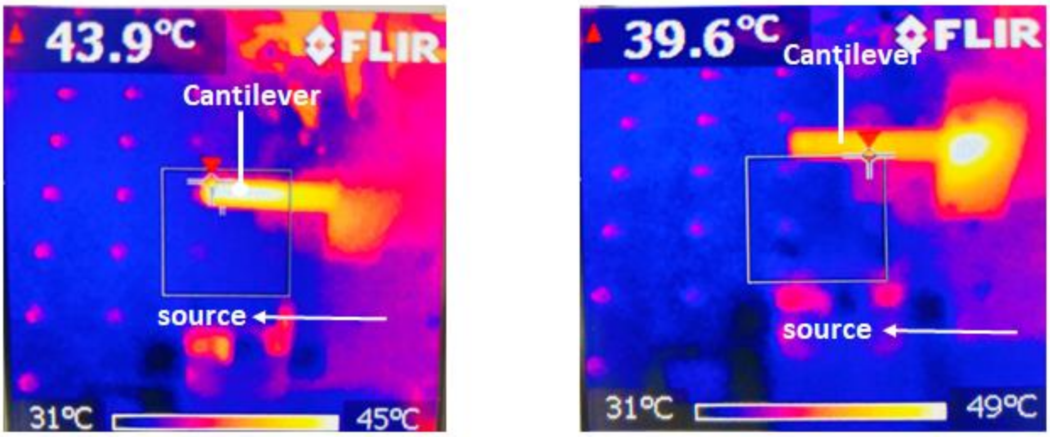

(a) (b)

Figure 3. 22 Measured temperature with a thermal imaging camera. (a) The heat source (oven) at 95°C and the cantilever temperature is 43.9°C. (b) The heat source is at 75°C and the cantilever temperature is 39°C.

As a conclusion, we can see from Figure 3.22 that when the heat source temperature raises the beam's temperature increases as well as its deflection. Furthermore, the Pyro electricity effect produce negative voltage under the cooling process. It showed a positive voltage when it was under the heating cycle.

3.3 A Six-Cantilevered based Energy harvester

Many researches work show that the standard designs such as linear piezoelectric energy harvesters are not a prominent solution as they can only operate in narrow bandwidth because of their single high resonant peak in their frequency spectrum. This section presents the simulation and experimentally validates a novel lead-free piezoelectric energy harvester to harness electrical energy from wideband, low-frequency, and low-amplitude ambient vibration. To reach this target, the harvester is designed to combine multi-frequency and nonlinear techniques. The proposed energy harvesting system consists of six piezoelectric cantilevers of different sizes and different resonant frequencies. Each is based on the lead-free material (single-crystal lithium niobate $LiNbO_3$) as the piezoelectric layer and shape memory alloy substrate. The design is in the form of a circular ring that embeds the cantilevers to create a nonlinear behavior when excited with ambient vibration. The finite element simulation and the experimental results confirm that the proposed lead-free harvester design is efficient at a different frequency below 250 Hz.

To harvest energy from surrounding with a broad and low-frequency range and low amplitude vibration, we propose a new VPEH structure design based on nonlinear functioning. The proposed method is based on a circular ring embedded with six cantilevers of different resonance frequencies and energy conversions. While the entire structure exhibits nonlinear functioning, allowing the low amplitude of vibration functioning, we use lead-free material (single-crystal Lithium Niobate LiNbO3) as the piezoelectric layer and Shape memory alloy as a substrate. Finite element simulation and experiments on the fabricated design are carried out and validate the functioning of the VPEH with the expected conditions, i.e., low amplitude, and low-frequency range. The fact that the material used is lead-free makes this harmless and makes the VPEH utilizable for daily life applications such as vehicles. It is worth mentioning that this section only aims for vibrational energy harvesting based on piezoelectric effects. We did not conduct the pyroelectric measurement for this given design as the main aim of this study is to overcome the narrow range of energy harvesting for VPEH.

3.3.1 Design of multiresonting Piezoelectric Energy Harvester

The proposed nonlinear piezoelectric energy harvesting system of this study is shown in Figure.3.23. This energy harvesting system is made of six cantilever beams and monobloc with a circular ring. The Monobloc ring and six cantilevers have two layers: a lithium niobate (LiNbO3, 127.8° Y-cut, from *Roditi systems Inc.*) layer, which is a lead-free piezoelectric material, and a shape memory alloy (SMA) based on the nitinol material (composition is 55:45 Ni: Ti, from *Nexametals company*) which serves as a passive layer. To fabricate the structure, the first step consists of cutting down separately a LiNbO3 wafer and an SMA wafer to obtain the desired shape (circular ring with six cantilevers) for each. The cutting process is made with a femtosecond laser cutting machine with several distinct advantages: high resolutions (down to 25 nm), noncontact interaction, and can be applied to any substrate without specific conditioning [34]. After getting the desired shape, both the samples are bonded together using silver glue with epoxy and were kept in an autoclave for curing at 120°C of temperature for 1h 30. To add the electrodes, a mask is put, and gold sputtering is done on the Nitinol and Lithium Niobate on top and bottom surface. The six cantilever beams are of different lengths but have the same thickness and width. However, all six cantilevers are connected to the same electrodes to generate more electrical power than individual consideration. An important and attractive feature of this proposed energy harvester compared to the others described in the literature is that there is no need to apply the traditional tip mass to reach a relatively low frequency (less than 500 Hz). Indeed, the chosen materials (SMA combined with LiNbO3) with appropriate dimensions and the nonlinearity (embedding on a circular shape) allow the proposed structure to work at low frequency and low amplitude of vibration whilst the six cantilevers of different sizes allow a wide range of principal working frequency (six resonance frequencies). Finally, another feature of this proposed structure is its adaptability and simplicity of design: its form is easy to fabricate, duplicate, or modify, for instance, if one needs to put additional cantilevers to increase the frequency range and the output power.

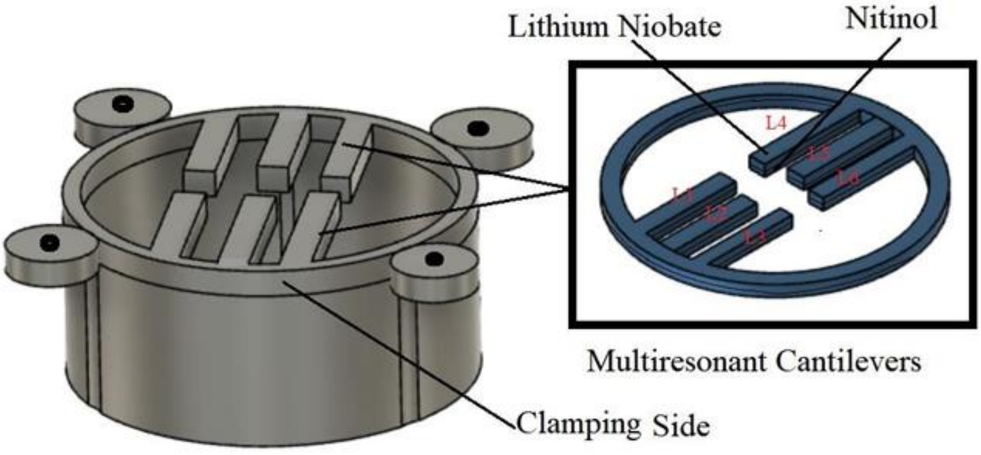

Figure 3. 23 Schematic of the proposed multi resonant piezoelectric energy harvester

The circular ring of the design has an outer diameter of 55mm and an inner diameter of 50mm. All six cantilevers have different sizes, which are illustrated in Table 3.3. The cantilever's best dimensions were selected based on the parametric study conducted, described in the next section.

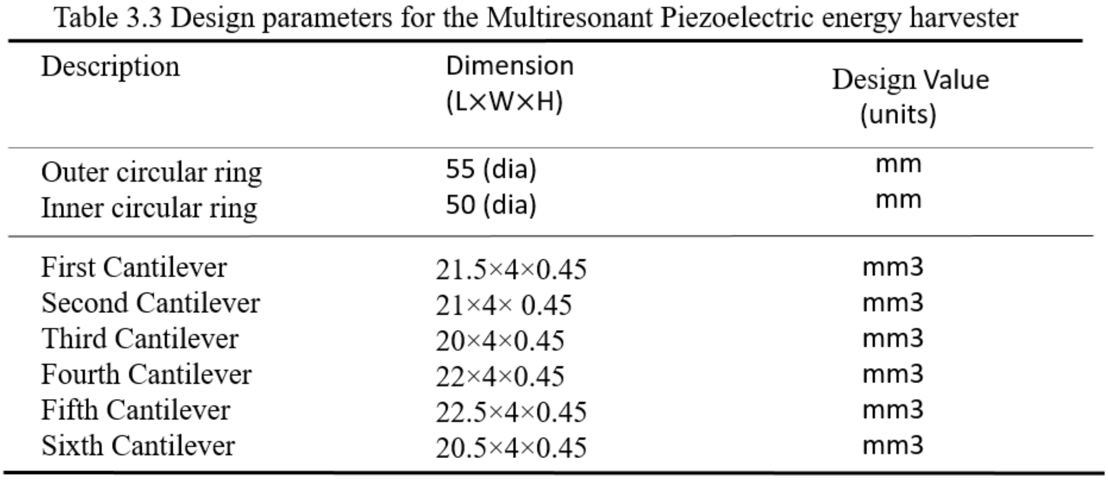

Table 3.3 Design parameters for the Multiresonant Piezoelectric energy harvester

Description	Dimension (L×W×H)	Design Value (units)
Outer circular ring	55 (dia)	mm
Inner circular ring	50 (dia)	mm
First Cantilever	21.5×4×0.45	mm3
Second Cantilever	21×4× 0.45	mm3
Third Cantilever	20×4×0.45	mm3
Fourth Cantilever	22×4×0.45	mm3
Fifth Cantilever	22.5×4×0.45	mm3
Sixth Cantilever	20.5×4×0.45	mm3

The choice of the cantilevers' dimensions allows tuning their resonance frequencies. Thus, to make the VPEH system performant for further analysis, we used finite element analysis COMSOL multiphysics software to optimize the cantilever beam's geometry. We are considering the parameters of the design along with the cantilever beam's material properties. Indeed, the material properties and geometry have an essential role to play as these properties affect the vibration response of the mutiresonant piezoelectric energy harvester, including the system's resonance frequency. A full parametric study is therefore done to find the cantilever beams' optimum lengths (L1, L2, L3, L4, L5, and L6) by using COMSOL Multiphysics as presented in the next section. This study's primary focus is to target a frequency range between 1 Hz and 500 Hz. We want to use this device in automobiles to power sensors present in them, as in those environments, the vibrating frequency is usually less than 500Hz. The objective is to optimize the geometry and determine the lowest resonance frequency without using the proof mass. Keeping in mind that the resonance frequency can be furthered tuned if we want to implement the proof mass. The proposed multiresonant piezoelectric energy harvester's fabricated prototype was experimentally tested under harmonic base excitation, as presented in the next section.

3.3.2 Finite Element Analysis of Multiresonant piezoelectric energy harvester

We have used COMSOL Multiphysics 5.5 software with "Piezoelectric Module" for the FEA study.

The whole geometry, including the ring with all attached six cantilevers, was modelled in 3D. Both the materials Lithium Niobate and Shape memory alloy (Nitinol) were selected from the material library. The simulation evaluated the bending, compression, and shear modes behaviours of the beam. The Lithium Niobate's material properties, along with the Nitinol, were the same as shown in Table 3.1. As mentioned in the last few studies, the resistive load must be set to 1 MΩ, which will behave as an open circuit condition.

The ring was kept as the fixed constraints for boundary conditions for performing the simulation, and the six cantilevers were selected as free. During the meshing in COMSOL Multiphysics software, the elements' size was chosen as 0.8mm while getting accurate results with minimum simulation time. Acceleration applied to the system was controlled at 1g. From the simulation, we can check the device's resonance frequencies and the output voltage achieved from the device. We know that the strain is directly related to the output voltage, so the higher will be the stress higher will be the output voltage. According to the literature [109], connecting different energy harvesting cantilever beam of the same thickness but with different lengths can produce higher output power. It was reported that the output power was increased from 2 μW to 5 μW, and the bandwidth was widened from (47, 55) Hz to (22, 88) Hz. Therefore, in this study, we decided to use the same thickness but different length cantilevers. In the next section, we presented the results of static structural analysis obtained from FEA. We compared the stress, strain, and deflection of the cantilever while changing the cantilever's length. An eigenfrequency analysis was also carried out to find the modes present for the device.

3.3.3 Parametric Study of Cantilever Beam

A parametric study was conducted on the cantilevers' length to analyze the impact of varying length (Section 3.3.3.1); the thickness of the beam being kept the same as 0.45 mm (combined thickness of

Nitinol with the Lithium niobate). A parameter sweep was also conducted to see how the acceleration (Section 3.3.3.2) will change the device's voltage.

3.3.3.1 Effect of the length of the cantilevers

Here in Table 3.4, we have presented the results we obtained for the cantilever beams with varying lengths of L1, L2, L3, L4, L5, and L6. With the modal analysis conducted, each design's first four natural frequencies are summarized in table 3.4. This study has been done to select the best geometry for creating a multi resonant piezoelectric energy harvester. However, it will also depend on the source of excitation. In this research, our focus was mainly on the frequency lower than 500 Hz. That's why we target a frequency range of 0-500 Hz.

Table 3.4 Representation of Various geometries with different beam length and their natural (NF: natural frequency (Hz))

	Geometry	**Cantilever with Changed length (mm)**	**Cantilever with same length (mm)**	**NF1**	**NF2**	**NF3**	**NF4**
1.	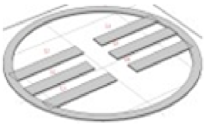	21.5 (L1)	22 (L2,L3,L4,L5,L6)	31	51	71	110
2.	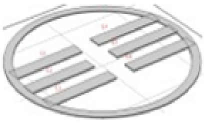	21 (L2)	22 (L1,L3,L4 ,L5,L6)	21	62	91	210
3.	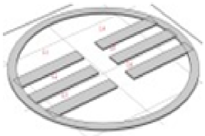	24 (L3)	22 (L1,L3,L4 ,L5,L6)	31	61	91	121
4.	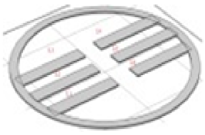	23 (L4)	22 (L1,L3,L4,L5,L6)	21	61	71	101
5.	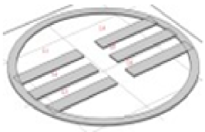	22.5 (L5)	22 (L1,L3,L4,L5,L6)	31	101	191	218
6.	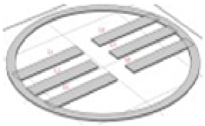	20.5 (L6)	22 (L1,L3,L4,L5,L6)	21	51	81	110

3.3.3.2. Effect of the Acceleration on the harvesting device

We conducted another study to analyze the acceleration impact on the device, among others we choose to work at 1g acceleration. Still, it was essential to know how the device will work at high or low acceleration to check the device's adaptability. The result is displayed in Figure.3.24 where se observe that the increase in the acceleration will result in an increase of the open circuit voltage of the device.

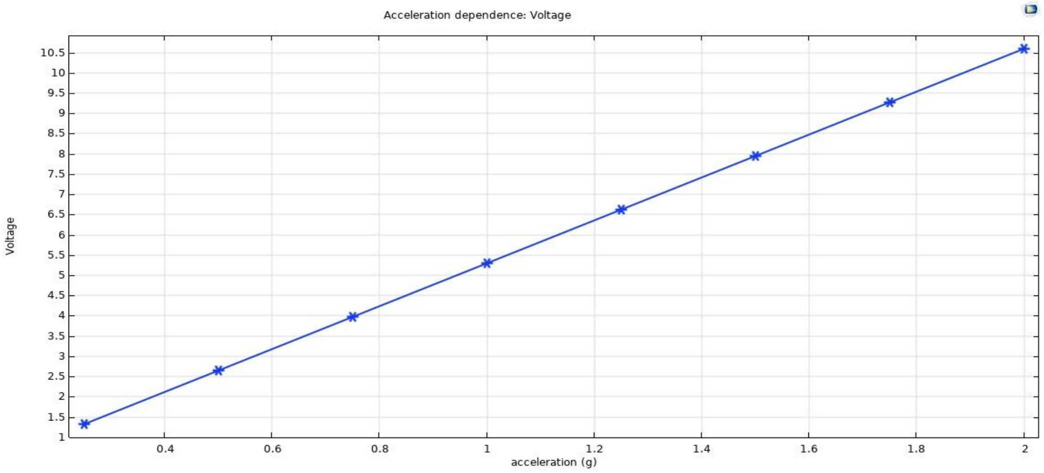

Figure 3. 24 Evolution of the output voltage versus the acceleration.

3.3.3.2.1 Modal and Harmonic Analysis of multiresonant Piezoelectric energy harvester

From the studies carried out in the previous section, we were able to select the desired cantilever lengths, without any proof mass. With the geometry of the different length of beams, modal and harmonic analyses are further carried out in this section.

3.3.3.2.1.1 Modal Analysis

In the Modal Analysis carried for the cantilever beam, we choose the resonance frequency with the high voltage values as all the first four frequencies for all the six cantilevers to come under 500 Hz. Hereafter, we represented the resonance frequencies with high voltage for the multi resonant piezoelectric energy harvester summarized in Table 3.5.

Table 3.5. Natural frequencies for the MPEH (FEA) (NF: natural frequency).

NF1	101
NF2	62
NF3	91
NF4	61
NF5	218
NF6	81

The total deformation shapes (of three main axes) for the first resonance frequency corresponding to Table 3.5 are illustrated in Figure.3. 25. Note that the red coloured part represents the maximum stress and maximum deformation.

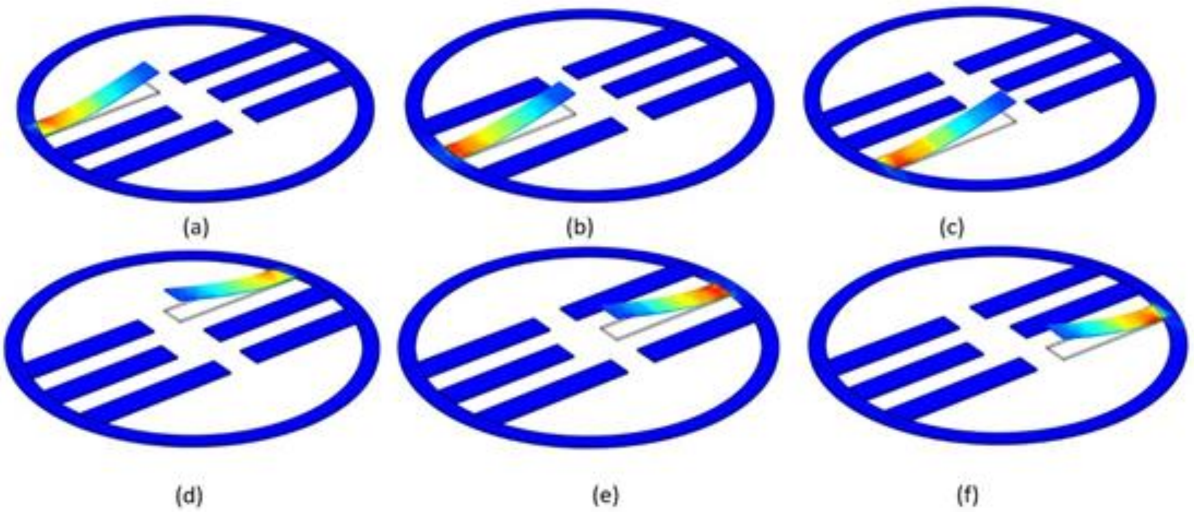

Figure 3. 25 Deformation shapes of all the six cantilevers for the resonances having the maximum voltage the results obtained from COMSOL Multiphysics modal analysis. (a) Cantilever1; (b) cantilever 2; (c) Cantilever 3; (d) Cantilever 4; (e) Cantilever5 ;(f) Cantilever 6.

3.3.3.2.1.2 Harmonic Analysis

To verify the results, we got from the modal analysis, we performed a harmonic analysis as well. For this particular study, the excitation is maintained at 1 g. Henceforth frequency response was evaluated, where we calculated the voltage and displacement for the multi resonant piezoelectric energy harvester. Again, the range of frequency is considered between 1 Hz to 500 Hz. The obtained results are presented in Figures 3.26 (a) and (b). While Observing Figure 3.26, maximum displacement and voltage are attained when the frequencies are closed to the resonance frequencies obtained from the modal analysis. This study indicates that the relation between the harmonic response analysis and modal analysis agrees closely.

The voltage against frequency response, as illustrated in Figure.3.6, shows similar behavior in which peak voltage is achieved at both resonance frequencies. We can see that at the resonance frequency, the cantilever (1) yields a maximum voltage of 3.3 V and the cantilever (2) produces 7.5 V, remaining cantilever (3), (4), (5), (6) yields a maximum voltage of 1.3 V, 1.7V, 0.2V, 1.3V respectively.

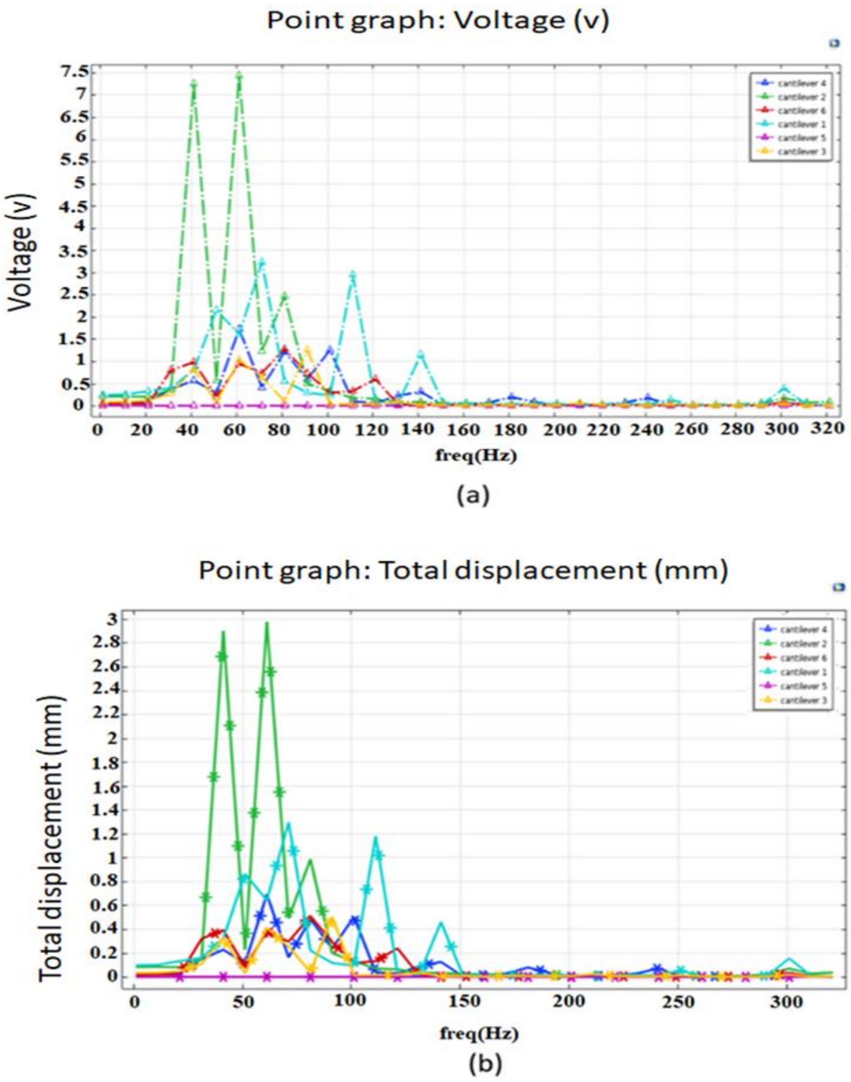

Figure 3. 26 Frequency responses of multi resonant piezoelectric energy harvester (a) Voltage and (b) Displacement obtained from FEA under 1g base excitation.

3.3.4. Experimental Validation

To validate the results, we got from the FEA simulation, an experimental study was carried out. The multi resonant piezoelectric energy harvester prototype was fabricated in a similar way that the previous section's design, with all cantilevers having different sizes. As the prototype is made up of a metal substrate (Nitinol) in the cantilever beam's shape, a Lithium Niobate layer is bonded over it.

As we can see in the respective Figure.3.27, the experimental setup consists of a shaker which is used to produce the mechanical vibration. The shaker excites at the natural frequency of each cantilever and driven by a sine wave from a function generator (RIGOL Technologies DG1022 20 MHz waveform generator) amplified by a power amplifier (RESONANCE FG Power Amplifier).

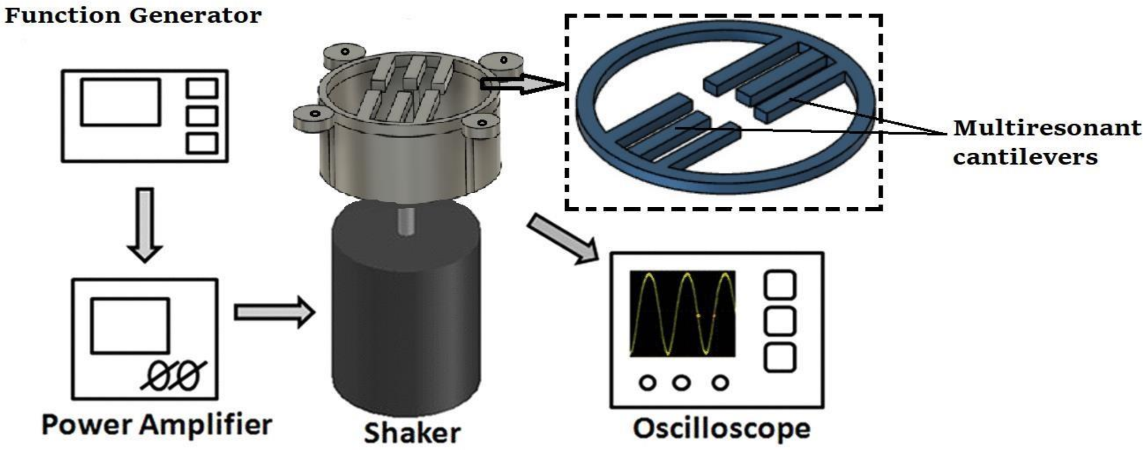

Figure 3. 27 Schematic of the experimental setup for the multiresonant Piezoelectric energy harvester.

The output voltage is measured by an oscilloscope of four inputs. The acceleration was measured at the cantilever beam's fixed base through an accelerometer (Dytran 3305A2, 0.3 to 5000 Hz, ±5%). The acceleration and the voltage generated were recorded by NI DAQ modules, NI 9234 and NI 9229, respectively, through Signal Express software. The schematic of the experimental setup and the fabricated prototype is presented in Figure 3.28 (a), (b), (c), where the whole experimental design, along with the close view of the clamping unit with the shaker, are represented, respectively.

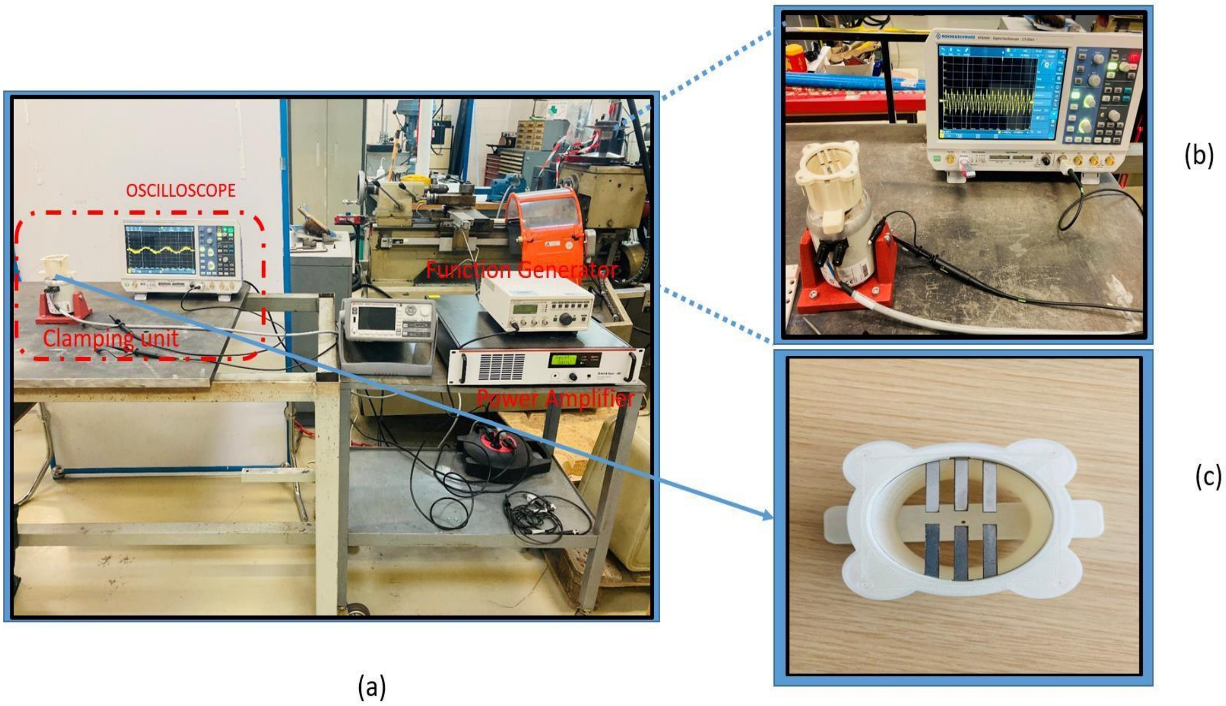

Figure 3. 28 (a)The experimental setup (b) the fabricated E.H. prototype attached on the shaker (c) the fabricated prototype.

3.3.4.1 Responses at Resonance

Experiments were performed at the resonance frequency of each cantilever. In this way, we could calculate and compare what we got from the FEA simulation results; the obtained results are displayed in Figure.3.29. It was found that at resonance for the first cantilever, the output Peak voltage for the system was 5 $V_{P,}$ and for the cantilever second, third, fourth, fifth, sixth is 4.5 $V_{P,}$ 6 V_P, 5.8 V_P, 5.5 $V_{P.,}$ and 1.5 V_P respectively. The third cantilever was the longest and cantilever sixth was the shortest in the following design.

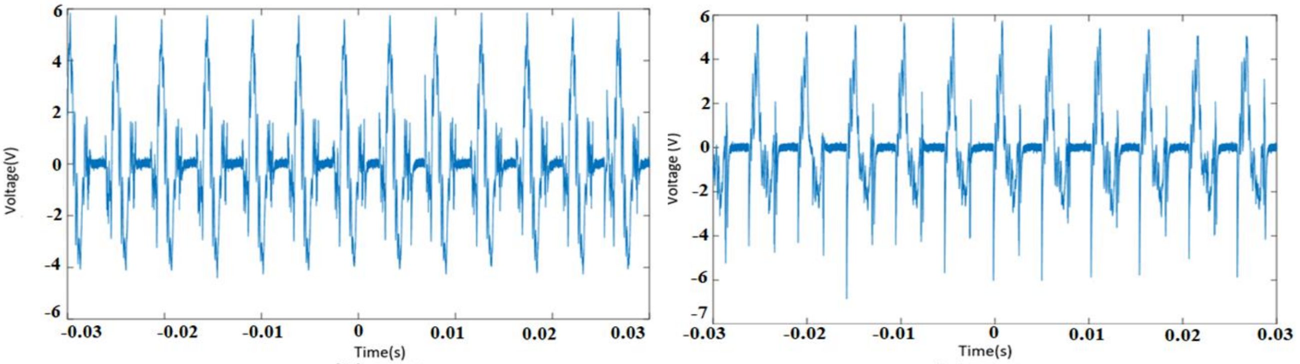

(b) 62 Hz (a)75 Hz

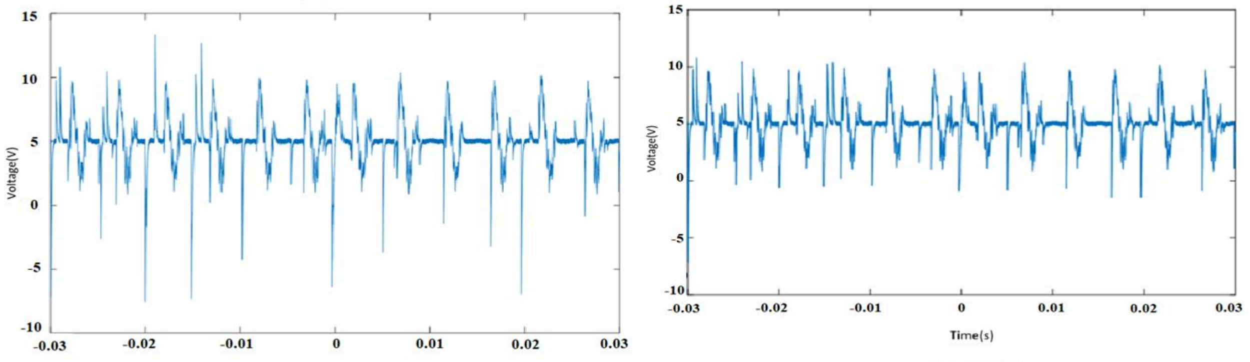

(f) 80 Hz (e) 194 Hz

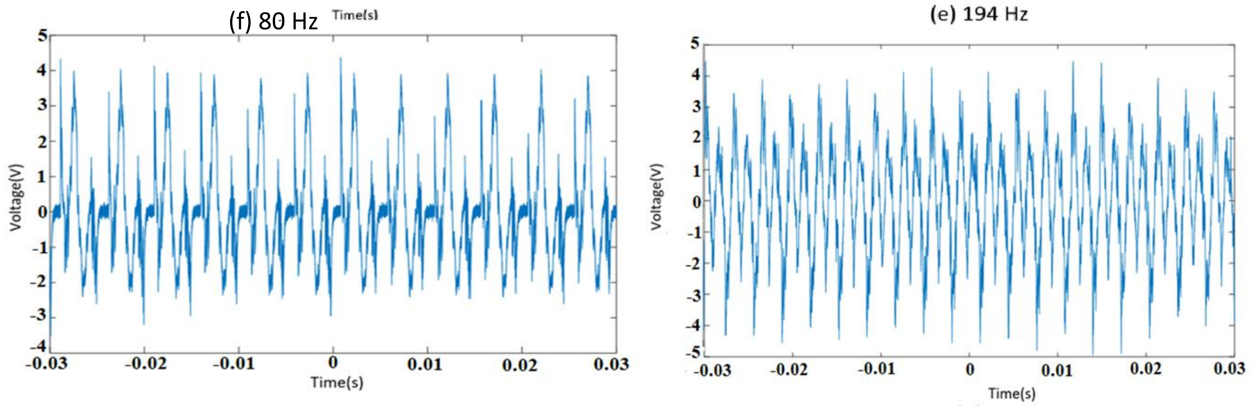

(c) 85 Hz (d) 61 Hz

Figure 3. 29 The output voltage of the multi resonant piezoelectric energy harvester at their respective resonance frequencies (a) third cantilever (b) fourth cantilever (c) fifth cantilever (d) firth Cantilever 4 (e) second cantilever (f) sixth cantilever.

3.3.4.2 Comparison of experimental results with simulation results

To validate the output voltage, we got from the FEA simulation, we compared them with the experimental results. More precisely we synthesize in a table the percentage of error we observed in the FEA simulation results relative to the experimental results, see Table3.6. In the meantime, in Figure

3.30, we present (a) experimental results and (b) FEA Simulation results. While the error is very small, it is worth mentioning that the resonance frequencies were similar in experimental and simulation results. As a conclusion, the experimental and the simulation results are in good agreement.

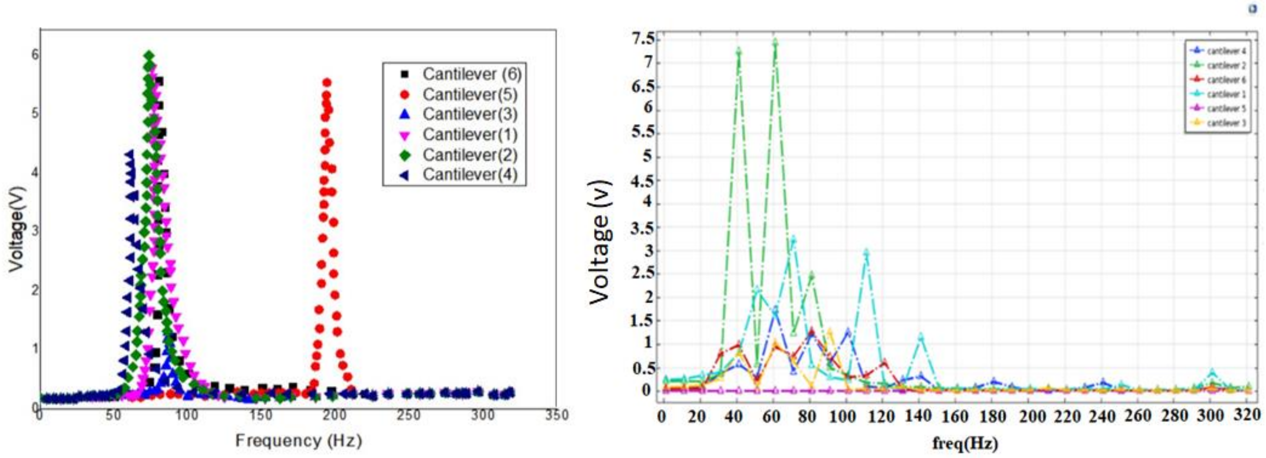

Figure 3. 30 The Graphical Representation of the Output voltage of the multi resonant piezoelectric energy harvester at their respective resonance frequencies (a) Experimental (b) FEA Simulation.

Table 3.6 :Comparison between the simulated and experimental results for natural Frequency

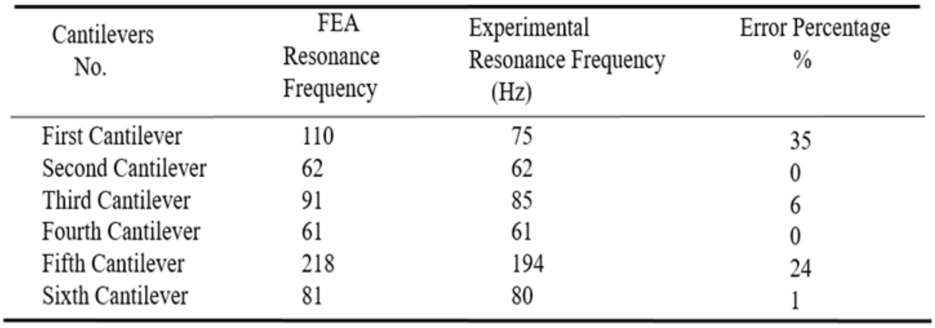

Cantilevers No.	FEA Resonance Frequency	Experimental Resonance Frequency (Hz)	Error Percentage %
First Cantilever	110	75	35
Second Cantilever	62	62	0
Third Cantilever	91	85	6
Fourth Cantilever	61	61	0
Fifth Cantilever	218	194	24
Sixth Cantilever	81	80	1

3.4 Conclusions

This Chapter introduces an initial design of a vibrational, thermal energy harvesting mechanism. The mechanism consists of PVDF, a shape memory alloy, and Lead-free material based on Lithium Niobate, single crystal piezoelectric material and enabling both piezo- and pyro-effect. A prototype was built and tested under different heat source frequencies for the thermal effect experiments in order to observe the pyro effect. Simultaneously, vibrational energy harvesting was also investigated based on the piezoelectric effect. A maximum peak output power of 1µ W was obtained at the optimal condition combining both the piezo and pyro results.

In this chapter, we discussed the individual piezoelectric and pyroelectric effects and how the two mechanisms work. Nevertheless, we also presented a broadband energy harvester designed to harvest vibrational energy. Further new implementation can be down in the proposed design. For example, proof mass use can be adapted in future work to lower done the resonance frequency. The designed broadband energy harvester was used to exploit the piezoelectric effect, but in future it can be used to exploit the pyroelectric effect as well.
The contribution of this research is to introduce the initial structure of thermal and vibrational energy harvesting mechanism for lead- free materials like Lithium Niobate.

4. Simultaneous hybrid energy harvesting through piezo and pyroelectric effects

The initial design of thermal and vibrational energy harvesting presented in the previous chapter was focused on studying the individual piezoelectric and pyroelectric effect of the cantilever beam. The purpose of this chapter is to study the coupling effect between the piezo- and pyroelectric effect and to verify the simultaneous functioning of the hybrid energy harvesting devices.

This chapter demonstrates how a cantilever beam based on lead-free material will exploit both the thermal and vibrational energy harvesting for studying this coupling effect. Small temperature variation at low frequency (below 1 Hz) is selected to harvest the maximum thermal energy when the cantilever works in low frequency.

On the other hand, to enhance the beam's piezoelectric effect-based energy harvesting, two magnets have been used. The beam alone will exhibit a resonance frequency that is much higher than the excitation frequency, hence the presence of the magnets placed at its tip will decrease the former and will match both. Then the coupling effect between the piezo- and pyro-electric, i.e. simultaneous functioning is investigated to improve output power. The chapter includes simulation based on the finite element COMSOL Multiphysics software. Then, experiment tests are investigated on the fabricated hybrid cantilever prototypes which demonstrated that output voltage up to 2V can be obtained at a maximum temperature varying frequency of 1Hz.

Beyond the above cantilever structure, we also develop in this chapter another concept of hybrid energy harvesting structure. The design still uses the piezoelectric effect and pyroelectric effect to harvest vibrational energy and thermal energy respectively. However, the system is capable of harvesting the energy with constant temperature, contrary to the previous cantilever and contrary to existing works. To this aim, we propose a closed system combined with the Joule-Thomson effect, which describes the temperature change of a real gas or liquid when forced through a valve or porous plug while keeping it insulated. Theoretical model is developed for the proposed system and simulation results are presented. Due to some fabrication challenges, its prototype fabrication could not be done, which can be treated as a perspective works.

4.1 Hybrid energy harvesting with a lead-free cantilevered structure

In this chapter, we propose a cantilever beam design for utilizing two energy conversion mechanisms simultaneously. Here, the pyroelectric and piezoelectric conversion are obtained with Lithium Niobate and shape memory alloy without any tip mass on a cantilever. As the cantilever has higher frequency than the excitation (vibration and temperature), the output power will be low. So, two neodymium circular disc magnets with a diameter of 4.5 mm and a thickness of 3 mm are used, as shown in Figure 4.1. One magnet is attached to the cantilever's free end which is a permanent magnet, and a soft magnet is attached to the mount located above the cantilever with opposite poles facing each other. Magnets are shown as an effective method of "plucking" a piezoelectric beam [110]. Therefore, a large deflection of the beam was expected by the magnetic attraction force, enhancing the piezoelectric effect.

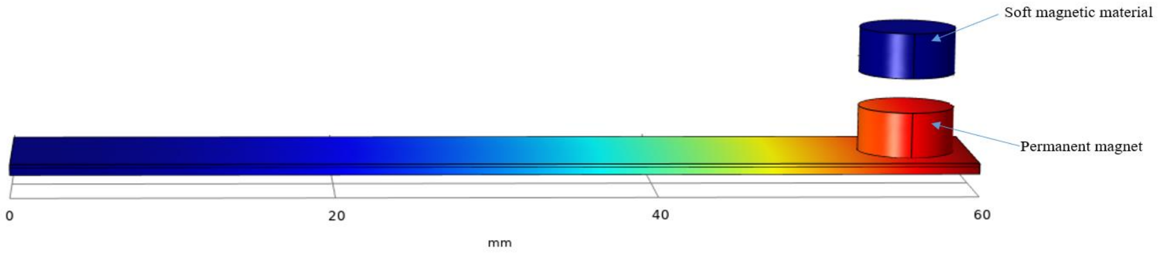

Figure 4. 1 Schematic of the structure.

In Figure 4.1 which shows the structure's schematic, the cantilever beam consists of two different material Lithium Niobate piezoelectric material and Shape member alloy. These two materials have a different coefficient of thermal expansion. The device behavior has been analyzed using a finite element multiphysics software. The effect of the materials properties and system parameters as well as effect of the frequency and magnitude of temperature cycling, on the efficiency of energy harvesting, are analyzed. The operating mechanism of the harvester is as follow. When the soft magnetic material temperature is below its magnetic Curie temperature, its magnetic properties the soft magnet drawn towards the permanent magnet, the free end of the beam get attached to the soft magnet developing a closed state depicted in Figure 4.2 a). Once the temperature starts to increase from the ambient temperature, the soft magnetic material is now heated up by conduction, and it loses its magnetic properties above its Curie temperature. When the soft magnetic material's temperature reaches its Curie temperature, the magnetic attraction force decreases. The cantilever beam’s mechanical force becomes dominant, which pulls it away from the soft magnetic material, this state is the open state depicted in Figure 4.2 (b). Again, when the temperature goes down to the ambient temperature the soft magnetic material regains its magnetization properties and then again, the permanent magnet gets attracted towards the soft magnetic material developing a closed state again.

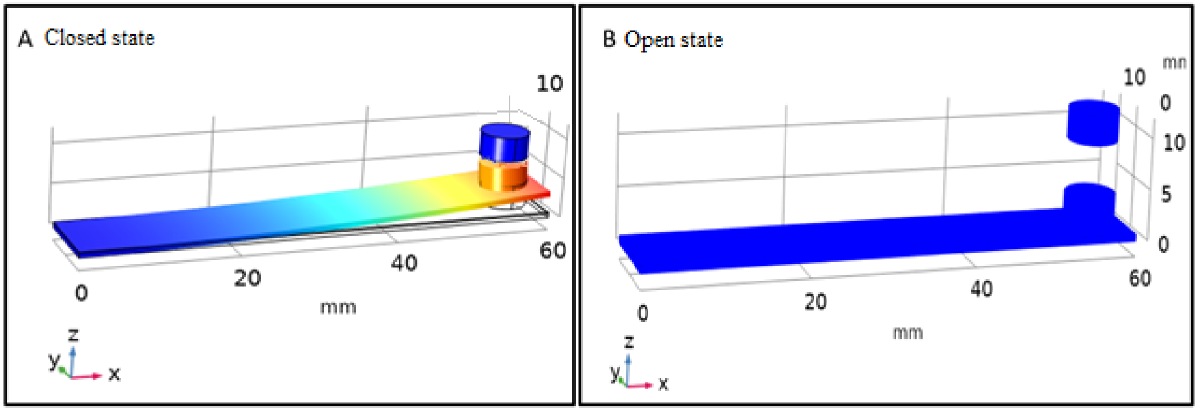

Figure 4. 2 The schematic of the (a) closed state and (b) open state.

4.1.1 Analytical Modelling

To keep the modelling simple and easy to understand, we started with a simple beam based on Timoshenko's analysis [111].Assuming that the thickness of the two layers are equal and the Young's modulus of the two layers are also the same, the curvature of the deflected beam is given by Equation (4.1). Later, the modelling was done using the same concept used by Miwon. K et.al on piezo-pyro hybrid energy harvesting device [112], also here for simplicity we conducted the study only for the piezoelectric and pyroelectric effect, therefore the magnetic force modelling is not conducted.

$$\frac{1}{R_s} = \frac{3}{2}\frac{\Delta\alpha.\Delta T}{h_b} \tag{4.1}$$

R_s is the radius of the beam's curvature, $\Delta\alpha$ is the coefficient of thermal expansion (CTE) difference between the two layers, ΔT is the temperature difference, and h_b is the thickness of the shape memory alloy beam.

The total electric charge on the Lithium Niobate layer is denoted as Q_t due to the beam's vibration as well as temperature variation. It can be considered as two current sources due to piezo- and pyro-electric effects. The total charge is the sum of the two effects and can be written as:

$$Q_t = Q_{piezo} + Q_{pyro} \tag{4.2}$$

Let us first consider the energy harvesting from surrounding vibration that uses the piezoelectric effect. The electric charge generated by the piezoelectric effect is depicted in Equation (4.3):

$$Q_{piezo} = \frac{(Fd_{31}L_P)}{h_P} \tag{4.3}$$

Where d_{31} is the piezoelectric coefficient, Lp is the length, F is the static force, and hp is the piezo layer's thickness. The strain of the piezo layers can be calculated by Equation (4.4):

$$\varepsilon_p = \frac{h_b}{2R_s} = \frac{3}{4}\Delta\alpha\Delta T \tag{4.4}$$

By substituting the force $F = \varepsilon_p E_p h_p b_p$ in above Equation (4.3), E_P is Young's modulus of the Piezo layer, b_p is the Lithium Niobate layer's width and h_b is the thickness of the shape memory alloy.

$$Q_{piezo} = \frac{h_p^2 b_p \mathrm{d31\ Lp}}{2\mathrm{Rs}} \tag{4.5}$$

The piezoelectric current can be calculated by Equation (4.6):

$$I_{piezo} = \alpha_{piezo} u - CV_{piezo} \tag{4.6}$$

I_{Piezo} is piezo output piezoelectric current, V_{piezo} is piezoelectric voltage, u displacement of the beam, and α_{piezo} is piezoelectric force factor C clamped capacitance of the beam.

The displacement of the piezo layer can be calculated by Equation (4.7):

$$u = u_M \sin(\omega_{Piezo} t) \tag{4.7}$$

Where u_M the displacement magnitude of the cantilever beam, ω_{piezo} is the angular frequency, and t is the time.

Energy for each piezo extraction by Lithium Niobate layer can be calculated with Equation (4.8):

$$E_{piezo} = \frac{1}{2}CV^2 \tag{4.8}$$

The power for piezoelectric effect can be represented by Equation (4.9):

$$P_{piezo} = f_{piezo} E_{piezo} \tag{4.9}$$

$$f_{piezo} = \frac{\omega_{piezo}}{2\pi}$$

Where f_{piezo} is the piezoelectric operating frequency and E_{piezo} is the piezoelectric beam's total energy, so the piezoelectric beam total power can be calculated by Equation (4.10):

$$P_{piezo} = f_{piezo} \frac{\alpha_{piezo}^2 U_M^2}{2C} \tag{4.10}$$

Now, if we focus on the pyroelectric effect. The electric charge Q_{pyro} is given by Equation (4.11):

$$Q_{Pyro} = p\, A\Delta T \tag{4.11}$$

Where p is the pyroelectric coefficient, and A is the surface area of the pyro material, so that:

$$Q_{Pyro} = p b_p L_p \Delta T \tag{4.12}$$

The pyroelectric current can be calculated by Equation (4.13):

$$I_{pyro} = \alpha_{pyro} T - CV_{pyro} \tag{4.13}$$

Where I_{pyro} is the pyroelectric output current, V_{pyro} is the pyroelectric voltage, T is the temperature, α_{pyro} is the pyroelectric force factor, and C is clamped capacitance.

The displacement of the pyro layer can be calculated by Equation (4.14) depending on the system's temperature change.

$$T = T_M \cos\left(\omega_{Pyro} p\right) \tag{4.14}$$

Where T_M is the Temperature variation magnitude, ω_{pyro} is the angular frequency, and t is the time.

Energy for each pyro extraction can be calculated below Equation (4.15).

$$E_{pyro} = \frac{1}{2} C V^2 \tag{4.15}$$

The power from pyroelectric effect can be represented by Equation (4.16)

$$P_{pyro} = f_{pyro} E_{pyro} \tag{4.16}$$

Where f_{pyro} is the frequency of the temperature oscillation, and E_{pyro} is the pyroelectric beam's total energy. So, the harvester Pyroelectric power can be calculated by Equation (4.17)

$$P_{pyro} = f_{pyro} \frac{\alpha_{pyro}^2 [\sin\beta] T_M^2}{C} \tag{4.17}$$

Where β is the conduction angle of the beam at the tip.

Let us now study the energy harvesting from both temperature and vibration excitations. Calculation of the total voltage excitation of the two different sources of energy simultaneously gives:

$$V_{total} = V_{piezo} + V_{pyro} \tag{4.18}$$

Where V_{total} is the total voltage from both the sources, V_{piezo} is the piezoelectric voltage, and V_{pyro} is the pyroelectric voltage.

The piezoelectric output voltage can be calculated from Equation (4.19):

$$V_{piezo} = \frac{\alpha_{piezo^2 U^2 M}}{C} \tag{4.19}$$

The pyroelectric output voltage can be calculated from Equation (4.20):

$$V_{pyro} = \frac{\alpha_{pyro}^2 [\sin\beta] T_M^2}{C} \tag{4.20}$$

Therefore, the total output voltage can be written as follow:

$$V_{total=} \frac{\alpha_{piezo}^2 U_M^2}{2C} + \frac{\alpha_{pyro}^2 [\sin\beta] T_M^2}{C} \tag{4.21}$$

The total power from the two sources is depicted in Equation. (4.22),

$$P_{total} = P_{piezo} + P_{pyro} \tag{4.22}$$

Therefore, the total output voltage can be written as follow:

$$P_{total} = f_{piezo}\frac{\alpha_{piezo}^2 U_M^2}{2C} + f_{pyro}\frac{\alpha_{pyro}^2[\sin\beta]T_M^2}{C} \tag{4.23}$$

Figure 4.3 shows an equivalent circuit of the two sources-based energy harvesting. In this, the voltage, which is applied to a resistive load, is assumed to be sum of the piezoelectric and pyroelectric voltages at different frequencies.

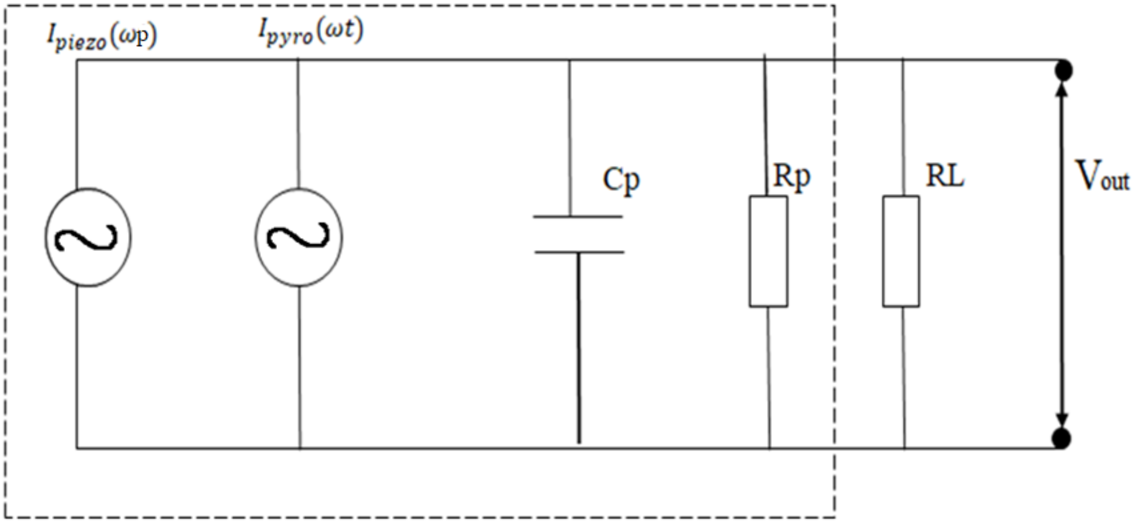

Figure 4. 3 The equivalent circuit of the design.

4.1.2 Finite Element Analysis

Extensive modelling was done using the finite element method to study the mechanical and heat transfer behavior of the cantilever beam placed in proximity of a heat source. This particular study was performed using finite element analysis (FEA) techniques in a Multiphysics COMSOL modelling package. We have used solid mechanics, heat transfer physics, and electrostatics selected from the standard set of COMSOL Multiphysics modules for achieving the specific goal for this study. A 2D model was used over a 3D one. Indeed, a 2D model reasonably lowers the number of degrees of freedom, which can quickly be solved with minimum mesh sizes that can accurately reflect our structures' most minor characteristic features.

One of the most crucial points was the meshing around the contact point between the cantilever and the heat source, which is particularly important and shown in Figure 4.4. On the other hand, for this model, we have used two magnets one is permanent, and the other one is a soft magnet of the exact dimensions with opposite poles. Solving the solid mechanics model with heat transfer contact pair was used by defining the identity pair with heat continuity boundary conditions. The cantilevered was composed of two different material Lithium Niobate with a thickness of 0.180 mm and shape memory alloy with a thickness of 0.110 mm. Both materials have a different coefficient of thermal expansion. The length of the cantilever was 60 mm, and the cantilever width was 10 mm. The magnetic material neodymium (NdFeB) circular disc magnets with a diameter of 4 mm and a height of 2.5 mm were used, and a Soft magnetic alloy (FeNi).

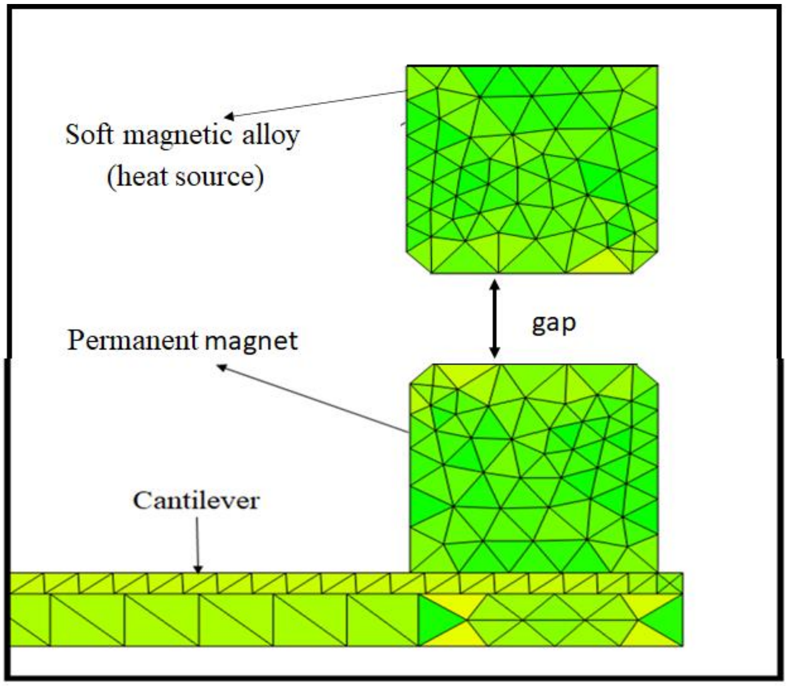

Figure 4. 4 Model geometry, mesh and mesh quality in the vicinity of the thermal contact between the cantilever (bottom) and magnet as the heat source (top).

To model the thermal response of the system, we did a transient thermal simulation. The heat transfer occurs when heating the whole system. The soft magnetic material in direct contact with the heat source gets heated first and transfer heat with the hard magnets when the magnets are in close contact. The two scenarios in this simulation are depicted in Figure 4.2, representing the closed and open state discussed in the coming section.

In the simulation's initial condition, when the system is in the closed state, heat is applied to the soft magnetic material by the heat source on the material's top surface.

Two case studies were conducted on the structure's temperature response, the first one was the closed state, and the second one was the open state. In the closed state, considering a thermal contact between the permanent magnet and the soft magnetic material and the open state, there is no thermal connection between the permanent magnet and the soft magnetic material in the open state. At the initial condition, the temperature was 295K which was the ambient temperature and then heat load is applied. This heat load is used for a specific time, and after that it was removed.

The heat transfer between the soft and permanent magnet occurs when the system is in a closed state, which means the system is working at the ambient temperature. Soft magnetic material has magnetic properties. Once the soft magnetic materials heat up, it loses its magnetization properties and detached from the permanent magnet and this state is referred to as the open state.

In the simulation to study the closed contact state, the modelling is based on the contact node model, where the contact points between the two magnets were defined. And later used in coupled modelling based on solid mechanics and heat transfer in solids. When the system was in the closed state by this contact node model, the heat transfer between the two magnets was studied, and the same model was used for the time-dependent study. We defined the mechanical contact between the soft magnetic material and the permanent magnet in the contact node. We solved the Equation in all domains in the Heat transfer in the solid module for the heat transfer solution and defined the heat source's temperature. Finally, the most important node was the cooper- Mikic-Yovanovich-Correlation which also defines the surface roughness. After that, we coupled the solid mechanics' solutions into the solid's heat transfer solutions to have a bidirectional coupling in the contact pressure node. Figure 4.5 depicts the whole FEA model's schematic defining the fixed constraints and the heat and cold sources with their respective temperature.

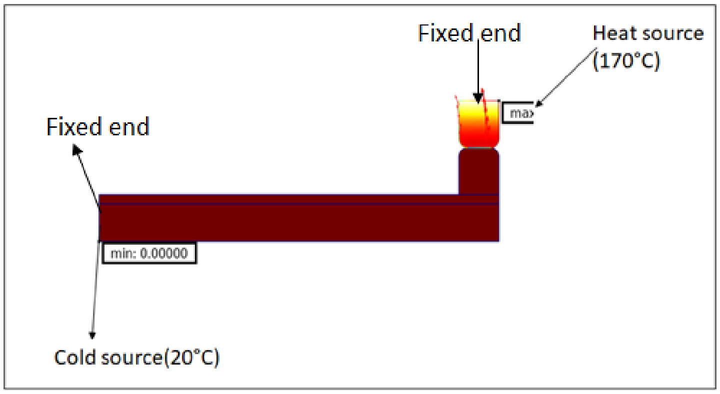

Figure 4. 5 *schematic of the FEA model.*

Figure 4.6 shows the time-dependent simulation along the beam length. The heat source is designed to heat and cool the entire structure periodically. The beam's temperature is simulated as the heat source's temperature fluctuates from 20 °C to 170 °C at 0.01 Hz for 5 seconds. Figure 4.6 shows temperature overtime at the heat source and the beam. (a)The beam's tip displacement with a temperature change is shown (b) Change in beam's temperature is depicted. This simulation was conducted for 5 seconds, and the beam's temperature did not reach a steady-state. Moreover, it was a time-consuming simulation that's why we chose to do it for a shorter period, as the simulation study took almost 9 hours. But by designing a time-dependent study of 5 seconds, the temperature variation experimented by the beam is shown in Figure 4.6 (b).

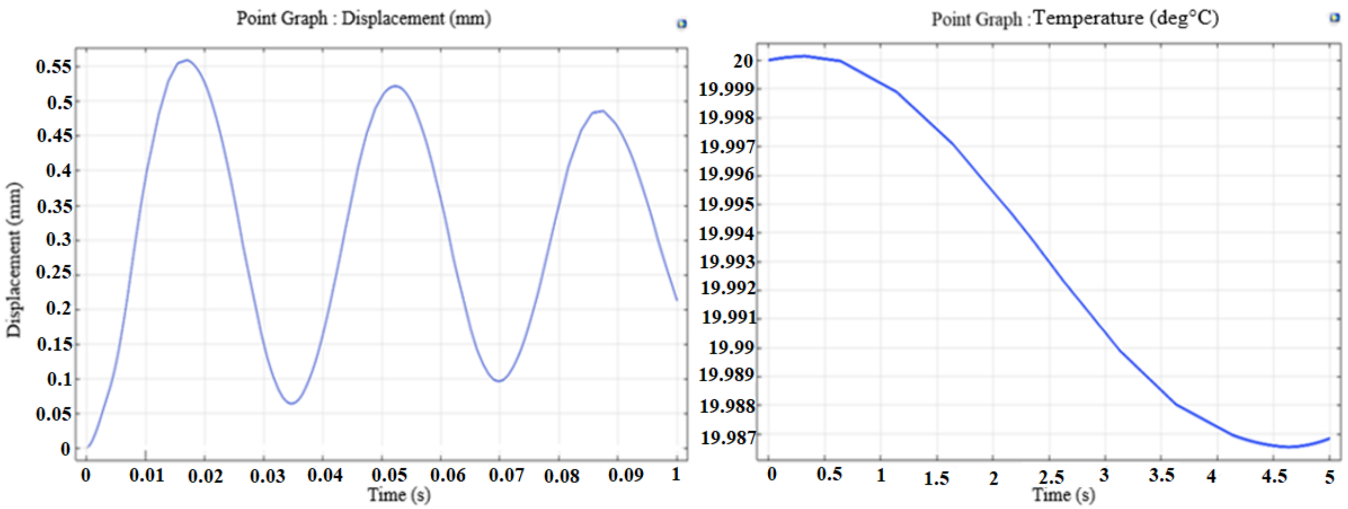

Figure 4.6 Simulation of time-dependent study. (a) The beam's tip bending with a temperature change is shown (b) Change in beam's temperature.

4.1.3 Experimental Set-up

The Shape memory alloy is composed of Ti-Ni-Cu, with a total thickness of 0.110 mm. The lithium niobate total thickness was 0.180 mm. The dimensions of the other components are depicted in Table 4.1.

Table 4.1 : Dimensions of components

Item	Dimension [mm]
Shape memory alloy	10 × 60 × 0.11
Lithium Niobate	10 × 60 × 0.18
Heat Source	70 × 70 × 10

A hairdryer was used with a fixed duty cycle to obtain a cyclic heating system, which created a periodic temperature profile to generate temperature fluctuations as excitation applied to the cantilever for the pyroelectric effect as harvesting. Figure 4.7 shows the experimental setup for generating the cyclic heat energy consisting of a heat source and a thermocouple. A K-type thermocouple sensor was used and attached to the beam's top electrode at its centre to ensure good thermal contact. The distance between the heat source and the cantilever beam was about 100 mm. To measure the displacement of the cantilever beam laser sensor has been used (Keyence LV-H62). An oscilloscope was used to acquire and display the output voltage.

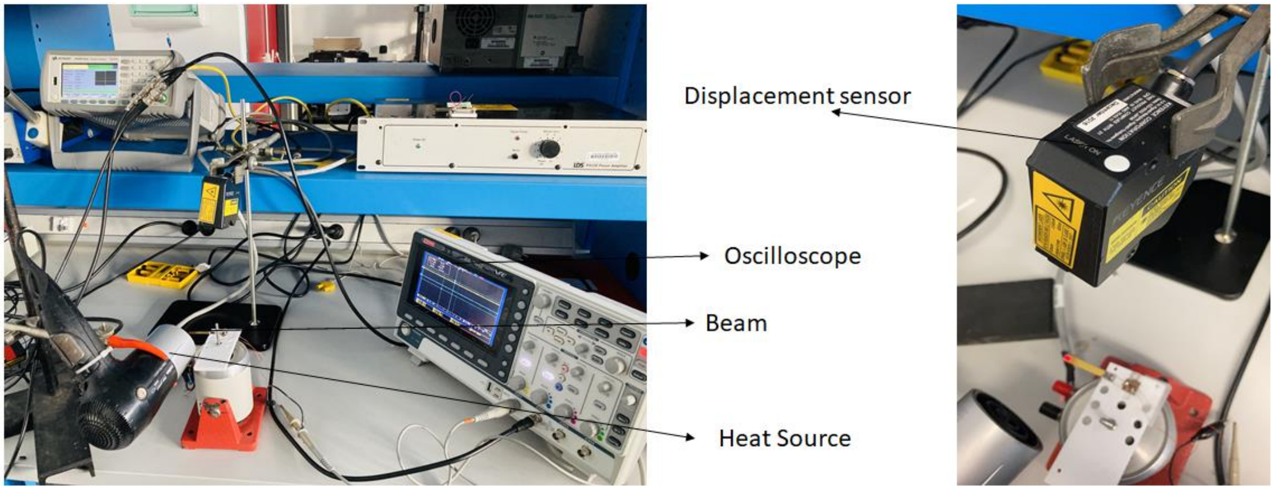

Figure 4. 7 Experimental Set-up.

The cyclic heating system was desirable to achieve a periodic temperature profile for generating temperature fluctuations in the pyroelectric material. To this aim a time varying work cycle was designed for the heat sources and depicted in Figure 4.8. This heating-cooling cycle was designed with a duty cycle of 50%.

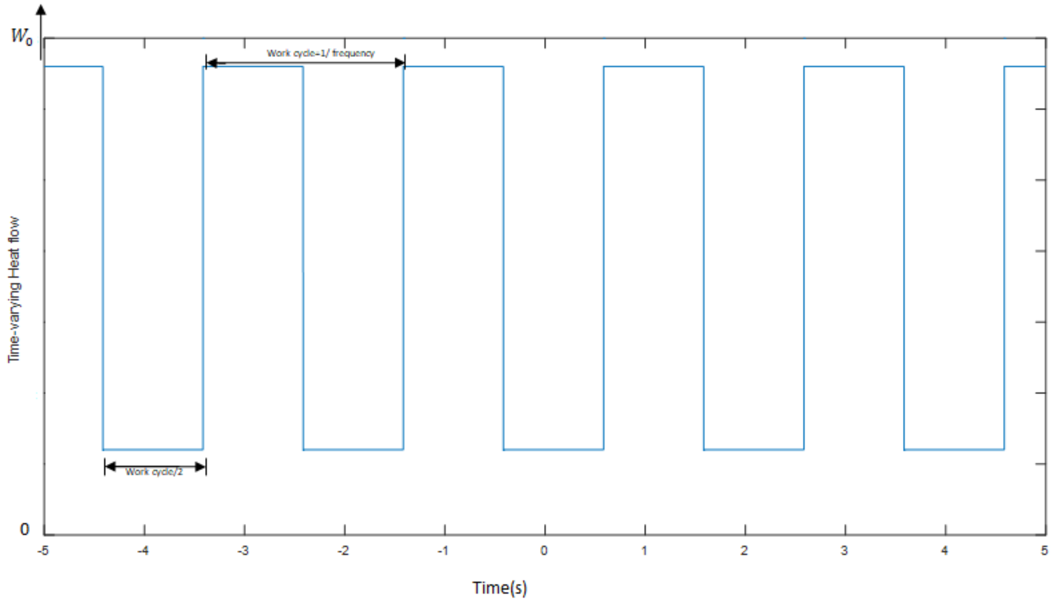

Figure 4. 8 The time-varying heat flow work cycle is designed for the heat source.

4.1.3.1 Experimental Results

Figure. 4.9 shows a typical graph of recorded temperature variations of the heat source and the corresponding output voltage from the measurement. The temperature of the cantilever beam reached a maximum of 45°C and the output voltage reached a maximum of 2V_{p-p}, respectively. From the graphs it is observed that as the temperature of the cantilever beams rises from the ambient temperature, the voltage produced by the material increases in the positive direction and when the heating sources temperature goes down it responds by decreasing to reach negative maximum. It is to be noted that the fluctuations of the temperature affect the durations of heating and cooling phases of the thermal cycle. It's worth mentioning that we experimented on three different frequencies 0.04 Hz, 0.5 Hz, and 1Hz. And we noticed that at 0.04 Hz, we got the maximum output as 2$V_{p-p,}$ as shown in Figure 4.9.

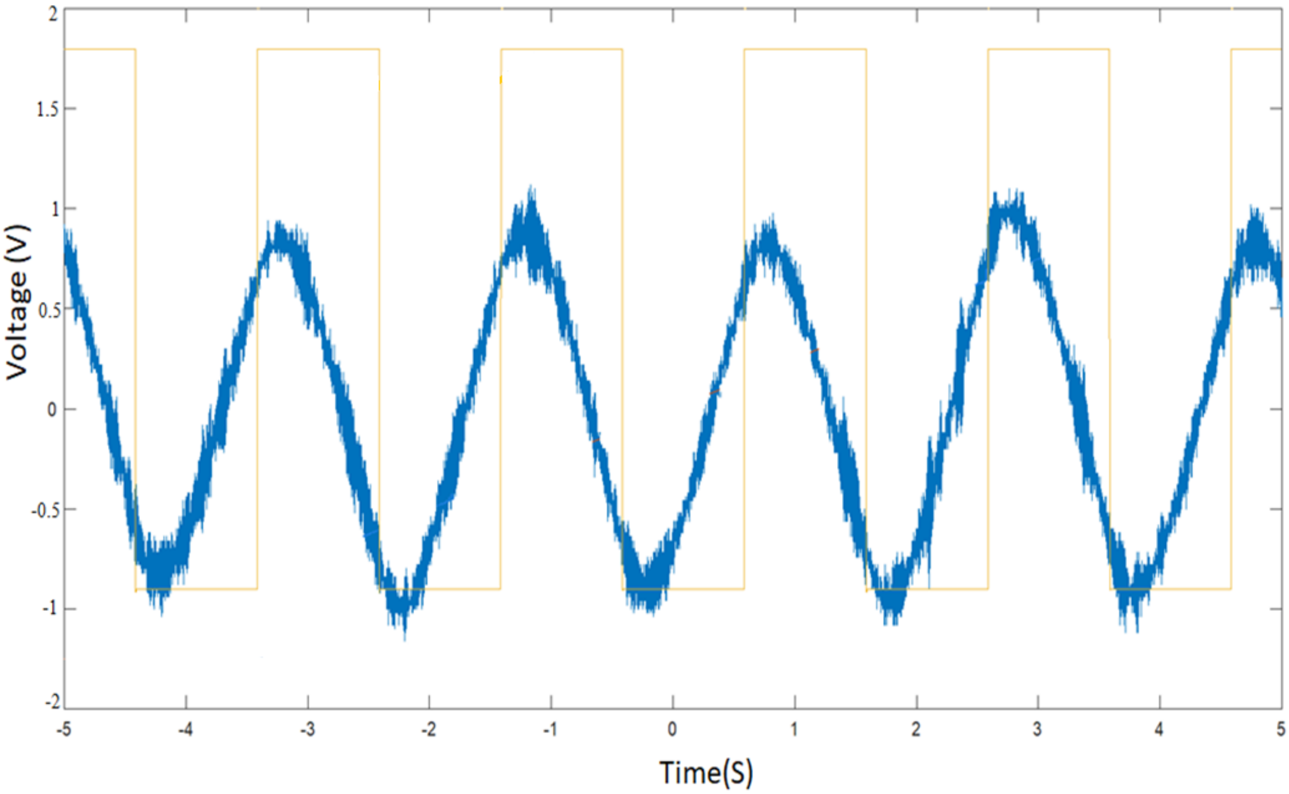

Figure 4. 9 shows the output voltage of the beam when excited with temperature variation at 0.04 Hz.

We also measured the beam's displacement, obtained with the 0.04 Hz temperature fluctuation. The results are in Figure 4.10 where (a) shows the displacement of the beam and (b) the heat source temperature. It was noticed that the maximum deflection of the beam at 0.04 Hz frequency was 19µm, which was the maximum among all the other frequencies.

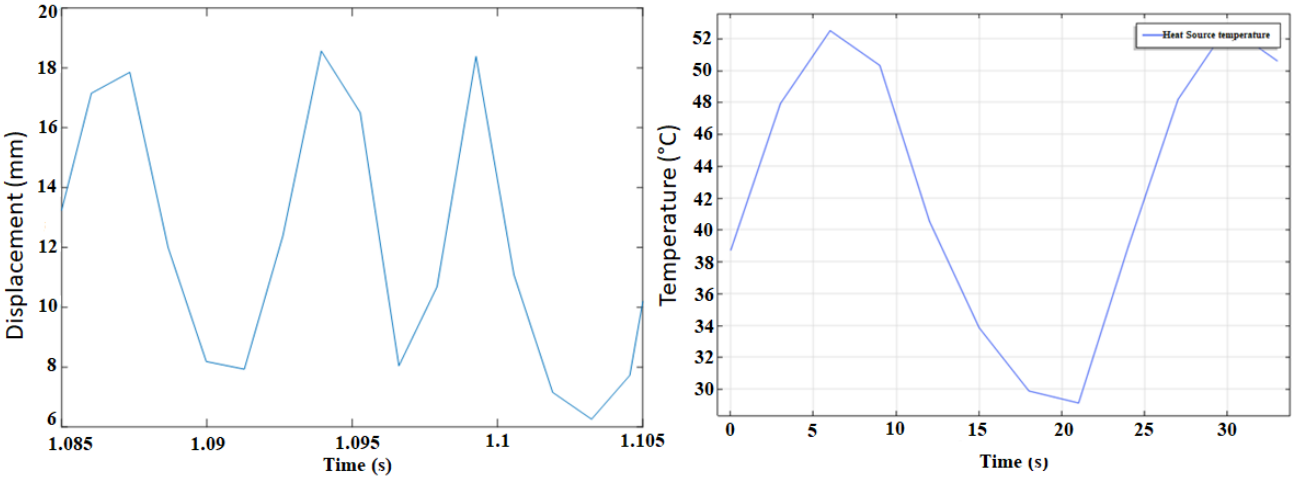

Figure 4.10 (a) Beam's bending at 0.04 Hz (b) change in the heat source temperature.

From the experimental results, we conclude that the output voltage is slightly increased as the frequency decreases. The reason is that more energy is obtained from heat source thanks to the more extended long period. As a consequence, we observed that we could get maximum output from the thermal excitation at low frequency of bending of the cantilever. Still, at the same time, the output from the piezoelectric effect was significantly less at low-frequency range since the ideal condition for obtaining the maximum output in the vibration energy is to work at its resonance frequency. The role of the additional magnet that will be put at the tip of the cantilever is therefore to reduce the resonant frequency of the latter and improve the harvested energy from vibration. Two neodymium circular disc magnets with a diameter of 4 mm and a thickness of 2.5 mm are used for that, as shown in Figure 4.11. One magnet is attached to the cantilever's free end, and the other one is attached to the mount located above the cantilever with unlike poles facing each other. Magnets working is based on the "plucking" method. As a consequence, we noticed a large deflection of the beam due to the magnetic attraction force during the experiment.

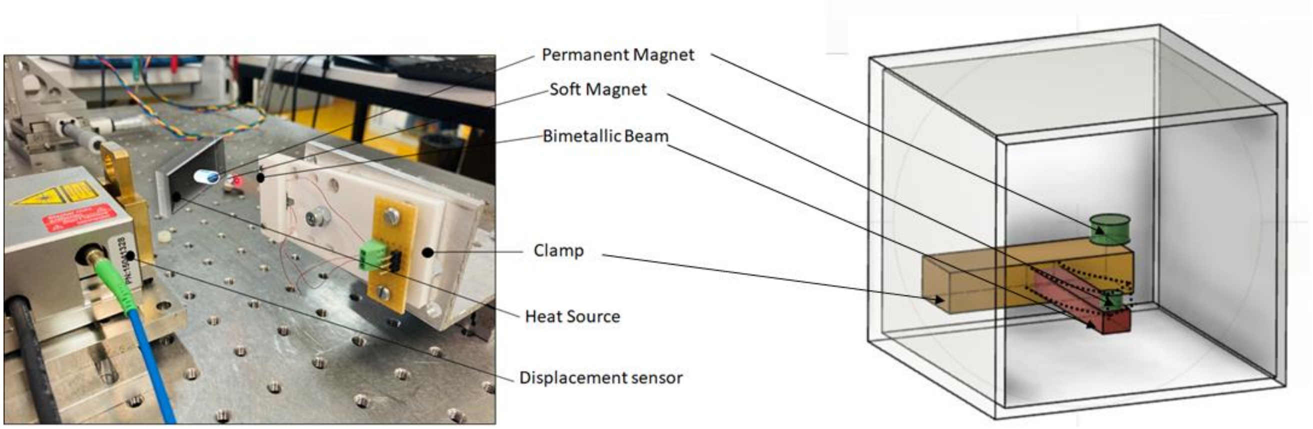

Figure 4.11 Experimental setup with the two magnets along with the schematic principle.

Figure 4.12 shows the open circuit voltage measured as 5Vp-p with the force of attraction of two magnets, and where the bending of the beam was 30µm. It was observed that whenever the two magnets are attached or released, they produce sharp peaks. Whenever the permanent magnet comes in close contact with the soft magnetic material heat transfer takes place and the cantilever beam bends producing a negative peak.

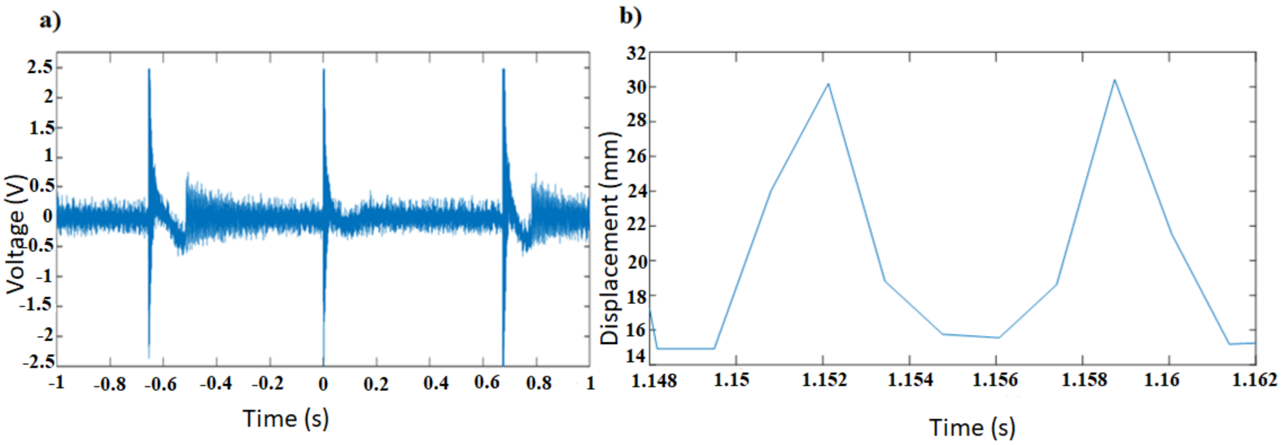

Figure 4. 12 (a) The output voltage (b) bending of the cantilever beam.

It is important to note that, as the temperature of the soft magnet increases, it loses its magnetic properties resulting in a less attraction between the two magnets and afterwards in their separation. When the mechanical force becomes more prominent than the magnetic force, the beam gets released, producing a negative peak. As expected, the piezoelectric effect contributes better, or even more dominant over the pyroelectric effect, in the output voltage with the large deflection caused by the magnets.

We also measured the open-circuit voltage without magnets. Here, the results in Figure.4.13 shows experiment results: open-circuit voltage. The positive peak in the voltage shows that the beam heats up ($dT/dt > 0$). The negative peak areas show that the beam is cooled down. In Figure.4.14 (a) without magnets, the maximum power output of 16 nW is obtained at an optimal condition when the Load resistance is 18 M Ω.

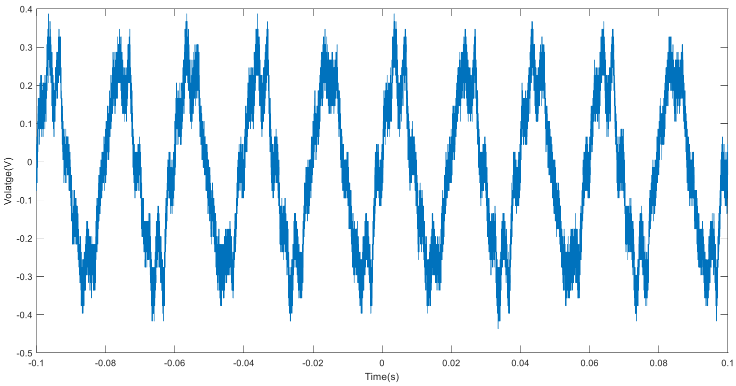

Figure 4. 13 Open- circuit voltage without magnets.

With the force of attraction of two magnets, the maximum power output of 290 nW is obtained at an optimal condition when the load resistance is 2.5M Ω, as shown in Figure 4.14 (b). The average output power is lower than the peak output power shown in Figure 4.14. In particular, the average power in experiments with magnets whose output voltage appears in the form of a spike is much lower than the peak power.

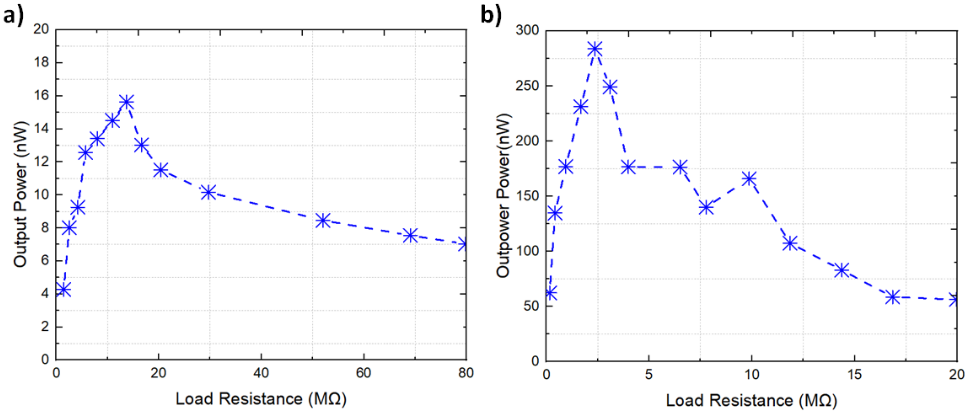

Figure 4.14 Measured peak power output versus load resistance (a) without magnets (b) with magnets.

4.1.4 Remark

It's worth mentioning that the above analytical modelling is also applicable for the Six- cantilever multi resonant energy harvester, which we depicted in the previous chapter. In this case, the total output power for the multi resonant energy harvester will be the sum of powers from the six cantilevers, each of them being modelled with the approach presented in this section.

4.2 A hybrid piezo-pyro E.H. for constant temperature

Within the ENHANCE European project, hybrid energy harvesters have to be designed and developed to supply small and autonomous sensors in automobiles. This work's focus is significantly related to the harvesting of energy from vehicles' vibration and the high temperature (in fluctuation or not) around the engine. To this aim, an ideal hybrid piezo-pyroelectric energy harvester should harvest vibrational energy at lower frequency ranges (less than 500 Hz) through piezoelectric effect and thermal energy at a higher temperature range through pyroelectric effect. However, the pyroelectric effect work with a time-varying temperature. As pyroelectric materials' necessary behavior responds to heat flow, charge generation upon temperature change is followed by gradual charge disappearance if the temperature stays constant. Due to this reason, to harvest thermal energy based on the pyroelectric effect, we always need a time-domain varying temperature.

The new hybrid energy harvester proposed from this section has been designed using Lithium Niobate piezoelectric material, shape memory alloy, polyvinyl difluoride, piezoelectric polymer, and helium gas, and its performance has been investigated using COMSOL Multiphysics® finite element method (FEM) software for rapid validation of the Proof of concept and visualization of the transducer functioning. The proposed hybrid harvester can convert both vibrational mechanical energy and constant temperature energy into electrical energy. The constant temperature conversion principle is based on the Joule-Thomson physical principle. Different transducer design and material configurations have been evaluated to identify the hybrid transducer's optimum conditions, materials, and innovation. For the FEM analysis, Solid mechanics, electrostatics for piezoelectricity, heat transfer in solids, heat transfer in fluids, electric currents chemistry modules have been used for pyroelectricity and associated thermodynamic properties in global definitions as well as for the vibrational piezoelectricity. The simulation demonstrates that the hybrid harvester could generate energy at a constant temperature, as predicted. The harvester has a volume of 12.21 cm^3 and can work at a constant temperature between 20 and 220 °C, and with surrounding mechanical vibration up to 500 Hz of frequency. On the one hand, the harvester was able to work for up to 8 hours under constant temperature. Simultaneously we also calculated stored energy, which was 0.9 J at 561 Hz of mechanical vibrational excitation. This lead-free piezo-pyro energy harvester is a promising device that can be used for environmental purposes, especially in automobiles. Its high-temperature performance stability, energy harvesting at constant external temperature, piezoelectric energy harvesting at lower frequencies, and lead-free nature makes it ideal to be used as an energy harvester and supplier for small appliances.

4.2.1 Working Principle

While vibrational energy harvesting through piezoelectric materials raised numerous works in the literature, harvesting thermal energy poses tremendous challenges when the ambient temperature is constant or varies slowly. In this case, we explore the combination of gas expansion and the above effects, with a harvester structure composed of the piezoelectric transducers themselves placed in closed structure with an ideal gas. The design's working principle is similar to a heat engine based on the Carnot cycle. It consists of two isothermal processes (expansion and contraction) and two adiabatic processes (expansion and contraction). The gas enclosed behavior is based on the Joule-Thomson effect to transform constant external temperature into temperature fluctuation.

The piezo-pyro hybrid transducer will have a preferred placement near the automobile components where vibrational and thermal losses are maximum. The identification of these spots is near the engine and around the car exhaust system.

Figure 4.15 illustrates the proposed concept. It is assumed that the proposed closed system will be vibrating at 1g of acceleration. Simultaneously, for the thermal gradient, the Joule-Thomson effect works ideally when the temperature of the gas inside the chamber changes over time through external temperature which is constant. The proposed structure consists of a hemisphere made up of copper and a circular ring. Six piezoelectric cantilevers are attached on the top and sealed with a PVDF film.

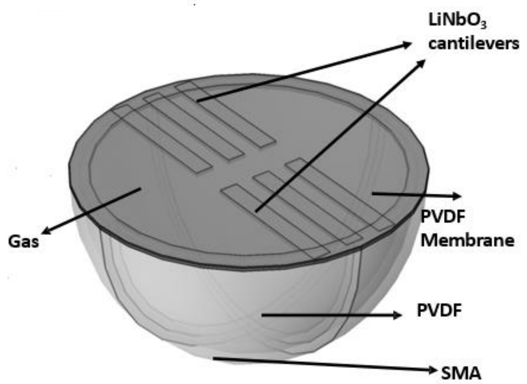

Figure 4. 15 Illustration of the proposed hybrid energy harvester structure.

4.2.2 Proof of concept

The proposed design of hybrid energy harvester is inspired from heat engine principle, in particular the Carnot engine.

So, to understand its functioning, let us see how the Carnot engine cycle works. Carnot engine's cycle consists of a linked sequence of a thermodynamic process that involves the transfer of heat and work in and out of the system while varying temperature, pressure, and other state variables within that system, eventually returning the latter to its initial state. During a closed cycle, the method returns to its original thermodynamic state in terms of temperature and pressure. For the proposed hybrid harvester, the thermodynamic cycle is converting mechanical work to increase the temperature and vice versa (decrease in temperature results into mechanical work). The system has two isotherms, which will help pyroelectric material harvest energy. The Carnot cycle based on the assumption of the absence of incidental wasteful processes such as friction, and the assumption of no conduction of heat between different parts of the engine at different temperatures.

The Carnot cycle consists of the following four processes depicted in Figure 4.16: along with that in Figure 4.17 the actual Woking cycle of the transducer is depicted.

1. A reversible isothermal gas expansion process. In this process, the ideal gas in the system absorbs q_{in} amount heat from a heat source at a high temperature T_{high}, expands and does work on surroundings.
2. A reversible adiabatic gas expansion process. In this process, the system is thermally insulated. The gas continues to expand and do work on surroundings, which causes the system to cool to a lower temperature, T_{low}.
3. A reversible isothermal gas compression process. In this process, surroundings do work to the gas at T_{low}, and causes a loss of heat, q_{out}.
4. A reversible adiabatic gas compression process. In this process, the system is thermally insulated. Surroundings continue to do work to the gas, which causes the temperature to rise back to T_{high}.

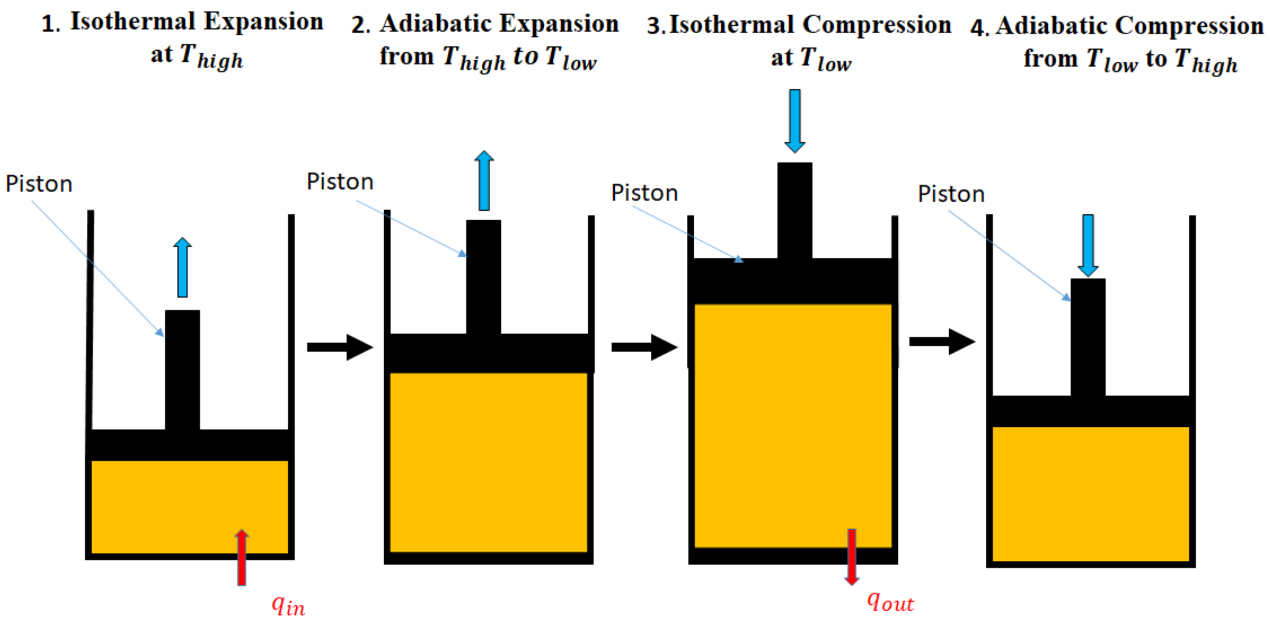

Figure 4. 16 An ideal gas-piston model of the Carnot cycle.

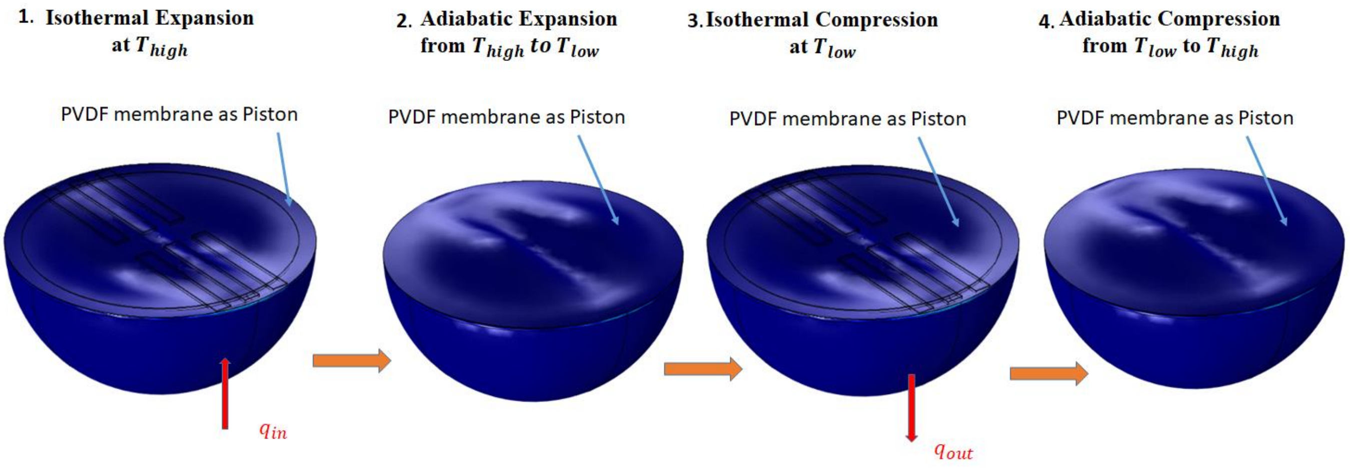

Figure 4. 17 The Transducer working cycle based on Carnot Principle.

4.2.2.1 Work done:

Work done by the engine is shown by the area enclosed under the curve depicted in Figure 4.18, Figure 4.18 represents a P-V graph as well as a T-S graph allowing to understand the thermodynamic cycle involved in our system as well as helps in understanding the work done by the system and on the system. The thermodynamic cycle is divided into four processes, process 1-2, process 2-3, process 3-4, and process 4-1. In a realistic scenario, processes 1-2 and process 2-3 will look like a single process. The same for process 3-4 and 4-1. For derivation of the equations, we have to split these cases into isothermal and isentropic cases. Where the reversible process follows both the first law and the second law of thermodynamics. The steepness in the graph going from the isothermal and isentropic process can be observed because of $P.V \neq (P.V)^{\gamma}$.

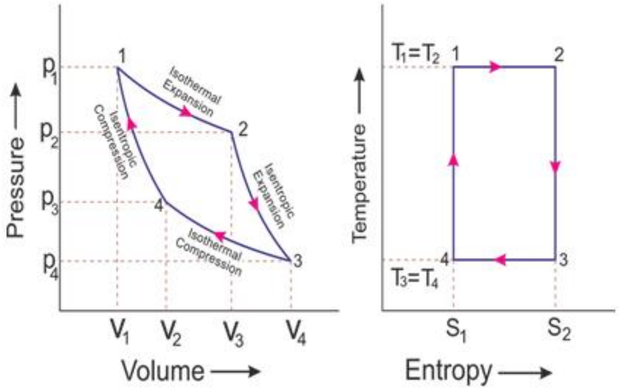

Figure 4. 18 Sketch of P-V and T-S diagram representing various combinations of processes forming cyclic integrals.

4.2.2.1.1 First Stage (Isothermal Expansion)

In the reversible isothermal expansion (1) shown in Figure 4.16, representing how the gas expands slowly, performing work on the surroundings. A system with ideal gas absorbs an amount of heat q_{in} from the heat source, which is at a temperature T_{high}, expands, and performs work on surroundings. During this process, due to the piston's movement, the heat Q_1 is given to the gas; therefore, the latter starts expanding isothermally. The temperature T_1 remains constant until volume and pressure reaches v_2 and p_2. The heat supplied by the heat source body is fully absorbed by the gas and is utilized by doing external work. So, the heat provided during this process is equal to the work done during this process. This isothermal expansion is represented by the curve 1-2 on the P-V and T-S diagram.

So, the work done by the gas is:

$$W = p_1 v_1 \log_e \frac{v_2}{v_1} \tag{4.26}$$

$$W = mRT_1 \log_e \frac{v_2}{v_1} \tag{4.27}$$

As there is no change of temperature from point 1 to 2, so ($T_1=T_2$) and as per the first law of thermodynamics, the internal energy is also zero (E=0), here m is the the amount of substance of gas (also known as number of moles.

Then the heat supplied is:

$$W_{1-2} = Q_{1-2} = mRT_1 \log_e \frac{v_2}{v_1} \tag{4.28}$$

$$W_{1-2} = Q_{1-2} = mRT_1 \log_e r \qquad (4.29)$$

$$r = \text{Expansion ratio} = \frac{v_1}{v_2}$$

On the other hand, the entropy change is:

$$(S_1 - S_2) = \frac{Q_1}{T_1} \qquad (4.30)$$

$$Q_{1-2} = (S_2 - S_1)T_1 \qquad (4.31)$$

4.2.2.1.2 Second Stage (Isentropic Expansion)

In reversible isentropic expansion (2) shown in Figure 4.16, the system is assumed to be thermally insulated, i.e., it neither gains nor loses heat. The gas continues to expand by reducing the pressure and do work on the surroundings, which causes the system to cool down at a lower temperature T_{low} and losing internal energy equal to the work done. As a result, the gas temperature reduces. Here $(P.V)^{\gamma}$ =constant.

Since the piston moves outward, the gas expands adiabatically till it reaches the pressure p_3, volume v_3, and temperature T_2. There is no exchange of the heat with the surrounding gasses (Q = 0). The reversible adiabatic expansion is represented by the curve 2-3 on the P-V diagram.

So, the work done by the gas is:

$$W_{2-3} = \frac{p_2 v_2 - p_3 v_3}{\gamma - 1} \qquad (4.32)$$

$$W_{2-3} = \frac{mRT_2 - mRT_3}{\gamma - 1} \qquad (4.33)$$

$$W_{2-3} = \frac{mR(T_1 - T_2)}{\gamma - 1} \qquad (4.34)$$

The change of internal energy can be expressed as E = - W, and while there is no entropy change means, $S_2 = S_3$.

4.2.2.2Work done during contraction of a gas:

More generally due to losses (friction, additional energy loses), no system is reversible without any external force, here Figure 4.19 depicts the two isothermals.

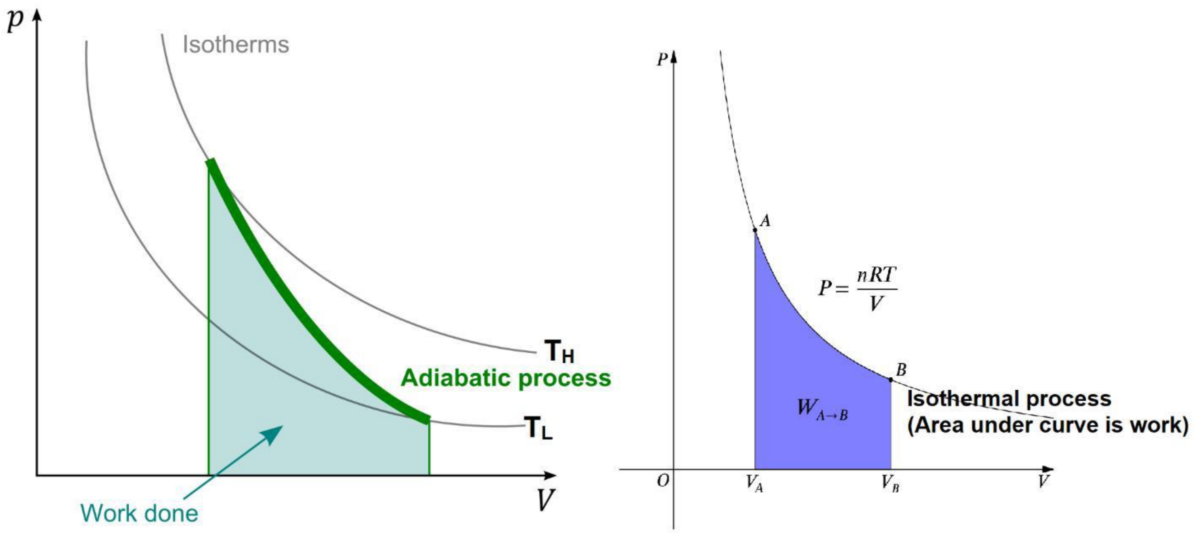

Figure 4. 19 Sketch of adiabatic and isothermal process, area under the curve is work done. The graph's steepness is due to (P.V.) γ is constant in the adiabatic process; compared to PV=constant in the isothermal process. The two isotherms occurred under the adiabatic process.

4.2.2.2.1 Third Stage (Isothermal Compression)

In reversible isothermal compression (3) depicted in Figure 4.16, the gas has transmitted some heat in the form of thermal loses T_{low} to the surroundings, and the piston starts moving inward compressing the gas. Now the surroundings work on the system, and heat is transferred from the system to the surroundings, such that temperature is constant, and heat q_{out} goes out of the system. The gas is compressed isothermally, therefore, the temperature T_3 will be constant from v_3 to v_4. Henceforth temperature T_4 is equal to T_3. Thus, heat is rejected to the cold source, similar to the gas's work. The isothermal compression curve is depicted by 3-4 on the p-v curve. So, the work done on the gas is:

$$Q_{3-4} = p_3 v_3 \log_e \frac{v_3}{v_4} \tag{4.35}$$

$$Q_{3-4} = mRT_3 \log_e \frac{v_3}{v_4} \tag{4.36}$$

$$Q_{3-4} = mRT_3 \log_e r \tag{4.37}$$

Here the total change of entropy,

$$S_3 - S_4 = \frac{Q_3}{Q_4} \tag{4.38}$$

$$Q_3 = T_4(S_3 - S_4) \tag{4.39}$$

$$Q_3 = T_4(S_2 - S_1) \tag{4.40}$$

4.2.2.2.2 Fourth Stage (Isentropic Compression)

In the reversible isentropic compression (4) shown in Figure 4.16, the system is assumed to be thermally insulated. The gas in the system is thermally insulated from the surroundings. However, surroundings continue to do work on the gas, which causes the temperature to increase. Internal energy equal to work done will increase because pressure has grown, and the volume gets lowered. When the piston moves inwards, the gas insides the closed system is compressed adiabatically until it reaches the pressure p_1, volume v_1, and temperature T_1. After that, the gas returns to its original condition to complete the Carnot cycle. The gas temperature increases from T_4 to T_1, and no heat is absorbed or rejected by the gas. Curve 4-1, represents the reversible adiabatic compression on the P-V and T-S diagram.
So, the work done on the gas is:

$$W_{4-1} = \frac{p_1 v_1 - p_4 v_4}{\gamma - 1} \tag{4.41}$$

$$W_{4-1} = \frac{mRT_1 - mRT_4}{\gamma - 1} \tag{4.42}$$

$$W_{4-1} = \frac{mR(T_1 - T_3)}{\gamma - 1} \tag{4.43}$$

Hence from the above cycles, the total internal energy decrease in reversible adiabatic expansion shown in curve 2-3 is equal to the increase in internal energy during reversible adiabatic compression 4-1.
So, the net work done can be calculated with Equation. (4.44).

$$W = \text{Heat supplied - Heat rejected} \tag{4.44}$$

$$W = mRT_1 \log r - mRT_3 \log r \tag{4.45}$$

$$W = mR \log r \, (T_1 - T_3)$$

The Carnot efficiency is defined by:

$$\eta = \frac{work\ done}{Heat\ supplied} \tag{4.46}$$

$$\eta = \frac{mR \log r (T_1 - T_3)}{mR \log r T_1} \tag{4.47}$$

$$\eta = \frac{(T_1 - T_3)}{T_1} \tag{4.48}$$

$$\eta = 1 - \frac{T_3}{T_1} \tag{4.49}$$

We can conclude from the Carnot cycle efficiency equation (4.48) that T_1 is more significant than T_3. Therefore, for smaller value of T_3, the thermal efficiency will be maximized. That is why the Carnot cycle has the highest thermal efficiency of all heat engines.

4.2.3 Thermodynamics for Transducer

Reconsider the piezo-pyro system in Figure 4.15. The hemispherical part comprises PVDF to harvest pyroelectric energy, SMA to provide mechanical strength and at the same time increase up to 2 % strain when coupled with PVDF in the system [113]. The top of the hemisphere has several piezoelectric cantilevers embedded on the circumference and is closed by a PVDF membrane arrangement. The PVDF membrane has pyroelectric and elastic properties.

The present piezo-pyro transducer utilizes the vibrational and thermal losses present in the automobiles. The working principle is based on Carnot cycle as depicted in the last section the transducer (closed system) also consist a cyclic process in which, due to the external vibration, pressure will be applied to the ideal gas by the compression and expansion of the PVDF membrane as shown in Figure 4.20. As the pressure increases, temperature increases, but volume drops as the system undergoes compression. According to the I law of thermodynamics, as the system's energy is conserved, the transducer's ideal gas will exert pressure back to the system, which lead to increase in the volume of the transducer. Like the ideal gas volume increases, both pressure and temperature drop as the system experiences expansion depicted in Figure 4.20.

The elastic property of the PVDF membrane will aid in continuing this harmonic motion. This continuous change in the system's pressure-volume cycle will give rise to a change in the system's temperature (as PV=RT). During any of the cycle process, the cyclic integral of heat added to the system is proportional to the system's cyclic integral of work.

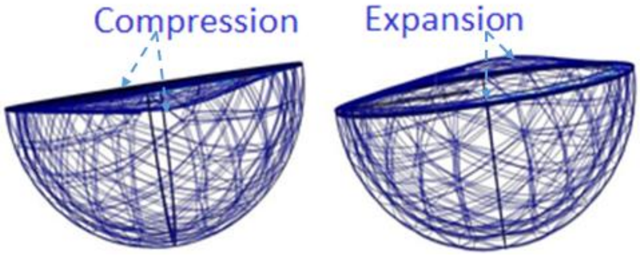

Figure 4. 20 Schematic of the contraction and expansion of the membrane (piston) of the system.

With the rise in pressure inside the transducer, the volume will decrease with an increase in temperature. Due to the limitation in gas molecules' mobility, excess residual energy has to be given out (due to energy conservation). The cyclic integral $\oint$ is used to show the energy conservation, the mathematical representation of this law is depicted in Equation (4.50).

$$\mathscr{J} = \oint \delta Q = \oint \delta W \tag{4.50}$$

$\mathscr{J}$ is the proportionality constant, known as the mechanical equivalent of heat. Q is the system's heat energy W is the work done by the system. This Equation relates mechanical energy with thermal energy.

4.2.3.1 Working of the proposed design

Consider a general case of an automobile and focusing on the area near its engine. Assume the STP's environmental conditions (Standard temperature and pressure (25 °C and 1 atm)). Initially, the automobile will be at rest, in off state (engine off), then after the ignition, and after time t, the engine encounter thermal losses and vibrational losses. Table 4.2 is the description of all thermal and vibrational losses events from initial time t_{intial} until final time t_{final}. It should always be remembered that the car generates two losses, vibrational losses and thermal losses, which will be harnessed by our transducer.

Table 4.2 The table describes the working condition of an automobile stat time to end time.

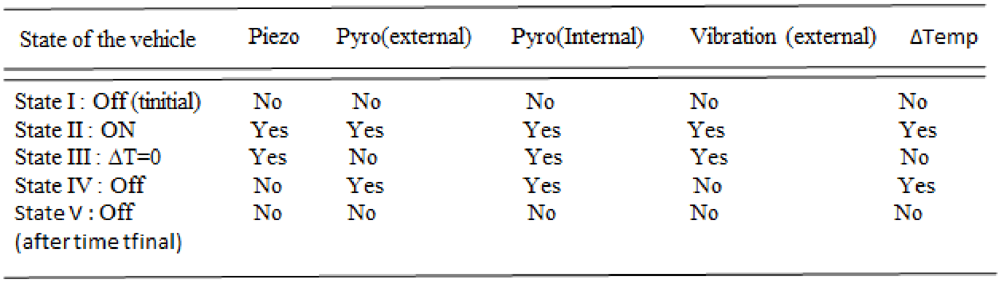

State of the vehicle	Piezo	Pyro(external)	Pyro(Internal)	Vibration (external)	ΔTemp
State I : Off (tinitial)	No	No	No	No	No
State II : ON	Yes	Yes	Yes	Yes	Yes
State III : ΔT=0	Yes	No	Yes	Yes	No
State IV : Off	No	Yes	Yes	No	Yes
State V : Off (after time tfinal)	No	No	No	No	No

State I: Describes initial working condition, such that State I=State V. When the car is at an off (at $t_{initial}$) state, there is no thermal nor vibrational energy. The transducer is neither absorbing nor emitting heat.

State II: When the car is in an ON state, due to vibrations from the automobile, the piezoelectric effect can be seen, and due to this vibration, the PVDF membrane will start exerting pressure on the gas due to which the temperature of the gas will also begin to increase. Simultaneously, as the ambient temperature will also increase, an increase in the transducer's outer layer's temperature, which is made up of SMA, will also experience the change in temperature, enhancing the pyroelectric effect.

State III: This is our primary working condition. It is a unique condition where, due to the external vibration, the thermal energy has been harvested at constant external temperature. At this stage, the vibrations from the automobile are present, and the vibrations will give rise to inflation and deflation of the PVDF membrane. However, the ambient temperature of the automobile will be constant. The outer layer of the transducer made up of SMA will not help in assisting the pyroelectric effect. Simultaneously, the PVDF membrane keeps on exerting pressure on the gas, which increases the pressure inside the closed system and changes the system's volume as the membrane is flexible. Hence a change in temperature inside the system can be seen. By this process, the pyroelectric effect can be seen inside the system.

State IV: When the automobile stops, the vibrations stop due to damping. So, there will not be any piezoelectricity effect in the system. Simultaneously, the automobile's temperature will also start to decrease. As the automobile is in the off state, the external temperature is reduced, which will help the transducer externally and internally generate the pyroelectric effect.

State V: At t_{final} condition; the internal and external thermal exchange will be completed, as the automobile is still at an off state, and there will be neither vibrations nor temperature gradient. Hence no electricity will be harvested. State V = State I.

4.2.3.2 Behaviour of gas:

4.2.3.2.1 Joule-Thomson Effect:

The Joule- Thomson effect describes the temperature change of a real gas or liquid when it is forced through a valve or porous plug, keeping them insulated so that there are no heat exchanges with the environment. This is called the Throttling or Joule-Thomson process. *Joule-Thomson coefficient* is used to measure the temperature change for a small change in pressure, based on the enthalpy and depicted in Equation. (4.51) Figure 4.17 presents the Joule–Thomson coefficients for various gases at atmospheric pressure.

$$\mu_{JT} = \left(\frac{\partial T}{\partial p}\right)_H = \frac{V}{C_p}(\alpha T - 1) \tag{4.51}$$

Where T is the rate of change of temperature, V is the volume of gas, C_P is the heat capacity at constant pressure, and α is the coefficient of thermal expansion. For Helium, Joule-Thomson Coefficient is almost constant over a wide temperature range (-70-1000 K). All real gases have an *inversion point* at which the value μ_{JT} of changes sign. The temperature of this point, the *Joule–Thomson inversion temperature*, depends on the pressure of the gas before expansion. Simultaneously, if specific heat is not constant, other thermodynamic laws are not applicable too. To avoid that, we have to use ideal gases. The ideal gas does not exist, but from Figure 4.21, we can see that helium is the gas that is very close to being called an ideal gas. That's the reason we are taking helium gas. After helium gas, hydrogen is the best-suited gas, but it is highly flammable.

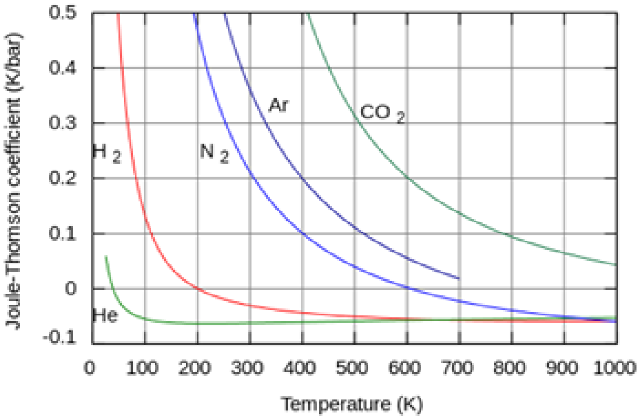

Figure 4. 21 Joule–Thomson coefficients for various gases at atmospheric pressure [114].

4.2.3.2.2 Volumetric Thermal Coefficient of expansion

In the general case of a gas, the volumetric coefficient of thermal expansion is given by Equation. (4.52):

$$\alpha_V = \frac{1}{V}\left(\frac{dV}{dT}\right)_p \tag{4.52}$$

Here, subscript p indicates that the pressure is held constant during the expansion. The subscript *V* stresses that the volumetric (not linear) expansion enters this general definition.

4.2.3.2.3 Compressibility Coefficient of gas

Compressibility or isothermal compressibility is a measure of relative volume change of a fluid with pressure is depicted in Equation. (4.53).

$$\beta_V = \frac{1}{V}(dV/dP)_T \tag{4.53}$$

Where β_V is the compressibility, for a significant change volumetric with pressure.

4.2.3.2.4 Potential change in temperature of the gas

A fluid package's potential temperature at pressure *P* is the package's temperature if adiabatically brought to a standard reference pressure P_O, usually 1000 millibars. The potential temperature is denoted θ and, for a gas well-approximated as ideal, is given by Equation. (4.54)

$$\theta = T(\frac{P}{P_0})^{\frac{R}{Cp}} \tag{4.54}$$

Where *T* is the current absolute temperature (in K) of the parcel, *R* is the gas constant of air, and *Cp* is the specific heat capacity at a constant pressure. R/Cp = 0.286 for air. For helium (T=20-220 C), it is 1:1.57.

The Joule-Thomson expansion consists of a thermally insulated system of which one side that is porous plug is a gas initially at $P1$, $V1$, and $T1$ (Pressure, volume, and temperature, respectively) and the other side is the external at $P2$, $V2$, and $T2$. In the absence of heat exchange with the surroundings, the total work done by the expanding gas equals the change in internal energy, which is given by Equation. (4.55).

$$w = \Delta U = P_1V_1 - P_2V_2 \tag{4.55}$$

For an ideal gas, $P_1V_1 = P_2V_2$, and the Joule-Thomson expansion would be at constant internal energy. However, the system proposed here uses helium gas, which is not an ideal gas. Meanwhile, helium is the closest to ideal among the other gases when considering the throttling effects. The change in enthalpy of the system in the Joule-Thomson expansion is given by Equation. (4.56):

$$\boldsymbol{\Delta H = \Delta U + \Delta(PV)} \tag{4.56}$$

Upon substitution of Equation. (4.56) into Eq. (4.55), we have:

$$\boldsymbol{\Delta H = 0}$$

i.e., the Joule-Thomson expansion is at constant enthalpy. It can be observed that when the Joule-Thomson expansion is carried out for several different pressure drops (*dP*) across the porous plug (or in our case, the flexible membrane) when different dT is measured, the plot of T vs. P is approximately linear with a slope equal to the Joule-Thomson coefficient (μ_{JT}) shown in Equation. (4.57).

$$\frac{\Delta T}{\Delta P} = \left(\frac{\partial T}{\partial P}\right) H = \mu_{JT} \tag{4.57}$$

For the modelling, we assume that μ_{JT} is negative (i.e., expansion leads to heating). However, the sign of μ_{JT} can also be positive (i.e. the gas cools down upon expansion). The so-called Joule-Thomson inversion temperature for specific gas will heat upon expansion, whereas below the inversion temperature will cool. At room temperature, common gases such as CO2, N2, and O2 cool upon expansion while He and Ne warm upon expansion. That is also another reason that made us chose helium.

4.2.3.2.5 Energy equation

As the system is reversible, the closed system's process by the first law of thermodynamics can be written as Equation. (4.58)

$$dU = TdS - PdV \tag{4.58}$$

Equation. (4.58) implies that the entropy *S* and the volume *V* are the two-state variables for which the differential of the internal energy *U* = *U (S, T)* becomes exact. This section transforms one essential pair of state variables to another, namely from (S, V) to (T, V), when one of the variables, here the entropy S, also takes a thermodynamic role potential.

The entropy is not an experimentally controllable variable, in contrast to *T*, *V*, and *P*, which allow measuring the thermal Equation of state

$$P = P(T, V) \tag{4.59}$$

Using Equation. (4.59) to deduce a relation, the energy equation allows determining the caloric equation of state *U* = *U (T, V)*. By Equation. (4.60), we can determine the internal energy of the system.

$$\left(\frac{dU}{dV}\right) = T\left(\frac{\partial P}{\partial T}\right)_V - P \tag{4.60}$$

The derivative of the internal energy is written with (4.60) in terms of measurable quantities. It is fulfilled for an ideal gas, for which *P V* = *mRT* and *(∂U/∂V) T* = *0*.

4.3 Simulation Results

A numerical model is developed to simulate the designed closed system design's performance as depicted in Table 4.3. The COMSOL Finite Element Analysis (FEA) software is used to estimate the performance using four different studies then an extensive simulation is carried out. The model is simulated with 3-D (three-dimensional) analysis. Figure.4.22 (a) and (b) illustrate the closed system working from the simulation. Three different studies are done to investigate the performance: (1) an Eigenfrequency Study to determine the first eigenfrequency (resonant) and its mode shape for all the six cantilevers, (2) a Stationary Study to check the total displacement and corresponding stress experienced by the system (3) a Time-Dependent Study Temperature distribution since heat transfer and distribution is a critical factor in this study. To guarantee mesh integrity, the ratio aspect of individual mesh elements should not be greater than three [116], the resulting mesh is shown in Figure 4.23.

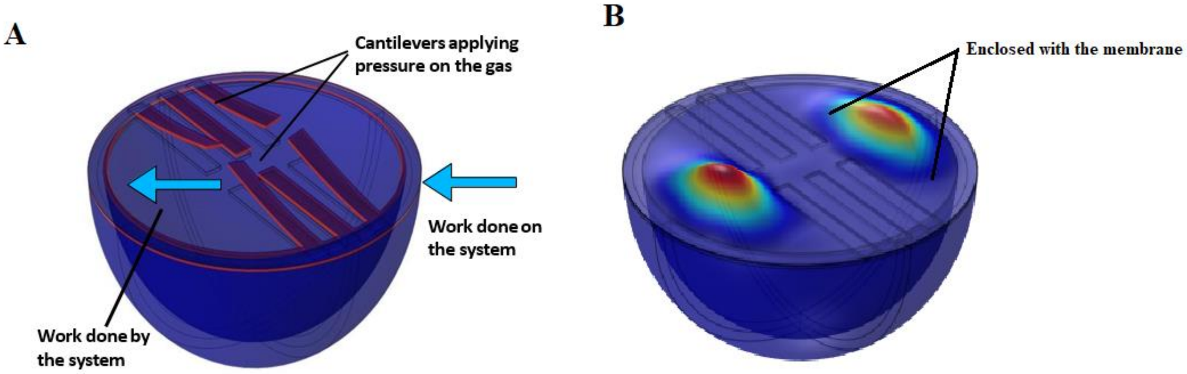

Figure 4. 22 *(a) and (b) illustrate the closed system working.*

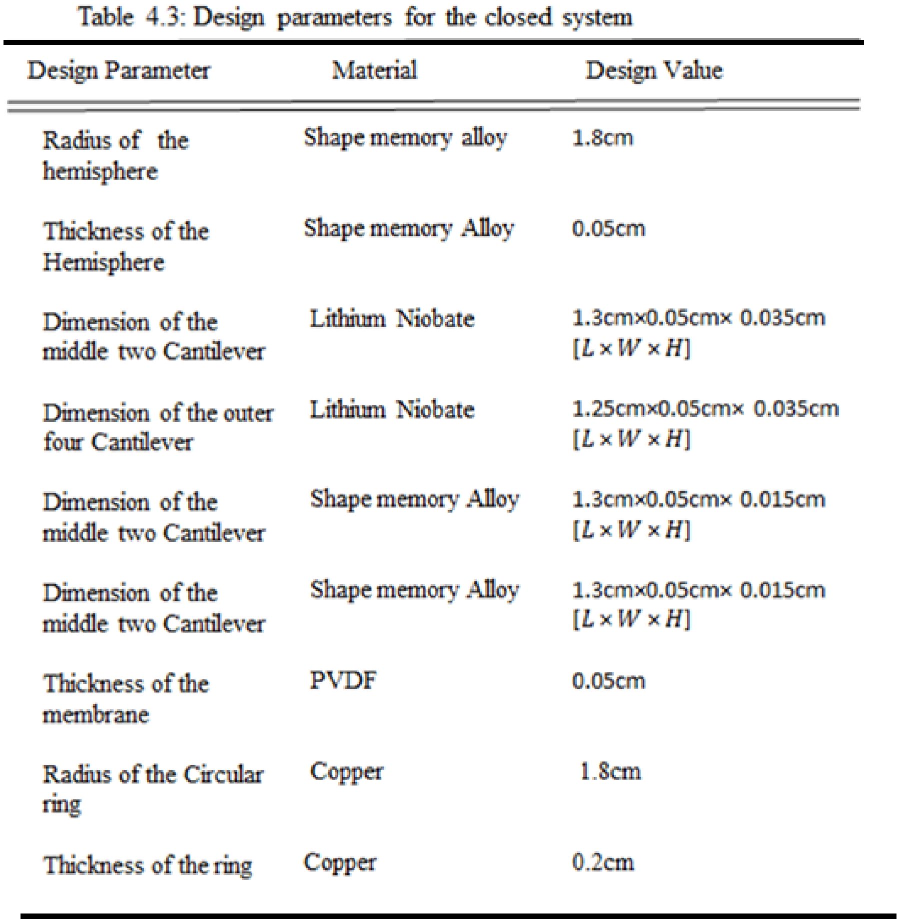

Table 4.3: Design parameters for the closed system

Design Parameter	Material	Design Value
Radius of the hemisphere	Shape memory alloy	1.8cm
Thickness of the Hemisphere	Shape memory Alloy	0.05cm
Dimension of the middle two Cantilever	Lithium Niobate	1.3cm×0.05cm× 0.035cm $[L \times W \times H]$
Dimension of the outer four Cantilever	Lithium Niobate	1.25cm×0.05cm× 0.035cm $[L \times W \times H]$
Dimension of the middle two Cantilever	Shape memory Alloy	1.3cm×0.05cm× 0.015cm $[L \times W \times H]$
Dimension of the middle two Cantilever	Shape memory Alloy	1.3cm×0.05cm× 0.015cm $[L \times W \times H]$
Thickness of the membrane	PVDF	0.05cm
Radius of the Circular ring	Copper	1.8cm
Thickness of the ring	Copper	0.2cm

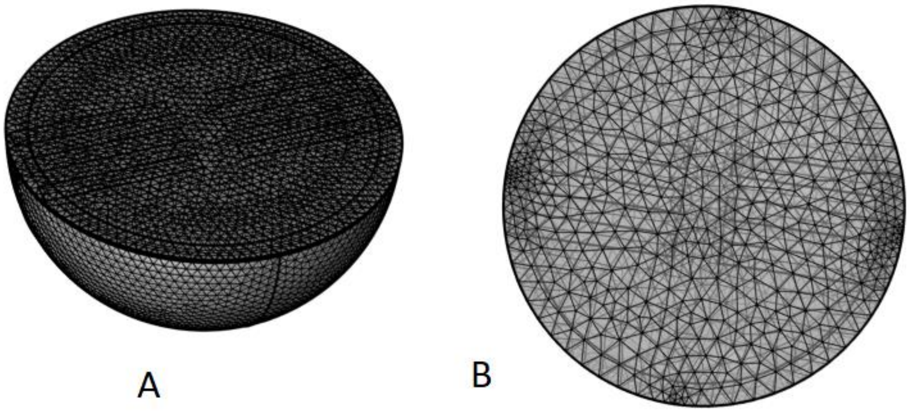

Figure 4. 23 Mesh quality of the closed system (A) Side view (B) Top view.

4.3.2.1 Eigenfrequency analysis

The designed closed system is analyzed by using FEA to determine its resonant frequencies and mode shapes. The resulting analysis is represented in Figure 4.24.

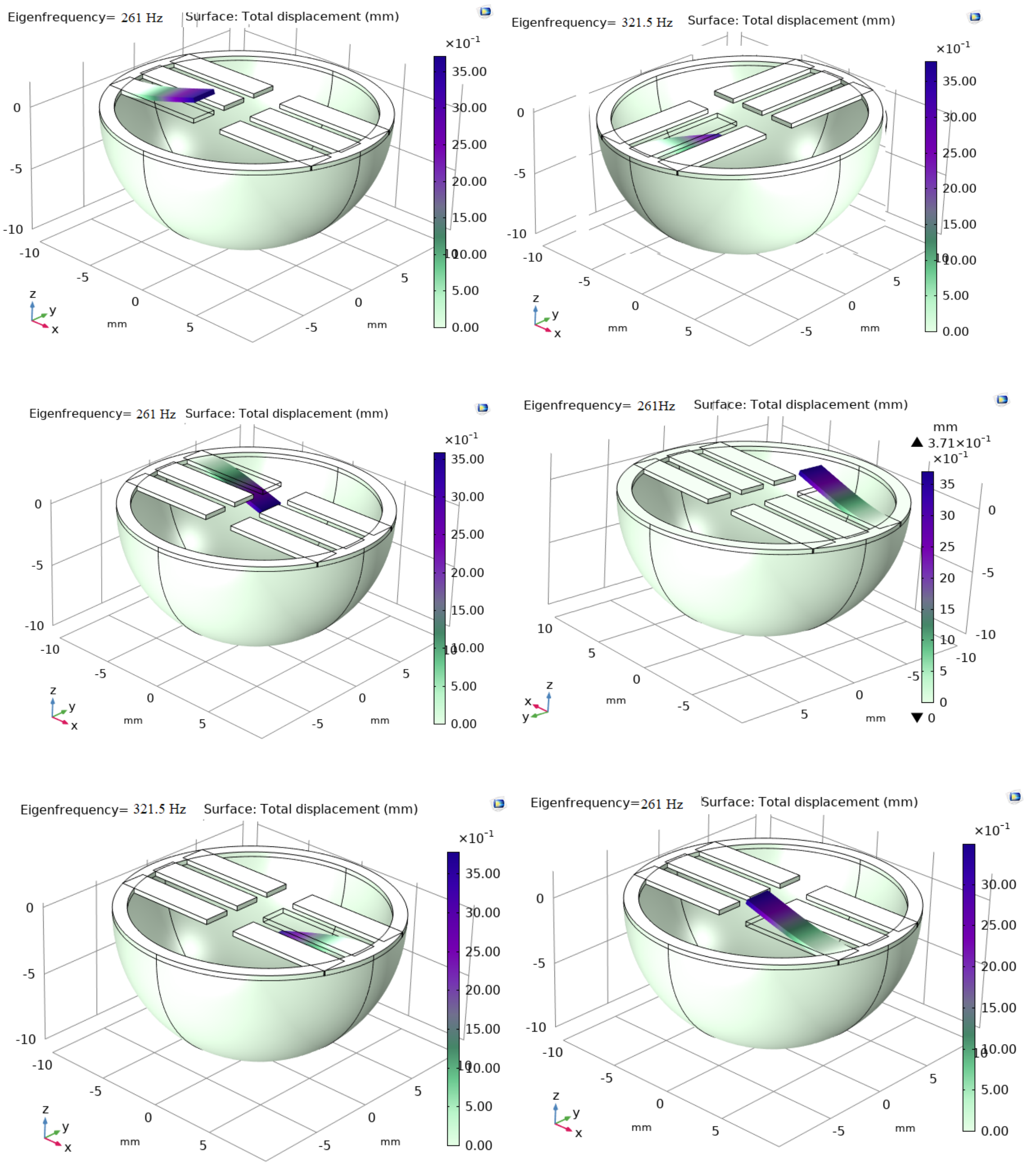

Figure 4. 24 Modeling the resonance frequency using COMSOL for multiple cantilevers (a) First cantilever first mode at 181Hz, (b) Second cantilever first mode at 321Hz, (c) Third cantilever first mode at 251 Hz, (d) Fourth cantilever first mode at 201 Hz(e) Fifth cantilever first mode at 241 Hz (f) Sixth cantilever first mode at 181Hz.

The conducted eigenfrequency study for all the six cantilevers to calculate the first five modes of natural frequencies of the system provided the numerical values synthesized in Table 4.4. It was found that the eigenfrequency was the same for the Four Cantilevers as they have the same length, width, and thickness as well have similar placement in the structure. In contrast, the two other cantilevers have identical eigenfrequency value.

Table 4.4 Eigen frequencies by finite element model
(Rf = Resonance frequency)

Cantilever	Rf1	Rf2	Rf3	Rf4	Rf5
First Cantilever	181 Hz	225 Hz	668Hz	1015 Hz	1158Hz
Second Cantilever	321 Hz	455 Hz	721Hz	1208 Hz	1601Hz
Third Cantilever	251 Hz	525 Hz	768Hz	1158 Hz	1758Hz
Fourth Cantilever	201 Hz	368 Hz	708Hz	1101 Hz	1350Hz
Fifth Cantilever	241 Hz	587 Hz	705Hz	1121 Hz	1654Hz
Sixth Cantilever	181 Hz	225 Hz	668Hz	1015 Hz	1158Hz

4.3.2.2 Stationary Study

A static FEA analysis is done to determine the system's total displacement and corresponding stress. Figure 4.25 (a) shows the total displacement of the PVDF membrane, measured to be 0.19 µm. Figure 4.25 (b) Shows the von mises stress (N/m^2) in z-direction for the PVDF membrane which is 6.6×10^{5}.

Simultaneously, in this study, we calculated the total deflection experienced by each cantilever. We also calculated the stress generated on all the cantilevers and is depicted in Figure.4.26.

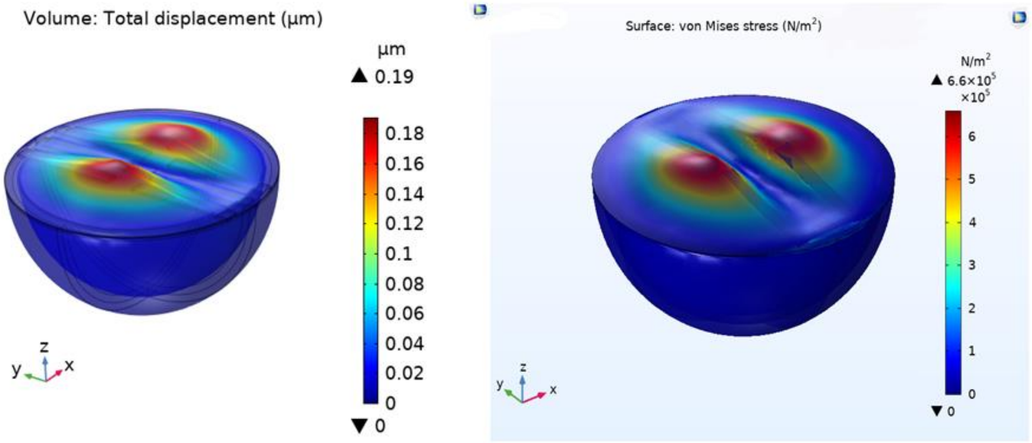

Figure 4.25 FEA simulation results for PVDF membrane under stationary study (a) total displacement of the PVDF membrane (b) Stress development on the membrane.

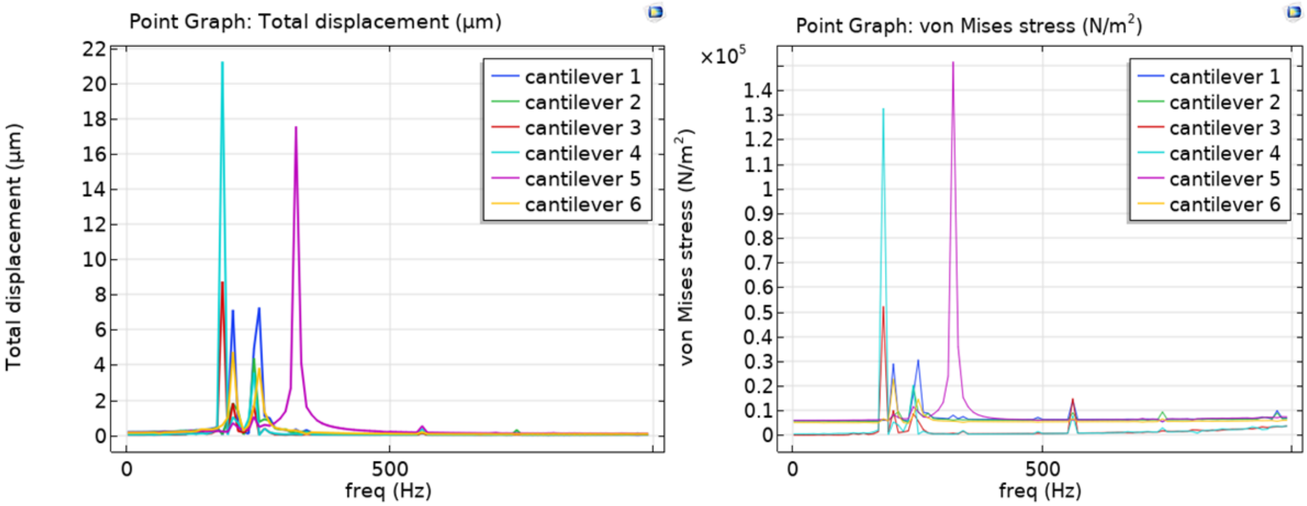

Figure 4. 26 FEA simulation results for Cantilever beam under stationary study (a) displacement of the cantilevers (b) Stress development on the cantilevers.

4.3.2.3 Time-Dependent Study

A Time-Dependent Study based on the Temperature distribution was done as the heat transfer and distribution are critical factors in this research. In this study, we focus on how the gas temperature changes over time and how long duration it lasts when the device's outside temperature is constant. We take an arbitrary point inside the system to calculate the gas's temperature, as shown in Figure 4.27.

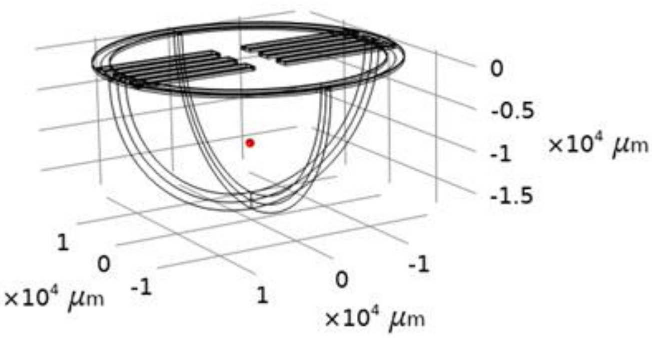

Figure 4.27 Schematic to represent the arbitrary point inside the closed system.

The simulation was conducted for 8 hours, and it was seen that the gas temperature kept on fluctuating during this period. After that, there was no more change in temperature as schematic in Figure.4.28. In the Figure we represented the temperature for both the (a) gas temperature and the (b) temperature of the cantilever.

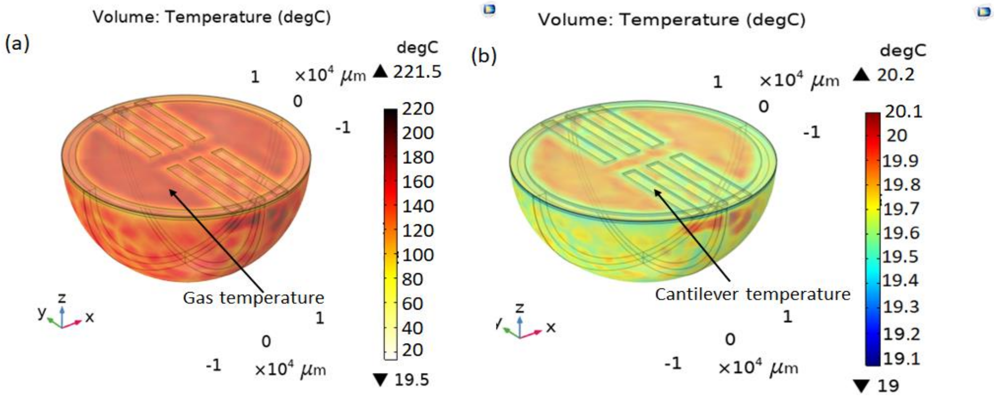

Figure 4. 28 (a) gas temperature and the (b) temperature of the cantilever after 8 hours.

This study noticed that the gas's temperature rate was higher than of the cantilever. Indeed the system consists of three different materials like a polymer, single crsytal, and metal with different CTE, leading to a higher temperature longer time for the activation. For the gas, the temperature changed from 19.5 °C to 221.5°CThe temperature change was lower for the cantilever since their temperature varied between 19 °C till 20.2°C.

Here in Figure 4.29 a) graphical representation of the change in gas temperature is shown inside the closed system in Figure 4.29 b) a zoom representation of the change in temperture of the gas inside the closed system is shown which continued for 8 hours , at constant ambient temperature.

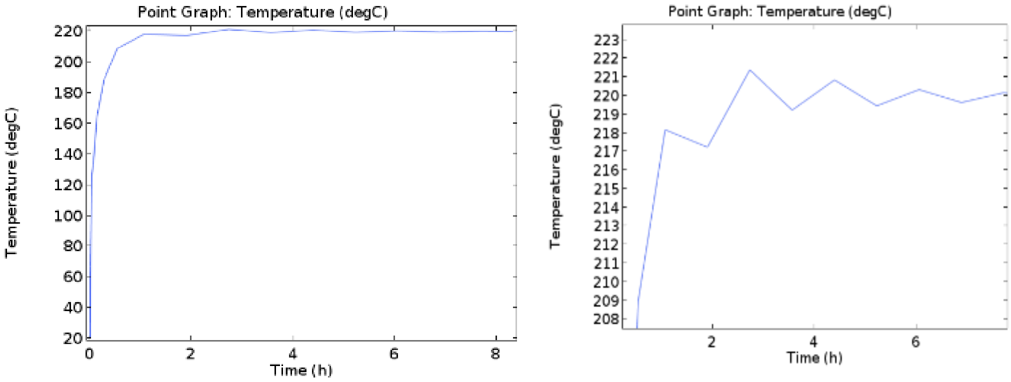

Figure 4. 29 (a) change in gas temperature inside the closed system (b) a zoom representation of the gas temperature change from 1-8 hours between (218°C-222°C).

This research aims to study the change in temperature of the gas when the outside temperature is constant. We plotted the graph for the outside temperature and the temperature of the gas at the same condition. The simulation result shows that the gas temperature fluctuated for 8 hours when the outside temperature was constant. The gas temperature stopped increasing after reaching 220°C in 1 hour, but fluctuation continued, depicted in Figure 4.30(A). We can conclude that this system can harvest the thermal (pyroelectric energy) for 8 hours even when the outside temperature is stable. Figure 4.30 (b) the point representation is shown on the transducer, where point no 79 (in red colour) was inside temperature of the gas and point 77 was the ambient temperature (in blue colour), and the same colour represented is used in the graph.

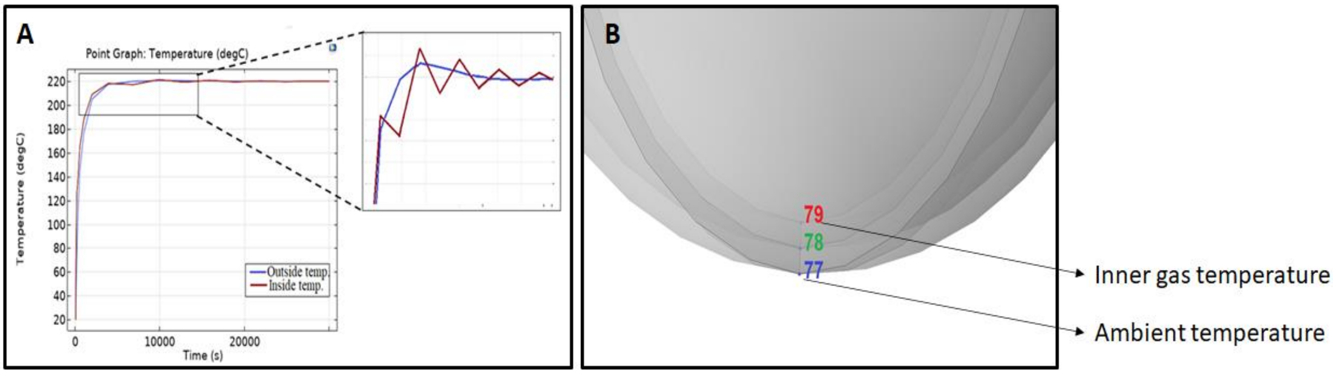

Figure 4.30 Comparison of the temperature change for the inside (gas) and outside (ambient) at similar conditions.

We now explore the output power of the device. We calculated the total stored electrical energy of the device, which was 0.9 J at an operating frequency of 561Hz. Figure 4.31 shows the stored energy.

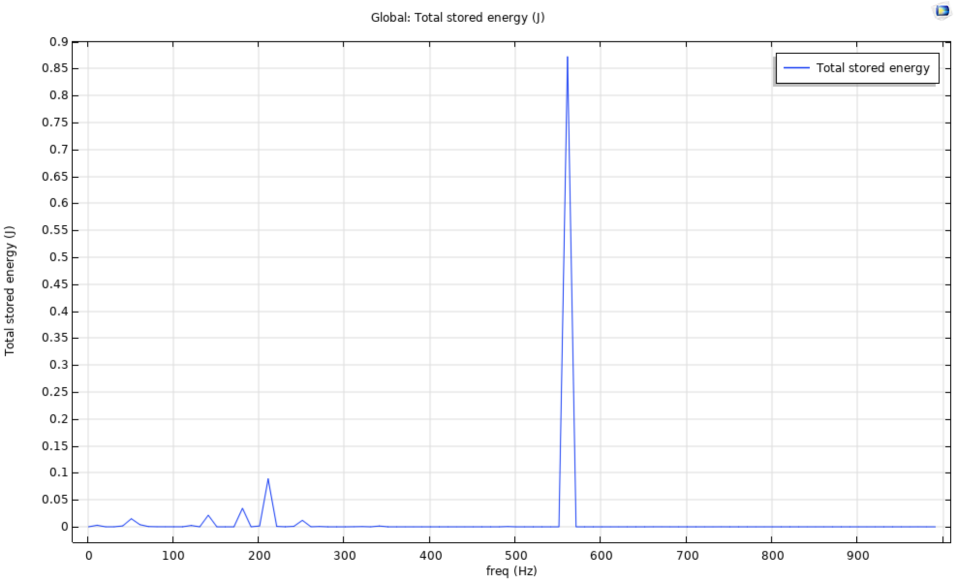

Figure 4.31 Total stored electrical stored energy of the closed system.

We also calculated the system's total voltage which was the sum of all the voltages we received from all the cantilevers, which is described in Figure 4.32, where we notice the maximum value for the output value as 30V. It is important to note that for all the cantilevers, we noticed different output voltage, but the maximum voltage was obtained from the cantilever at 225Hz.

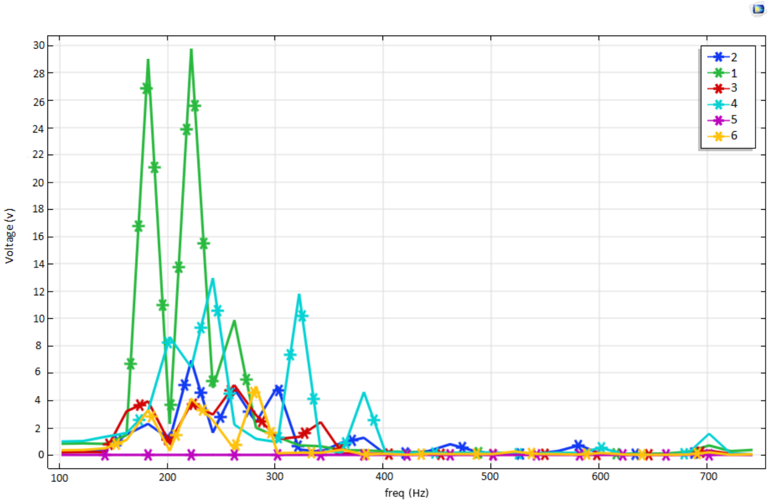

Figure 4.32 Total Output voltage from the closed system.

In this simulation, we also study the load impact on the device, and we calculated the output power. The maximum electrical power of 500 nW was attained in this simulation for a 600 kΩ resistive load. Simultaneously we observed the mechanical power corresponding to. Here in Figure 4.33, the output electric power and the input mechanical power are depicted.

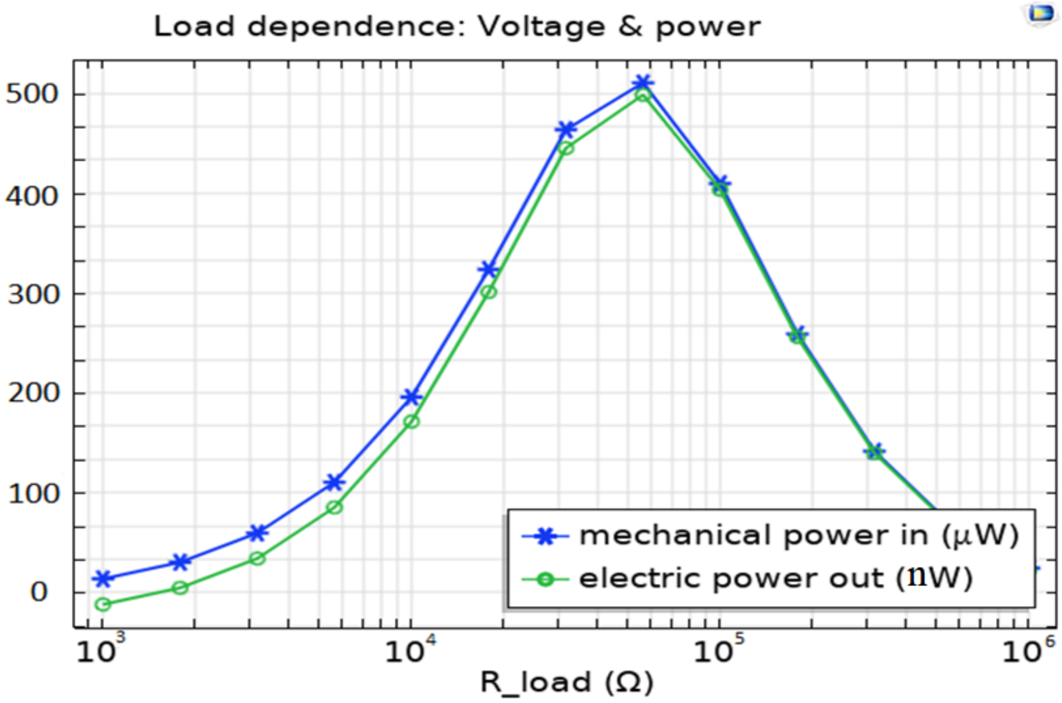

Figure 4. 33 The output electric power and the input mechanical power as a function of load.

4.4 Conclusion

This chapter introduces an initial design of a thermal energy harvesting mechanism. This mechanism consists of Lithium Niobate, a shape memory alloy, and two neodymium magnets, enabling both piezo- and pyro-effect. The output power is higher with two magnets than without magnets. A prototype was built and tested under the different frequencies of heat sources. A maximum peak power output of 290 nW was obtained at the optimal condition when the load resistance is 2.5MΩ. Without magnet, output voltage appears as a sinusoidal curve following the temperature fluctuation. Using two magnets to achieve a more significant motion range results in large spike peaks due to the beam's snapping as the latter is attached to or released from the magnet. As a consequence, piezoelectric effect is more noticeable when using the magnets. The power with magnet's presence is about ten times higher at 0.04 Hz than without magnets. Experimental tests qualitatively validated the concept of hybrid energy harvesting mechanism to exploit both the piezo and pyroelectric effects.

The second design of hybrid energy harvesting, in this chapter was based on a closed system that employs both the pyroelectric effect and piezoelectric effect for the thermal and vibrational energy conversion consists of Lithium Niobate, a shape memory alloy and PVDF. Beyond the fact that it is hybrid, the design features include harvesting the thermal energy at constant temperature and uses lead-free piezoelectric material. While the constant temperature harvesting capability is based on the Joule-Thomson effect, Lithium Niobate and PVDF piezoelectric materials are used for the lead-free material. Extensive simulation with COMSOL Multiphysics software has been carried out and shows the potential of the proposed design. Future works include improving the design, fabrication and experimental validation for a more realistic approach.

5. Design, modelling and simulation of electrical circuit for the hybrid energy harvesting device

In recent years Piezoelectric harvesting micro-generators have been widely studied, and nonlinear energy extraction methods have been developed to optimize their performances. When it comes to hybrid systems, the input sources of energies are of different natures and definitely work on different frequencies, which consequently render piezoelectric materials-based energy harvesting challenging, moreover thermal energy sources work on a significantly less frequency range (less than 1 Hz). Hence, in previous chapters, to combine these forms of energy, we proposed nonlinear techniques of energy harvesting. As a consequence, nonlinear techniques of electrical circuits are also suitable for such hybrid energy harvesting. For example, the Synchronous Electric Charge Extraction (SECE) [115] *for a piezoelectric harvester could significantly enhance the electromechanical conversion while tackling the impedance matching issue. The present study investigates the SECE method applied to thermal-vibrational harvesters.*

5.1. Introduction

Piezoelectric energy harvesters have been vastly studied for energy generation from external vibrations. The highest output power can be obtained at a resonance situation when the external vibration frequency matches the harvester's resonance frequency. However, the environmental vibrations generally have low frequencies (0-100 Hz). Moreover, as temperature variation exhibits very low frequency (generally less than 1 Hz), pyroelectric effect-based energy harvester suffers from low power. Consequently, designing hybrid harvesters that scavenge thermal and vibrational energies is very challenging in our situation where both frequencies are low. In previous chapters, we proposed nonlinear harvesting technique based on magnets as well as closed-system based on the Joule-Thomson effect to scavenge energies from low frequencies temperature/vibration and to scavenge energies from constant temperature and low frequency vibration respectively. An electrical circuit is necessary to adapt the output voltage from each of these harvesters to a constant and regulated voltage supplying any load. If well designed, the electrical circuit could even improve the performance of the entire energy harvesters, from the transduction to the supply. Few research groups have shown that implementing a nonlinear circuit to the piezoelectric harvester can significantly enhance the electromechanical conversion, leading to outstanding overall energy harvesting performance [116]. The main advantage of using these nonlinear methods in electrical circuits in this research is that the treatments are not limited to the piezoelectric effect but can also be adapted to numerous types of energy conversion. Here, it is also used for pyroelectricity. Therefore, this research aims to give a concept of energy harvesting circuits that can work with two different frequencies and harvest energy from numerous energy sources present in our environment, in our situation the surroundings temperature and vibration

5.2. Network Topology

This section aims to briefly expose the different techniques in energy harvesting from the piezoelectric effect and pyroelectric effect, to have a comprehensive view of each process, making the further theoretical development more understandable.

5.2.1. Standard Technique

The standard circuit for energy harvesting technique consists of simply connecting the piezo element to a diode bridge-based rectifier with a smoothing capacitor C_S Figure.5.1(a) depicts the schematic when the load is resistive denoted R, where V_0 and V_{DC} are the piezo element voltage and load voltage, respectively, and C_0 is the capacitance of the piezo element. When the absolute value of the piezo voltage V_0 is less than the rectified voltage V_{DC}, the bridge rectifier is blocked, and the piezo element is let in an open circuit. When the absolute value of V_0 is more significant than V_{DC}, the bridge rectifier conducts, and a charge flow appears from the piezoelectric element to the smoothing capacitor until the current is cancelled (which occurs when the displacement velocity is null)[117]. This is depicted in Figure.5.2 (a), which shows the standard technique's typical waveforms.

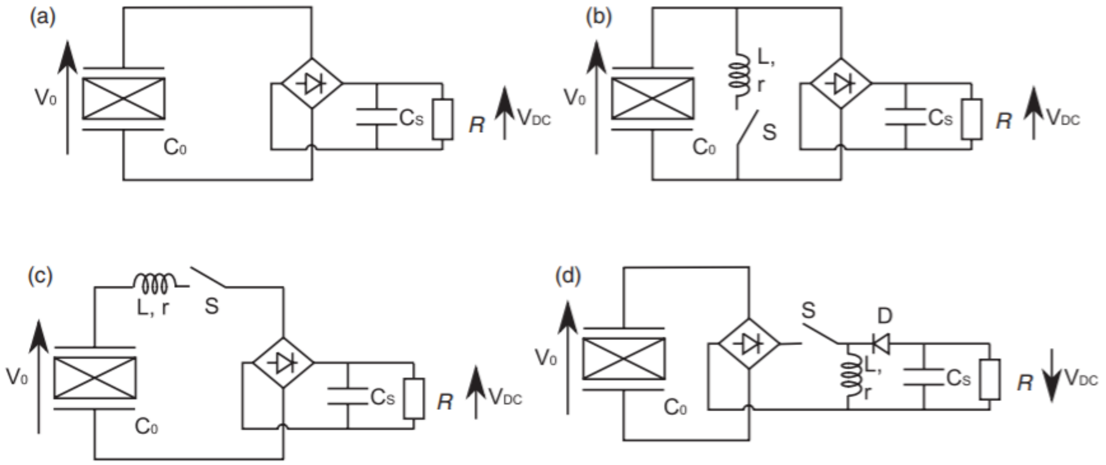

Figure 5. 1. Energy harvesting technique schematics: (a) standard, (b) parallel SSHI, (c) series SSHI, (d) SECE. [116].

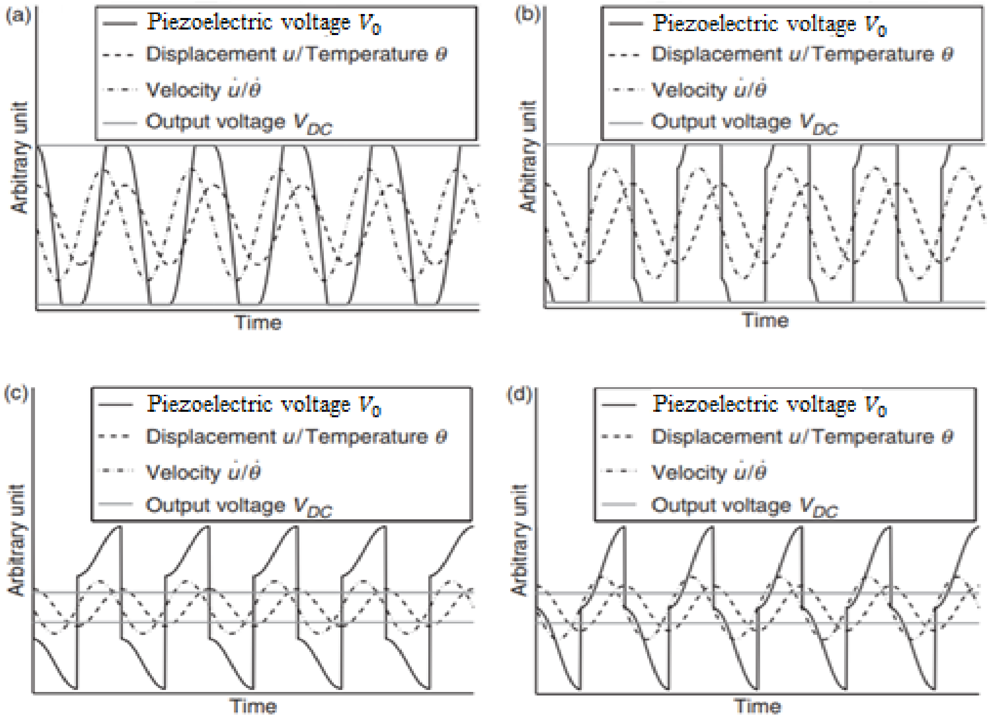

Figure 5. 2 Typical waveforms for each technique: (a) standard, (b) parallel SSHI, (c) series SSHI, (d) SECE [117]

5.2.2. Nonlinear Techniques

5.2.2.1 Parallel synchronized switch harvesting on inductor

The basic schematic of the parallel Synchronized Switch Harvesting on Inductor (SSHI) is depicted in Figure.5.1 (b). Compared to the standard technique, in parallel SSHI, an inductor L has been added in parallel with the piezo element (that has an internal resistance r) and in series with switch S controlled digitally. Just after the energy transfer process (i.e., when the displacement reaches an extremum), the switch S is briefly closed, thus shaping an oscillating electrical network by connecting the piezo capacitance with the inductor L. The switch closing time period is given as half the period of the LC_0 circuit. There is thus an inversion of the piezo voltage. However, we can say that the inversion is not perfect due to internal losses and is characterized by the coefficient γ that can be expressed as a function of the electrical quality factor Q_i, whose typical value is 0.6–0.8. Related waveforms are presented in Figure.5.2 (b).

5.2.2.2 Series synchronized switch harvesting on inductor

The series SSHI, which Taylor et al. (2001) proposed, consists of inductor L connected to the piezo element in series. Here the command for the switch is synchronized with the charge available on the piezo element. The switch remains turned on when this charge is maximal (i.e., when the displacement is maximal or minimal). Thus, a charge flow appears from the piezo element to the smoothing capacitor through the inductance L and the switch S. The charge flow is stopped when the current is null, which occurs when the voltage inversion is complete. In this case, this voltage inversion is referenced to V_{DC} (according to a minimum or maximum switching), while in the parallel SSHI, the reference voltage is zero. Figure.5.2(c) depicts the typical waveforms of the technique.

5.2.3 Synchronous electric charge extraction (SECE)

The principles of the Synchronous Electric Charge Extraction (SECE) differ slightly from the previously exposed techniques. The first step in SECE techniques is to convert the electrostatic energy available on the piezo element to electrical energy by connecting the piezo element to the inductance L when the electrostatic charge is maximal (i.e., when the displacement reaches an extremum). Then, when the piezo voltage reaches zero, the switch S is open, and the electromagnetic Energy on L is transferred to the smoothing capacitor C_S (Figure.5.1 (d)). Thus, with this technique, there is a total decoupling of the harvesting stage from the storage stage. The typical SECE waveforms are presented in Figure.5.2 (d).

In the standard energy harvesting circuit comprising an AC– DC rectifier, a filtering capacitor C_R, and for supplying an electrical load R_l in parallel, as shown in Figure.5.1 (a), to ensure a nearly constant DC voltage V_{DC} [119], C_R should be large enough such that the time constant R_lC_R is much larger than the oscillating period of the harvester. The rectifier will be blocked at the steady state when $V < V_{DC}$ and will conduct and transfer Energy when V reaches V_{DC}. The waveform of the voltage V across the PEH is shown in the Figure.5.3 (a) [120]. The main components of the SECE circuit comprise an inductor L_{SCE}, a diode D_{SCE}, and a switch S, as shown in Figure.5.3 (a). The switch S remains opened most of the time within one vibration period except for the two instances (t1 and t2 in Figure.5.3 (b)) at which the PEH's deflection reaches a maximum. Once the PEH bends to its maximum deflection, S will be closed for a short time for energy transfer. Hence, the voltage across the PEH at these instances quickly drops to zero. The control circuit's power consumption to turn the switch on and off can be compensated from less than 5% of the harvested power [120]. At the steady state, the voltage waveform is assumed to have the profile shown in the Figure.5.3 (b) [120]. This assumed profile will be verified in later circuit simulation.

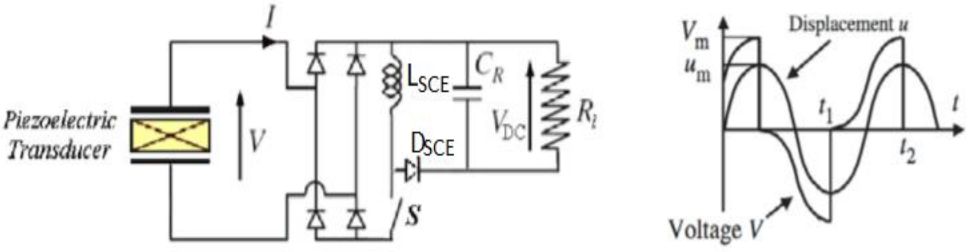

(a) (b)

Figure 5. 3. (a) An SECE energy harvesting circuit and (b) corresponding voltage across PEH and displacement waveform [120].

5.3. Modelling and theoretical development

In the following work, we have exposed a hybrid-switching interface for piezo/pyro harvesting. The concept mainly focuses on the pyro energy extraction through the SECE interface as we know pyro energy extraction is one of the main challenges in research; however, along with pyro energy extraction, we are also focusing on extracting the piezo energy, which means the system will be working on two different frequencies. Here in the design, we will be working in the SECE nonlinear switching pattern, which works perfectly fine for the weakly coupled structure, and which will be done w.r.t. the temperature. Our main aim here is to follow this strategy because knowing the fact that switching only on the high-frequency piezo response "erases" the pyro one, which yield less energy. Therefore, we made few assumptions such as the pyro energy will be more in comparison to the piezo energy, which made us choose materials having high pyroelectric coefficient, not the piezoelectric coefficient.

Regarding electromechanical model, it relates the mechanical and electrical variables of the harvesting system. There are varieties diverse and complex models, including lumped- parameter models, Rayleigh-Ritz type approximate distributed parameter models and numerically distributed parameter FE solution attempts. Whereas we know that Lumped parameter model has limited degrees of freedom, a distributed parameter model has infinite degrees of freedom. Hence, the former is simpler and widely used while the latter is complicated though accurate. Here, we have used the lumped parameter model. The mechanical structure bonded with piezoelectric elements can be modelled by the 'mass + piezo + spring + damper' model with only one degree of freedom. This model is shown in Figure.5.4, which summarizes a vibrational structure when the piezoelectric generator is vibrating near its resonance frequency [121].

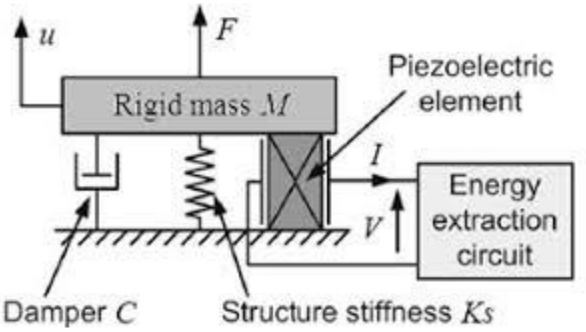

Figure 5. 4 Electromechanical models of the piezoelectric energy harvesting system [121].

Theoretical developments in the case of vibrations have already been exposed [121], based on a simple but realistic spring-mass model of an electromechanical structure as depicted in Figure 5.3 [122], The issuing model is given in Equations (5.1), with M, C, KE the dynamic mass, structural damping coefficient, and short-circuit stiffness of the spring-mass system, respectively, In the model, F is the driving force. u is the flexural displacement of the structure, and v the strain rate that is equivalent to the velocity of displacement (speed) if a constant strain under the piezoelectric element is assumed. This assumption is valid if the structure is excited at one of its resonance frequencies and if the dimensions of the piezo actuator are minimal compared to the mode shape as described by some research group earlier. V and I are the voltage and the current flowing out of the piezo element, and α and C_0 the force factor and blocking capacitance of the piezoelectric element, with e and S the piezoelectric constant and permittivity, respectively, and A, l the piezoelectric surface and thickness, respectively. Here both the piezoelectric and pyroelectric energy harvesting techniques will be presented in this section. It is important to note that in this last case, only forced temperature variation magnitude can be seen due to the specific nature of the pyroelectric effect (indeed, no resonance appears in such systems).

$$M\ddot{u} + C\dot{u} + K^E u = F - \alpha V \tag{5.1}$$

5.3.1. Energy extraction using the piezoelectric effect

In this case, only the electrical piezoelectric Equation (5.2) needs to be considered. D, E, and S are given as the electrical displacement, electric field, and strain, respectively. ε^S and e are the permittivity's and the voltage constant of the piezoelectric element, respectively. Considering Ampere's circuital law and as ferroelectric elements are not subject to a magnetic field, the electrical displacement, assumed to be uniform, can be expressed as a function of the current I flowing out of the piezoelectric element in Equation (5.3) (A is the surface of the piezoelectric element). Therefore, considering that the electric field and the strain are constant Equation (5.4), with u the structure's flexural displacement. In this equation, A and C_0 are defined as the force factor and clamped capacitance, respectively, whose expressions are given by Equation (5.5), with l the piezoelectric element's thickness.

$$D = \varepsilon^S E + eS \tag{5.2}$$

$$I = -A\frac{\partial D}{\partial t} \tag{5.3}$$

$$I = \alpha_{piezo} u - C_0 V \tag{5.4}$$

$$\alpha = -\frac{eA}{l} \; ; \; C_0 = \frac{\varepsilon^S A}{l} \tag{5.5}$$

Therefore, in a condition where the piezoelectric element is let in an open circuit (step 1 in Figure.5.3), the current flowing out the piezo element is null (I=0), and therefore the voltage varies with the displacement as given in Equation (5.6), with K is stiffness constant. The value of K is obtained by considering the end of the previous energy extraction process, yielding in Equation (5.7). The value of the displacement u_1 at the initial stage of the energy transfer process is obtained when V reaches V_{DC}, leading to Equation (5.8).

$$V = \frac{\alpha}{C_0} u + K \tag{5.6}$$

$$K = -V_{DC} + \frac{\alpha}{C_0} u_M \tag{5.7}$$

$$u_1 = 2\frac{C_0}{\alpha} V_{DC} - u_M \tag{5.8}$$

Therefore, in the whole energy transfer process, the total amount of transferred energy to the load is given by Equation (5.9). Due to the fact that the energy transfer process occurs twice a period, the total amount of harvested energy per period becomes Equation (5.10), and its maximal value leading to the maximal harvested energy per cycle is given by Equation (5.11), which can also be expressed as a function of the piezoelectric element parameters, with S_M the maximal value of the strain over the piezoelectric element.

$$W = \int IVdt = \alpha V_{DC}\,(u_M - u_1) = 2V_{DC}(\alpha u_M - C_0 V_{DC}) \tag{5.9}$$

$$W_{piezo} = 4V_{DC}(\alpha u_M - C_0 V_{DC}) \tag{5.10}$$

$$W_{piezo} = \frac{\alpha^2}{C_0} u_M^2 = \frac{e^2 A l}{\varepsilon^S} S_M^2 \tag{5.11}$$

5.3.2 Energy extraction using pyroelectric effect

In the pyroelectric effect, the electrical Equation (5.1) becomes (5.12), with θ the temperature and p and ε^{θ} the pyroelectric constant and the pyro elements' permittivity. Using the same concept as in the piezoelectric energy harvesting case leads to the same expression of the current flowing out of the pyroelectric part by Equation (5.13), but α and C_0 are defined by Equation (5.16). Considering that the amplitude of the temperature variation θ_M remains constant, the same development stands for the standard technique applied to thermal energy harvesting. Thereafter, the total harvested energy per cycle yields the Equation (5.17) and the maximal harvested energy per cycle Equation (5.18).

$$D = \varepsilon^{\theta} E + p\theta \tag{5.12}$$

$$I = -A\dot{D} \tag{5.13}$$

$$I = -A \in^T \dot{E} - Ap\dot{T} \tag{5.14}$$

$$I = \alpha_{pyro}\dot{T} - C_0\dot{V} \tag{5.15}$$

$$\alpha = -pA\ ;\ C_0 = \frac{\varepsilon^T A}{l} \tag{5.16}$$

$$W_{pyro} = 4V_{DC}(\alpha T_M - C_0 V_{DC}) \tag{5.17}$$

$$W_{pyro} = \frac{\alpha^2}{C_0}u_M^2 = \frac{p^2 Al}{\varepsilon^T}T_M^2 \tag{5.18}$$

5.3.3 Assumptions

While working with the switching technique, we made few assumptions to make the concept easy to understand.

- For the given study, we neglect the backward piezo coupling (no damping, constant displacement magnitude)
- Here we worked on two frequencies (piezo – f_{piezo} - and pyro - f_{pyro}), which are far away from each other, and their ratio is not an integer.
- We have assumed the Pyro voltage magnitude is much higher than the piezo voltage (otherwise pyro energy will be negligible).

$$I_{Piezo} = \alpha_{piezo}\dot{u} - C_0\dot{V}_{piezo} \tag{5.19}$$

$$I_{Pyro} = \alpha_{pyro}\dot{T} - C_0\dot{V}_{pyro} \tag{5.15}$$

Where I is outgoing current, V is the output voltage, u is displacement, T is the temperature, α is Force (piezo)/entropy (pyro) factor, and C_0 is the clamped capacitance.
Assuming sine displacement and temperature (around mean temperature T_0), we have:

$$u = u_M \sin(\omega_{piezo}t) \tag{5.20}$$

$$T = T_M \sin(\omega_{Pyro}t) \tag{5.21}$$

Where,

$$\frac{\omega_{Piezo}}{\omega_{Pyro}} \gg 1$$

Where U_M is displacement magnitude, T_M is temperature variation magnitude, and ω is the angular frequency

5.3.4 Switching part

In the switching part, each piezo energy extraction will be doubled because of the previous switch.

5.3.4.1 The calculation for the piezo part,

For calculating the electrical energy due to the piezoelectric effect, the following equation can be used

$$E_{Piezo} = \frac{1}{2} C_0 V_{max}^2 = \frac{1}{2} C_0 \left(2 \frac{\alpha_{Piezo\, U}}{C_0}\right)^2 = 2 \frac{\alpha_{piezo}^2}{C_0} U_M^2 \qquad (5.22)$$

If we set a threshold Thresh = cos (β) ω pyro T_M where (β =conduction angle) with this threshold the switching was done between the two different frequencies, here we have depicted the threshold condition.

$$|\dot{T}| = |T_M \omega_{pyro} \cos(\omega_{pyro} t)| < thresh = |\cos(\omega_{pyro} t)| < |\cos(\beta)| = \frac{\beta}{\omega_{pyro}} < t > \frac{\pi - \beta}{\omega_{pyro}}$$

The average number N_{piezo} of piezo switches will take place twice in a period, which is due to the vibration (piezoelectric effect).

Here, the piezo power can be represented by half a pyro period [$2\left(\frac{\pi - 2\beta}{\omega_{pyro}}\right) f_{piezo}$].

Also, when we calculate the piezo power, which is half a pyro period, we obtain Equation (5.23): Where,

$$P_{Piezo} = 2N f_{pyro} E_{piezo} = 4N f_{pyro} \frac{\alpha_{piezo}^2}{C_0} u_M^2 = 8\left(\frac{\pi - 2\beta}{\omega_{pyro}}\right) f_{piezo} f_{pyro} \frac{\alpha_{piezo}^2}{C_0} u_M^2$$

$$= 8\left(\left(\frac{\pi - 2\beta}{\omega_{pyro}}\right) f_{piezo} \frac{\alpha_{piezo}^2}{C_0} u_M^2\right) \qquad (5.23)$$

$$\beta = 0 = P_{piezo} = 4 \frac{\alpha_{piezo}^2}{C_0} u_M^2 = \text{(this will work the same as a pure SECE)}$$

$$\beta = \frac{\pi}{2} (only\ pyro) = P_{piezo} = 0$$

5.3.4.2 The calculation for the pyro part,

For calculating the electrical energy due to the pyroelectric effect, the following equation can be used

$$E_{Piezo} = \frac{1}{2} C_0 V_{pyro\ max}^2 \tag{5.24}$$

$$V_{Pyro\ max} = \frac{\alpha_{pyro}}{C_0} |\int dT| = \frac{\alpha_{Pyro}}{C_0} \left| \int_{\pi-\beta}^{\pi+\beta} T_M \omega_{Pyro} \cos(\omega_{pyro} t) dt \right| \tag{5.25}$$

$$V_{Pyro\ max} = \frac{\alpha_{pyro}}{C_0} T_M [\sin(\pi - \beta) - \sin(\pi + \beta)] \tag{5.26}$$

$$V_{Pyro\ max} = \frac{\alpha_{pyro}}{C_0} T_M \sin(\beta) \tag{5.27}$$

After calculating the value for V $_{\text{pyro max}}$ it can be implemented in Equation (5.27) to get the electrical energy generated by the pyroelectric effect.

$$E_{Pyro} = 2 \frac{\alpha_{pyro}^2}{C_0} [\sin(\beta)] T_M^2 \tag{5.28}$$

On the other hand, the pyro power (two extractions per period) is:

$$P_{Pyro} = 2 f_{pyro} E_{pyro} = 4 f_{pyro} \frac{\alpha_{pyro}^2}{C_0} [\sin(\beta)]^2 T_M^2 \tag{5.29}$$

5.3.4.3 The calculation for the total power

Adding Equation (5.23) and Equation (5.29), we can calculate the total power obtained from the piezo and the pyro.

$$P = P_{piezo} + P_{pyro}$$

$$\text{P} = 8 \left(\frac{\pi-2\beta}{2\pi}\right) f_{piezo} \frac{\alpha_{piezo}^2}{C_0} u_M^2 + 4\, f_{pyro} \frac{\alpha_{pyro}^2}{C_0} [\sin(\beta)^2] T_M^2 \tag{5.30}$$

$$\text{P} = [\left(\frac{\pi-2\beta}{2\pi}\right) + \frac{f_{pyro} \alpha^2_{pyro\ [\sin(\beta)]^2 T_M^2}}{f_{piezo} \alpha_{piezo}^2 u_M^2}] 4 f_{piezo} \frac{\alpha_{piezo}^2}{C_0} u_M^2 \tag{5.31}$$

Using the ratio of open-circuit voltage (r_V) and frequency (r_f), we obtain:

$$r_V = \frac{\alpha_{Pyro} T_M}{\alpha_{Piezo} u_M} \tag{5.32}$$

$$r_f = \frac{f_{pyro}}{f_{piezo}} \tag{5.33}$$

$$P = \left[\left(\left(\frac{\pi-2\beta}{2\pi}\right) + {r_V}^2 r_f\ [\sin(\beta)]^2 \right) \right]] 4 f_{piezo} \tag{5.34}$$

5.4. Simulation Results

The model has been implemented in MATLAB in order to investigate the efficiency of the circuit based on SECE technique for investigating the pyroelectric, piezoelectric, open circuit hybrid and hybrid SECE energy harvesting where the hydrid SECE represents the switching at the maxima for the pyroelectric at the open circuit condition. We observed that the system was able to harvest around 0.8 mJ depicted in Figure 5.5 and approximately 10 Volts DC voltage shown in Figure 5.6.

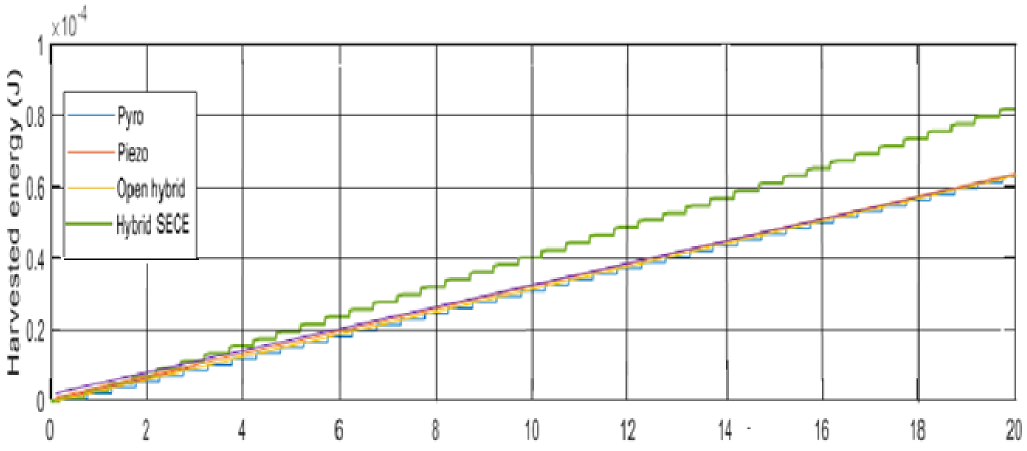

Figure 5. 5 Harvested Energy for Piezo, Pyro, hybrid, hybrid open and hybrid SECE system.

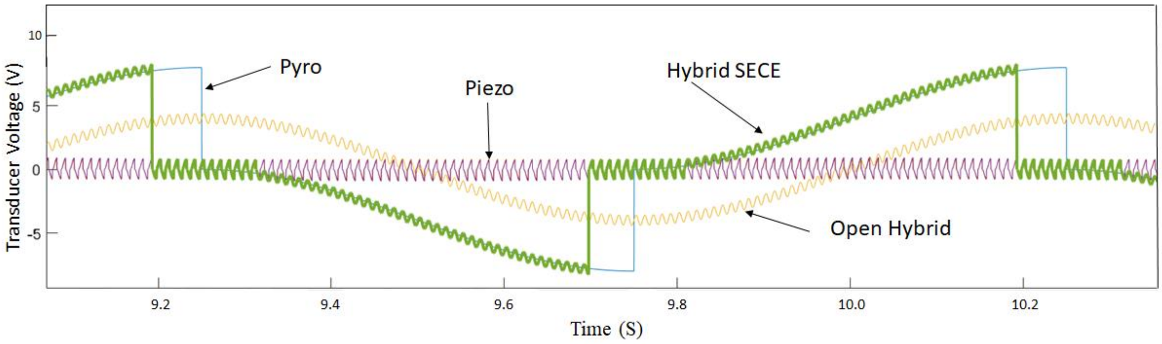

Figure 5. 6 Harvested voltage for Piezo, Pyro, and hybrid SECE and open hybrid system.

In general, the circuit simulation results on PEH performance with the SECE shows a promising result. The PEH simulations with various couplings and vibrating at resonance or off-resonance frequencies were investigated and the outcomes of the SECE circuit's applicability is presented. As shown above, the results work on the two different frequencies, where pyro is more than the piezo as we depicted in the simulated solution.

5.5 Conclusion

In this work, we worked on a non- linear technique for energy extraction approach called SECE, working on different frequencies. The circuit was based on event switching technique allowing to maximize the harvested energy from the thermal and vibrational sources that exhibited frequencies that are not the same. The circuit was afterwards implemented in MATLAB and simulated which demonstrated that it can indeed work with more than one frequency.

From the simulations, we conclude that the lost power from using the SECE circuit is about 15.7%, which is very interesting against the lost power from standard circuit (24.8%). Such loss of power from SECE is reasonable.

When the PEH is excited at the resonance frequency, simulation shows that the power is four times than the optimal power from a standard circuit when the electromechanical coupling is weak. However, the efficiency of the SECE can be dramatically reduced and become lower than that of the standard circuit if the coupling of the PEH is strong. When the PEH vibrates at a different frequency than the structure resonance frequency, simulation predicts that the power with the SECE circuit can be significantly improved compared to the power with the standard circuit. However, it is important to mention that due to some difficulties in the fabrication of the device the implementation of the circuit was not possible and can be investigated in near future

6. Conclusions and future work

This final chapter summarises the results and contributions of this research. Future work is suggested based on the current results. Finally, publications are given.

6.1 Conclusions

This research focused on a hybrid thermal energy harvesting approach using piezo- and pyro-electric effects. First, the research presented a novel hybrid piezoelectric-pyroelectric energy harvester using a cantilever beam with a lead-free material lithium niobate without any tip mass. The cantilever is moving between two surfaces with different temperatures under external vibration. Lithium Niobate single crystal is used as the piezoelectric material, which also has pyroelectric characteristics. Using the pyroelectric effect and the piezoelectric one, the Lithium Niobate output RMS voltage was enhanced up to 10% under 30°C ΔT. The study begins with a review of energy harvesting concentrating on state-of-the-art thermal energy harvesting. This approach was designed to harvest more than two energy sources to improve output performance and to have a simple structure. The initial prototype was presented as a cantilever consisting of a shape memory alloy, a lead-free piezoelectric and pyroelectric material layer. And both the output for the piezo response and the pyro response of the prototypes were presented. We also introduced a new prototype PEH which can work for a broad range frequencies domain and shown promising results.

After that, the coupled piezoelectric and pyroelectric effects were studied for the same prototypes. The heat transferred from the heat source determines two effects. The thermal behaviour was simulated by the finite element method using COMSOL multiphysics. To increase piezoelectricity by raising the mechanical load, two magnets with like-poles facing each other were used to achieve a more excellent piezoelectric response of the beam as the pyroelectric response was dominating the piezoelectric response in low frequency.

Furthermore, a new concept has been introduced for hybrid piezoelectric, pyroelectric energy harvesting based on the Joules Thomson effect and working at a constant temperature. Keeping in mind the real-time scenario, the concept of the device is presented here along with the FEA simulation results, which shows that if an automobile temperature reaches a constant value. There will be no pyroelectric energy harvesting is possible even then with these devices. We can create an artificial environment that will be able to create a temperature gradient for eight hours. A model has been successfully established. The dimensions of the prototype were investigated to increase the output power.

And at last, we proposed to exploit an electrical circuit by which we can condition the output of hybrid energy harvesters and supply sensors in automobiles. Here we focused on the pyroelectric and piezoelectric inputs studied in the previous chapters. Since these effects work on two very different frequencies, the exploited electrical circuit is a non-linear technique called SECE. An analytical model of the electrical circuit has been established and implemented in MATLAB for simulation which validated the efficiency of the circuit to harvest energies from two different sources.

6.2 Contributions

This work's contribution is a simple beam-shaped structure for hybrid harvesting using a shape memory alloy metallic beam, piezoelectric and pyroelectric material. Many studies on the fabrication of the material for hybrid harvesting, but not on the mechanisms. This work concluded several points to utilize both piezo- and pyro- electric effects from the experiments and analysis. First, this work suggested the individual output response for both the piezo and pyro effect based on lead-free materials. A new concept design was introduced for piezoelectric energy harvester works on multi resonant frequencies. For the first time, a concept is given for hybrid energy harvesting based on constant temperature conditions using only lead-free materials. In addition to the prototypes, a model was built to analyze this mechanism. Analysis of this structure has not been done yet. We proposed a new approach to evaluate the output performance of the prototypes based on the non-linear technique. Consequently, this research gives guidelines for the mechanism.

6.3 Future Work

In this study, the hybrid thermal harvesting mechanism was proposed, and prototypes were presented. Besides, the principle of the mechanism represented by comprehensive modelling has been proven. However, further investigations can be performed, such as: i) temperature conditions of the heat source, ii) other materials' parameters, iii) fabrication for the closed system, and iv) implementation of the electrical circuit. The following suggestions may improve low output power, which is a drawback of the current mechanism.

1. **Thermodynamic stud**y. To improve heat exchange, intensive research on

thermodynamics is required. Simulations on thermal behavior have been conducted via FEM but have not been studied in various conditions and situations. Thermodynamics could be considered together with the environment in which this mechanism is applied.

2. **Heat source**. One heat element was used in this research. However, the heat source has various variables, such as size, temperature range, the frequency of the temperature changes, or irregular temperature fluctuations. It is expected that more interesting results will be obtained at different temperature conditions, for example, near the Curie temperature of the ferroelectric material.

3. **Materials study**. Commercially available shape memory alloy and Lead-free Lithium niobate, and PVDF were purchased and used. Other lead-free materials can also be used to investigate the performance of the device. However, the properties of the material have a significant impact on the output performance of the mechanism. In terms of the pyroelectric material, the pyroelectric coefficient must be greater than the piezoelectric one for materials like Lithium tantalate can also be explored.
4. **Multiple beam structures**. Single beams structures were tested here. Multiple beams structure can also be studied.
5. **Circuit design**. This thesis has presented a non-linear technique concept that works on two different frequencies. The implementation is a future perspective.

Bibliography

[1] G. D. Abowd and E. D. Mynatt, 'Charting past, present, and future research in ubiquitous computing', *ACM Trans. Comput.-Hum. Interact.*, vol. 7, no. 1, pp. 29–58, Mar. 2000, doi: 10.1145/344949.344988.

[2] 'Energy Harvesting and the Internet of Things', *Green Inf. Technol.*, pp. 151–160, Jan. 2015, doi: 10.1016/B978-0-12-801379-3.00009-7.

[3] 'ITN Enhance Project - project overview'. https://www.itn-enhance.com/enhance (accessed Feb. 03, 2021).

[4] R. Ahmed, F. Mir, and S. Banerjee, 'A review on energy harvesting approaches for renewable energies from ambient vibrations and acoustic waves using piezoelectricity', *Smart Mater. Struct.*, vol. 26, no. 8, p. 085031, Aug. 2017, doi: 10.1088/1361-665X/aa7bfb.

[5] M. R. Shaikh, S. Shaikh, S. Waghmare, S. Labade, and A. Tekale, 'A Review Paper on Electricity Generation from Solar Energy', *Int. J. Res. Appl. Sci. Eng. Technol.*, vol. 887, Sep. 2017, doi: 10.22214/ijraset.2017.9272.

[6] J. Baeyens, 'Waste Energy Harvesting: Mechanical and Thermal Energies. By Ling Bing Kong, Tao Li, Huey Hoon Hng, Freddy Boey, Tianshu Zhang, and Sean Li', *Energy Technol.*, vol. 3, no. 7, pp. 790–790, 2015, doi: https://doi.org/10.1002/ente.201500113.

[7] R. A. Kishore and S. Priya, 'A Review on Low-Grade Thermal Energy Harvesting: Materials, Methods and Devices', *Materials*, vol. 11, no. 8, Aug. 2018, doi: 10.3390/ma11081433.

[8] N. Nguyen and K. Pochiraju, 'Behavior of thermoelectric generators exposed to transient heat sources', *Appl. Therm. Eng.*, vol. 51, pp. 1–9, Mar. 2013, doi: 10.1016/j.applthermaleng.2012.08.050.

[9] C. R. Bowen, J. Taylor, E. LeBoulbar, D. Zabek, A. Chauhan, and R. Vaish, 'Pyroelectric materials and devices for energy harvesting applications', *Energy Environ. Sci.*, vol. 7, no. 12, pp. 3836–3856, Nov. 2014, doi: 10.1039/C4EE01759E.

[10] N. Jaziri, A. Boughamoura, J. Müller, B. Mezghani, F. Tounsi, and M. Ismail, 'A comprehensive review of Thermoelectric Generators: Technologies and common applications', *Energy Rep.*, vol. 6, pp. 264–287, Dec. 2020, doi: 10.1016/j.egyr.2019.12.011.

[11] S. Buzzi, C. I, T. E. Klein, H. V. Poor, C. Yang, and A. Zappone, 'A Survey of Energy-Efficient Techniques for 5G Networks and Challenges Ahead', *IEEE J. Sel. Areas Commun.*, vol. 34, no. 4, pp. 697–709, Apr. 2016, doi: 10.1109/JSAC.2016.2550338.

[12] S. Watson *et al.*, 'Future emerging technologies in the wind power sector: A European perspective', *Renew. Sustain. Energy Rev.*, vol. 113, p. 109270, Oct. 2019, doi: 10.1016/j.rser.2019.109270.

[13] 'PM277.pdf'. Accessed: Feb. 04, 2021. [Online]. Available: https://spie.org/samples/PM277.pdf.

[14] D. Hoffmann, A. Willmann, R. Göpfert, P. Becker, B. Folkmer, and Y. Manoli, 'Energy Harvesting from Fluid Flow in Water Pipelines for Smart Metering Applications', *J. Phys. Conf. Ser.*, vol. 476, p. 012104, Dec. 2013, doi: 10.1088/1742-6596/476/1/012104.

[15] G. Despesse, J. Chaillout, S. Boisseau, and C. Jean-Mistral, 'Mechanical Energy Harvesting', *Energy Auton. Micro Nano Syst.*, pp. 115–151, Jan. 2013, doi: 10.1002/9781118561836.ch5.

[16] A. Rahman and M. Hoque, *Harvesting Energy from Sound and Vibration*. 2013.

[17] S. Anton and H. Sodano, 'A Review of Power Harvesting Using Piezoelectric Materials (2003-2006)', *Smart Mater. Struct.*, vol. 16, p. R1, May 2007, doi: 10.1088/0964-1726/16/3/R01.

[18] H. Pan, H. Li, T. Zhang, A. A. Laghari, Z. Zhang, and B. Qian, 'A portable renewable

wind energy harvesting system integrated S-rotor and H-rotor for self-powered applications in high-speed railway tunnels', *Energy Convers. Manag.*, vol. 196, pp. 56–68, May 2019, doi: 10.1016/j.enconman.2019.05.115.

[19] H. Sharma, A. Haque, and Z. Jaffery, 'Solar energy harvesting wireless sensor network nodes: A survey', Jan. 2018.

[20] G.-M. Sung, C.-K. Chung, Y.-J. Lai, and J.-Y. Syu, 'Small-Area Radiofrequency-Energy-Harvesting Integrated Circuits for Powering Wireless Sensor Networks', *Sensors*, vol. 19, p. 1754, Apr. 2019, doi: 10.3390/s19081754.

[21]J. C. Rodriguez, V. Nico, and J. Punch, 'A Vibration Energy Harvester and Power Management Solution for Battery-Free Operation of Wireless Sensor Nodes', *Sensors*, vol. 19, no. 17, Art. no. 17, Jan. 2019, doi: 10.3390/s19173776.

[22] P. K. Sharma and P. V. Baredar, 'Analysis on piezoelectric energy harvesting small scale device – a review', *J. King Saud Univ. - Sci.*, vol. 31, no. 4, pp. 869–877, Oct. 2019, doi: 10.1016/j.jksus.2017.11.002.

[23] H. Li, C. Tian, and Z. D. Deng, 'Energy harvesting from low frequency applications using piezoelectric materials', *Appl. Phys. Rev.*, vol. 1, no. 4, p. 041301, Nov. 2014, doi: 10.1063/1.4900845.

[24] H. Fu, G. Chen, and N. Bai, 'Electrode Coverage Optimization for Piezoelectric Energy Harvesting from Tip Excitation', *Sensors*, vol. 18, p. 804, Mar. 2018, doi: 10.3390/s18030804.

[25] D. Upadrashta and Y. Yang, 'Trident-Shaped Multimodal Piezoelectric Energy Harvester', *J. Aerosp. Eng.*, vol. 31, no. 5, p. 04018070, Sep. 2018, doi: 10.1061/(ASCE)AS.1943-5525.0000899.

[26] J. A. Paradiso and T. Starner, 'Energy scavenging for mobile and wireless electronics', *IEEE Pervasive Comput.*, vol. 4, no. 1, pp. 18–27, Jan. 2005, doi: 10.1109/MPRV.2005.9.

[27] C. Sun, G. Shang, and H. Wang, 'On Piezoelectric Energy Harvesting from Human Motion', *J. Power Energy Eng.*, vol. 07, pp. 155–164, Jan. 2019, doi: 10.4236/jpee.2019.71008.

[28] R. Meier, N. Kelly, O. Almog, and P. Chiang, 'A piezoelectric energy-harvesting shoe system for podiatric sensing', *2014 36th Annu. Int. Conf. IEEE Eng. Med. Biol. Soc.*, 2014, doi: 10.1109/EMBC.2014.6943668.

[29] P. Smalser, 'Power transfer of piezoelectric generated energy', US5703474A, Dec. 30, 1997.

[30] M. Kimura, 'Piezo-electricity generation device', Sep. 01, 1998.

[31]S. P. Beeby, M. J. Tudor, and N. M. White, 'Energy harvesting vibration sources for microsystems applications', *Meas. Sci. Technol.*, vol. 17, no. 12, pp. R175–R195, Dec. 2006, doi: 10.1088/0957-0233/17/12/R01.

[32] P. D. Mitcheson, T. C. Green, E. M. Yeatman, and A. S. Holmes, 'Architectures for Vibration-Driven Micropower Generators', *J. Microelectromechanical Syst.*, vol. 13, no. 3, pp. 429–440, Jun. 2004, doi: 10.1109/JMEMS.2004.830151.

[33] N. Toit, 'Modeling and design of a MEMS piezoelectric vibration energy harvester /', Mar. 2006.

[34] S. Roundy, P. K. Wright, and K. S. J. Pister, 'Micro-Electrostatic Vibration-to-Electricity Converters', in *Microelectromechanical Systems*, New Orleans, Louisiana, USA, Jan. 2002, pp. 487–496, doi: 10.1115/IMECE2002-39309.

[35] L. L. Baranowski, G. Jeffrey Snyder, and E. S. Toberer, 'Response to "Comment on 'Effective thermal conductivity in thermoelectric materials'" [J. Appl. Phys. 113, 204904 (2013)]', *J. Appl. Phys.*, vol. 115, no. 12, p. 126102, Mar. 2014, doi: 10.1063/1.4869140.

[36] R. A. Kishore, D. Singh, R. Sriramdas, A. J. Garcia, M. Sanghadasa, and S. Priya, 'Linear thermomagnetic energy harvester for low-grade thermal energy harvesting', *J. Appl. Phys.*, vol. 127, no. 4, p. 044501, Jan. 2020, doi: 10.1063/1.5124312.

[37] J. M. D. Coey, *Magnetism and Magnetic Materials*. Cambridge: Cambridge University Press, 2010.

[38] L. Carlioz, J. Delamare, and S. Basrour, 'Temperature threshold tuning of a thermal harvesting switch', in *transducers 2009 - 2009 International Solid-State Sensors,*

Actuators and Microsystems Conference, Jun. 2009, pp. 1385–1388, doi: 10.1109/SENSOR.2009.5285830.

[39] C.-C. Chen, T.-K. Chung, C.-Y. Tseng, C.-F. Hung, P.-C. Yeh, and C.-C. Cheng, “A miniature magnetic-piezoelectric thermal energy harvester,”IEEE Trans. Magn., vol. 51, no.7, p. 9100309, 2015.

[40] J. Chun, H.-C. Song, M.-G. Kang, H. B. Kang, R. A. Kishore, and S. Priya, ‘Thermo-Magneto-Electric Generator Arrays for Active Heat Recovery System’, *Sci. Rep.*, vol. 7, no. 1, Art. no. 1, Feb. 2017, doi: 10.1038/srep41383.

[41]M. Gueltig *et al.*, ‘High-Performance Thermomagnetic Generators Based on Heusler Alloy Films’, *Adv. Energy Mater.*, vol. 7, no. 5, p. 1601879, 2017, doi: https://doi.org/10.1002/aenm.201601879.

[42] O. Puscasu *et al.*, ‘Flexible bimetal and piezoelectric based thermal to electrical energy converters’, *Sens. Actuators Phys.*, vol. 214, pp. 7–14, Aug. 2014, doi: 10.1016/j.sna.2014.03.027.

[43] D. Zakharov *et al.*, ‘Thermal energy conversion by coupled shape memory and piezoelectric effects’, *J. Micromechanics Microengineering*, vol. 22, no. 9, p. 094005, Aug. 2012, doi: 10.1088/0960-1317/22/9/094005.

[44] S. Hunter, N. Lavrik, T. Bannuru, S. Mostafa, S. Rajic, and P. Datskos, ‘Development of MEMS based pyroelectric thermal energy harvesters’, *Proc SPIE*, vol. 8035, May 2011, doi: 10.1117/12.882125.

[45] S. Ravindran, T. Huesgen, M. Kroener, and P. Woias, ‘A self-sustaining micro thermomechanic-pyroelectric generator’, *Appl. Phys. Lett. - APPL PHYS LETT*, vol. 99, Sep. 2011, doi: 10.1063/1.3633350.

[46] ‘Steven Percy, Chris Knight, Scott McGarry, Alex Post, Tim Moore, and Kate Cavanagh. Thermal to Electrical Energy Converters. SpringerBriefs in Electrical and Computer Engineering. Springer New York, 2014. ISBN 978-1-4614-9214-6. doi:10.1007/978-1-4614- 9215-3. - Google Search’.

[47] ‘3A Thermoelectric Cooler (TEC) Driver - Electronics-Lab.com’. https://www.electronics-lab.com/project/3a-thermoelectric-cooler-tec-driver/ (accessed Feb. 04, 2021).

[48] Z. Tian, S. Lee, and G. Chen, ‘A Comprehensive Review of Heat Transfer in Thermoelectric Materials and Devices’, *Annu. Rev. Heat Transf.*, vol. 17, Jan. 2014, doi: 10.1615/AnnualRevHeatTransfer.2014006932.

[49] G. Sebald, S. Pruvost, and D. Guyomar, ‘Energy Harvesting Based on Ericsson Pyroelectric Cycles in a Relaxor Ferroelectric Ceramic’, *Smart Mater. Struct.*, vol. 17, p. 015012, Dec. 2007, doi: 10.1088/0964-1726/17/01/015012.

[50] R. W. Whatmore, ‘Pyroelectric devices and materials’, *Rep. Prog. Phys.*, vol. 49, no. 12, pp. 1335–1386, Dec. 1986, doi: 10.1088/0034-4885/49/12/002.

[5] C. Bowen, H. A. Kim, P. Weaver, and S. Dunn, ‘Piezoelectric and Ferroelectric Materials and Structures for Energy Harvesting Applications’, *Energy Environ. Sci.*, vol. 7, p. 25, Jan. 2014, doi: 10.1039/c3ee42454e.

[52] S. Lang, ‘Pyroelectricity: From Ancient Curiosity to Modern Imaging Tool’, *Phys. Today - PHYS TODAY*, vol. 58, pp. 31–36, Aug. 2005, doi: 10.1063/1.2062916.

[53] R. B. Olsen, D. A. Bruno, and J. M. Briscoe, ‘Pyroelectric conversion cycles’, *J. Appl. Phys.*, vol. 58, no. 12, pp. 4709–4716, Dec. 1985, doi: 10.1063/1.336244.

[54] R. B. Olsen, J. M. Briscoe, D. A. Bruno, and W. F. Butler, ‘A pyroelectric energy converter which employs regeneration’, *Ferroelectrics*, vol. 38, no. 1, pp. 975–978, Oct. 1981, doi: 10.1080/00150198108209595.

[55] R. Kandilian, A. Navid, and L. Pilon, ‘The pyroelectric energy harvesting capabilities of PMN–PT near the morphotropic phase boundary’, *Smart Mater. Struct.*, vol. 20, pp. 55020–10, Apr. 2011, doi: 10.1088/0964-1726/20/5/055020.

[56] ‘4.1 – Transportation and Energy | The Geography of Transport Systems’. https://transportgeography.org/contents/chapter4/transportation-and-energy/ (accessed Feb. 04, 2021).

[57] S. Roundy, P. K. Wright, and J. M. Rabaey, *Energy Scavenging for Wireless Sensor*

Networks: with Special Focus on Vibrations. Springer US, 2004.
[58] P. D. Mitcheson and T. C. Green, ‘Maximum Effectiveness of Electrostatic Energy Harvesters When Coupled to Interface Circuits’, *IEEE Trans. Circuits Syst. Regul. Pap.*, vol. 59, no. 12, pp. 3098–3111, Dec. 2012, doi: 10.1109/TCSI.2012.2206432.
[59] Y. Suzuki, ‘Electrostatic/Electret-Based Harvesters’, in *Micro Energy Harvesting*, John Wiley & Sons, Ltd, 2015, pp. 149–174.
[60] R. Aljadiri, L. Taha, and P. Ivey, ‘Electrostatic Energy Harvesting Systems: A Better Understanding of Their SustainabilityElectrostatic Energy Harvesting Systems: A Better Understanding of Their Sustainability’, *J. Clean Energy Technol.*, vol. 5, pp. 409–416, Sep. 2017, doi: 10.18178/JOCET.2017.5.5.407.
[61] S. Boisseau, G. Despesse, and B. Ahmed, ‘Electrostatic Conversion for Vibration Energy Harvesting’, in *Small-Scale Energy Harvesting*, M. Lallart, Ed. InTech, 2012.
[62] ‘IoT Solution - Wuhan linptech Co., Ltd.’ http://www.energyharvesting.cn/en/iotsolution/ (accessed Mar. 14, 2021).
[63] C. Saha, T. O’Donnell, N. Wang, and P. Mccloskey, ‘C. R. Saha, T. O’Donnell, N. Wang and P. McCloskey, “Electromagnetic generator harvesting energy from human motion”, Sensors and Actuators – A: Physical, volume 147, Issue 1, 2008’, *Sens. Actuators Phys.*, vol. 147, Sep. 2008, doi: 10.1016/j.sna.2008.03.008.
[64] P. D. Mitcheson, T. C. Green, and E. M. Yeatman, ‘Power processing circuits for electromagnetic, electrostatic and piezoelectric inertial energy scavengers’, *Microsyst. Technol.*, vol. 13, no. 11, pp. 1629–1635, Jul. 2007, doi: 10.1007/s00542-006-0339-0.
[65] X. Wang, S. V. Palagummi, L. Liu, and F.-G. Yuan, ‘A magnetically levitated vibration energy harvester’, *Smart Mater. Struct.*, vol. 22, p. 055016, Apr. 2013, doi: 10.1088/0964-1726/22/5/055016.
[66] S. P. Beeby *et al.*, ‘A micro electromagnetic generator for vibration energy harvesting’, *J. Micromechanics Microengineering*, vol. 17, no. 7, pp. 1257–1265, Jul. 2007, doi: 10.1088/0960-1317/17/7/007.
[67] ‘Paul-Jacques Curie - Wikipedia’. https://en.wikipedia.org/wiki/Paul-Jacques_Curie (accessed Mar. 14, 2021).
[68] ‘IEEE Standard on Piezoelectricity’, *ANSI/IEEE Std 176-1987*, p. 0_1-, 1988, doi: 10.1109/IEEESTD.1988.79638.
[69] E. Hoummadi, M. Safaei, and S. Anton, *Design, analysis, and fabrication of a piezoelectric force plate*. 2017.
[70] A. Erturk and D. J. Inman, ‘An experimentally validated bimorph cantilever model for piezoelectric energy harvesting from base excitations’, *Smart Mater. Struct.*, vol. 18, no. 2, p. 025009, Jan. 2009, doi: 10.1088/0964-1726/18/2/025009.
[71] F. Goldschmidtboeing and P. Woias, ‘Characterization of different beam shapes for piezoelectric energy harvesting’, *J. Micromechanics Microengineering*, vol. 18, p. 104013, Sep. 2008, doi: 10.1088/0960-1317/18/10/104013.
[72] ‘Cantilevered Piezoelectric Energy Harvester With a Dynamic Magnifier | Energy Harvesting | Piezoelectricity’, *Scribd*. https://www.scribd.com/document/247779301/Cantilevered-Piezoelectric-Energy-Harvester-With-a-Dynamic-Magnifier (accessed Feb. 04, 2021).
[73] J. C. Park and J. Y. Park, ‘Asymmetric PZT bimorph cantilever for multi-dimensional ambient vibration harvesting’, *Ceram. Int.*, vol. Supplement 1, no. 39, pp. S653–S657, 2013, doi: 10.1016/j.ceramint.2012.10.155.
[74] J. Xu, Y. Liu, W. Shao, and Z. Feng, ‘Optimization of a right-angle piezoelectric cantilever using auxiliary beams with different stiffness levels for vibration energy harvesting’, *Smart Mater. Struct. - SMART MATER STRUCT*, vol. 21, Jun. 2012, doi: 10.1088/0964-1726/21/6/065017.
[75] D.- Lee, G. P. Carman, D. Murphy, and C. Schulenburg, ‘Novel Micro Vibration Energy Harvesting Device using Frequency Up Conversion’, in *TRANSDUCERS 2007 - 2007 International Solid-State Sensors, Actuators and Microsystems Conference*, Jun. 2007, pp. 871–874, doi: 10.1109/SENSOR.2007.4300269.
[76] S.-M. Jung and K.-S. Yun, ‘Energy-harvesting device with mechanical frequency-up

conversion mechanism for increased power efficiency and wideband operation', *Appl. Phys. Lett.*, vol. 96, no. 11, p. 111906, Mar. 2010, doi: 10.1063/1.3360219.

[77] M. A. Halim and J. Y. Park, 'Theoretical modeling and analysis of mechanical impact driven and frequency up-converted piezoelectric energy harvester for low-frequency and wide-bandwidth operation', *Sens. Actuators Phys.*, vol. 208, pp. 56–65, Feb. 2014, doi: 10.1016/j.sna.2013.12.033.

[78] T. Galchev, E. E. Aktakka, and K. Najafi, 'A Piezoelectric Parametric Frequency Increased Generator for Harvesting Low-Frequency Vibrations', *J. Microelectromechanical Syst.*, vol. 21, no. 6, pp. 1311–1320, Dec. 2012, doi: 10.1109/JMEMS.2012.2205901.

[79] M. Wild, M. Bring, E. Halvorsen, L. Hoff, and K. Hjelmervik, 'The challenge of distinguishing mechanical, electrical and piezoelectric losses', *J. Acoust. Soc. Am.*, vol. 144, no. 4, pp. 2128–2134, Oct. 2018, doi: 10.1121/1.5057443.

[80] 'Lead zirconate titanate', *Wikipedia*. Dec. 27, 2020, Accessed: Feb. 04, 2021. [Online]. Available: https://en.wikipedia.org/w/index.php?title=Lead_zirconate_titanate&oldid=996564604.

[81] J.-H. Lee *et al.*, 'Highly stretchable piezoelectric-pyroelectric hybrid nanogenerator', *Adv. Mater. Deerfield Beach Fla*, vol. 26, no. 5, pp. 765–769, Feb. 2014, doi: 10.1002/adma.201303570.

[82] Y. Chen, Y. Zhang, F. Yuan, F. Ding, and O. Schmidt, 'A Flexible PMN-PT Ribbon-Based Piezoelectric-Pyroelectric Hybrid Generator for Human-Activity Energy Harvesting and Monitoring', *Adv. Electron. Mater.*, vol. 3, p. 1600540, Feb. 2017, doi: 10.1002/aelm.201600540.

[83] M.-H. You *et al.*, 'A self-powered flexible hybrid piezoelectric–pyroelectric nanogenerator based on non-woven nanofiber membranes', *J. Mater. Chem. A*, vol. 6, no. 8, pp. 3500–3509, Feb. 2018, doi: 10.1039/C7TA10175A.

[84] B. Gusarov *et al.*, 'Thermal energy harvesting by piezoelectric PVDF polymer coupled with shape memory alloy', *Sens. Actuators Phys.*, vol. 243, pp. 175–181, Jun. 2016, doi: 10.1016/j.sna.2016.03.026.

[85] M.-K. Kim, M.-S. Kim, S. Lee, C. Kim, and Y.-J. Kim, 'Wearable thermoelectric generator for harvesting human body heat energy', *Smart Mater. Struct.*, vol. 23, p. 105002, Sep. 2014, doi: 10.1088/0964-1726/23/10/105002.

[86] Y. Zhang *et al.*, 'Enhanced pyroelectric and piezoelectric properties of PZT with aligned porosity for energy harvesting applications', *J Mater Chem A*, vol. 5, Apr. 2017, doi: 10.1039/C7TA00967D.

[87] J. Kim *et al.*, 'High-Performance Piezoelectric, Pyroelectric, and Triboelectric Nanogenerators Based on P(VDF-TrFE) with Controlled Crystallinity and Dipole Alignment', *Adv. Funct. Mater.*, Apr. 2017, doi: 10.1002/adfm.201700702.

[88] Y. Tang *et al.*, 'Enhanced pyroelectric and piezoelectric responses in W/Mn-codoped Bi4Ti3O12 Aurivillius ceramics', *J. Eur. Ceram. Soc.*, vol. 38, Aug. 2018, doi: 10.1016/j.jeurceramsoc.2018.08.025.

[89] R. Suhail, J.-F. Chen, G. Amato, and D. McCrum, 'Mechanical behaviour of NiTiNb Shape Memory Alloy Wires– Strain Localisation and Effect of Strain Rate', *Mech. Mater.*, vol. 144, p. 103346, May 2020, doi: 10.1016/j.mechmat.2020.103346.

[90] J.-G. Sun, T.-N. Yang, C.-Y. Wang, and L.-J. Chen, 'A Flexible Transparent One-structure Tribo-Piezo-Pyroelectric Hybrid Energy Generator Based on Bio-inspired Silver Nanowires Network for Biomechanical Energy Harvesting and Physiological Monitoring', *Nano Energy*, vol. 48, Mar. 2018, doi: 10.1016/j.nanoen.2018.03.071.

[91] Y. Ji, K. Zhang, and Y. Yang, 'A One-Structure-Based Multieffects Coupled Nanogenerator for Simultaneously Scavenging Thermal, Solar, and Mechanical Energies', *Adv. Sci.*, vol. 5, Dec. 2017, doi: 10.1002/advs.201700622.

[92] T. Ding *et al.*, 'Hybrid Photothermal Pyroelectric and Thermogalvanic Generator for Multisituation Low Grade Heat Harvesting', *Adv. Energy Mater.*, vol. 8, Oct. 2018, doi: 10.1002/aenm.201802397.

[93] B. Orr, A. Akbarzadeh, M. Mochizuki, and R. Singh, ‘A review of car waste heat recovery systems utilising thermoelectric generators and heat pipes’, *Appl. Therm. Eng.*, vol. 101, Nov. 2015, doi: 10.1016/j.applthermaleng.2015.10.081.

[94] L. Van Minh, M. Hara, and H. Kuwano, *High performance nonlinear micro energy harvester integrated with (K, Na)NbO3/Si composite quad-cantilever*. 2014.

[95] ‘Potassium–Sodium Niobate Lead-Free Piezoelectric Materials: Past, Present, and Future of Phase Boundaries | Chemical Reviews’. https://pubs.acs.org/doi/10.1021/cr5006809 (accessed Feb. 05, 2021).

[96] A. Bartasyte, S. Margueron, T. Baron, S. Oliveri, and P. Boulet, ‘Toward High-Quality Epitaxial LiNbO 3 and LiTaO 3 Thin Films for Acoustic and Optical Applications’, *Adv. Mater. Interfaces*, vol. 4, p. 1600998, Mar. 2017, doi: 10.1002/admi.201600998.

[97] J. Hong, W. Yan, Y. Ma, D. Zhang, and X. Yang, ‘Experimental investigation on the vibration tuning of a shell with a shape memory alloy ring’, *Smart Mater. Struct.*, vol. 24, p. 105007, Sep. 2015, doi: 10.1088/0964-1726/24/10/105007.

[98] M. Senthilkumar . M. G. Vasundhara . G. K. Kalavathi 'Electromechanical analytical model of shape memory alloy based tunable cantilevered piezoelectric energy harvester doi.org/10.1007/s10999-018-9413-x.

[99] H. Li, C. Tian, and Z. Deng, ‘Energy harvesting from low frequency applications using piezoelectric materials’, *Appl. Phys. Rev.*, vol. 1, p. 041301, Dec. 2014, doi: 10.1063/1.4900845.

[100] N. Sezer and M. Koç, ‘A comprehensive review on the state-of-the-art of piezoelectric energy harvesting’, *Nano Energy*, vol. 80, p. 105567, Feb. 2021, doi: 10.1016/j.nanoen.2020.105567.

[101] A. A. Arevalo Carreno and I. Foulds, *Parametric Study of Polyimide – Lead Zirconate Titanate Thin Film Cantilivers for Transducer Applications*. 2013.

[102] G.-Y. Kim *et al.*, ‘Effect of Thickness Ratio in Piezoelectric/Elastic Cantilever Structure on the Piezoelectric Energy Harvesting Performance’, *Electron. Mater. Lett.*, vol. 15, no. 1, pp. 61–69, Jan. 2019, doi: 10.1007/s13391-018-00103-w.

[103] r. Xu and s. G. Kim, ‘figures of merits of piezoelectric materials in energy harvesters’.

[104] R. Waser, U. Bottger, and S. Tiedke, Polar Oxides: Properties, Characterization, and Imaging. John Wiley & Sons, 2006, ch. 3.

[105] M. Stewart, M. G. Cain, and D. A. Hall, Ferroelectric Hysteresis Measurement & Analysis. Teddington: National Physical Laboratory, 1999.

[106] A. Benyahia and R. Bouamrane, ‘Investigation of the dielectric response of binary disordered systems modelled as random resistor–capacitor networks’, *Indian J. Phys.*, vol. 94, no. 12, pp. 1895–1900, Dec. 2020, doi: 10.1007/s12648-019-01642-0.

[107] c. Maurini, ‘electromechanical coupling of distributed piezoelectric transducers for passive damping of structural vibrations: comparison of network configurations’.

[108] A.Almori and Ashok Batra Experimental and modelling study of a piezoelectric energy harvesters unimorph cantilever arrays.

[109] K. Mohamed, H. Elgamal, and S. A. Kouritem, ‘An experimental validation of a new shape optimization technique for piezoelectric harvesting cantilever beams’, *Alex. Eng. J.*, vol. 60, no. 1, pp. 1751–1766, Feb. 2021, doi: 10.1016/j.aej.2020.11.024.

[110] P. Pillatsch, E. Yeatman, and A. Holmes, ‘Magnetic plucking of piezoelectric beams for frequency up-converting energy harvesters’, *Smart Mater. Struct.*, vol. 23, Jan. 2014, doi: 10.1088/0964-1726/23/2/025009.

[111] B. Wang, J. Zhao, and S. Zhou, ‘A micro scale Timoshenko beam model based on strain gradient elasticity theory’, *Eur. J. Mech. -Solids - EUR J MECH -SOLID*, vol. 29, pp. 591–599, Jul. 2010, doi: 10.1016/j.euromechsol.2009.12.005.

[112] M. Kang and E. M. Yeatman, ‘Coupling of piezo- and pyro-electric effects in miniature thermal energy harvesters’, *Appl. Energy*, vol. 262, p. 114496, Mar. 2020, doi: 10.1016/j.apenergy.2020.114496.

[113] C. Chang, V. H. Tran, J. Wang, Y.-K. Fuh, and L. Lin, ‘Direct-write piezoelectric polymeric nanogenerator with high energy conversion efficiency’, *Nano Lett.*, vol. 10, no. 2, pp. 726–731, Feb. 2010, doi: 10.1021/nl9040719.

[114] ‘Joule–Thomson effect’, *Wikipedia*. Dec. 06, 2020, Accessed: Feb. 05, 2021. [Online]. Available: https://en.wikipedia.org/w/index.php?title=Joule%E2%80%93Thomson_effect&oldid=992619984.

[115] S. Boisseau *et al.*, ‘Synchronous Electric Charge Extraction for multiple piezoelectric energy harvesters’, in *2015 IEEE 13th International New Circuits and Systems Conference (NEWCAS)*, Jun. 2015, pp. 1–4, doi: 10.1109/NEWCAS.2015.7182103.

[116] D. Guyomar, A. Badel, E. Lefeuvre, and C. Richard, ‘Toward energy harvesting using active materials and conversion improvement by nonlinear processing’, *IEEE Trans. Ultrason. Ferroelectr. Freq. Control*, vol. 52, no. 4, pp. 584–595, Apr. 2005, doi: 10.1109/TUFFC.2005.1428041.

[117] M. Lallart and D. Guyomar, ‘An optimized self-powered switching circuit for non-linear energy harvesting with low voltage output’, *Smart Mater. Struct.*, vol. 17, no. 3, p. 035030, May 2008, doi: 10.1088/0964-1726/17/3/035030.

[118] F. Dell’Anna *et al.*, ‘State-of-the-Art Power Management Circuits for Piezoelectric Energy Harvesters’, *IEEE Circuits Syst. Mag.*, 2018, doi: 10.1109/MCAS.2018.2849262.

[119] L. Tang and Y. Yang, ‘Analysis of synchronized charge extraction for piezoelectric energy harvesting’, *Smart Mater. Struct.*, vol. 20, no. 8, p. 085022.

[120] E. Brusa, S. Zelenika, L. Moro, and D. Benasciutti, *Analytical characterization and experimental validation of performances of piezoelectric vibration energy scavengers*. 2009.

[121] E. Lefeuvre, A. Badel, C. Richard, D. Guyomar and L. Petit *A comparison between several vibrational-powered piezoelectric generators for standalone systems* Sensors and Actuators A 126 (2006) 405–416.

[122] A. Badel, E. Lefeuvre, C. Richard, D. Guyomar and L. Petit Piezoelectric Energy Harvesting using a Synchronized Switch. Journal of Intelligent Material Systems and Structures 2006 17: 831DOI: 10.1177/1045389X06057533

Titre: Contribution au développement de récupérateurs d'énergie hybrides thérmo-vibrationnels.

Mots clefs : Piézoélectrique, vibrationnel, thermique, récupération d'énergie

Résumé : Autour de nous, il existe de nombreuses énergies ambiantes qui seront “perdues” si elles ne sont pas récupérées ni exploitées. Parmi celles-ci, l’énergie issue des vibrations mécaniques et l’énergie thérmique sont parmi les plus répandues car leurs sources sont partout : moteurs de véhicules, marches d’une personne, rayon soleil, etc. Tandis que récupérer de manière individuelle de l’énergie de vibrations et de l’énergie thérmique et les transformer en énergie électrique ont donné lieu à une littérature assez remplie, leur récupération et transformation de manière simultanée et avec le même dispositif sont très peu étudiées.

Dans le cadre du projet européen ITN-ENHANCE (Piezoelectric Energy Harvesters for Self-Powered Automotive Sensors: from Advanced Lead-Free Materials to Smart Systems), cette thèse se focalise sur l’étude et le développement de récupérateurs d’énergie de vibrations mécaniques et d’énergie thérmique de manière simultanée et avec les mêmes dispositifs. Appelés dispositifs hybrides de récupération d’énergie, ceux-ci sont à base de matériaux piézoélectriques Niobate de Lithium leur permettant d’avoir la particularité de ne pas être toxiques car sans plomb. Dédiés pour l’alimentation de capteurs autonomes dans les voitures, les défis incluent la faible fréquence des vibrations ainsi que la faible amplitude et la lenteur des fluctuations thérmiques. Les travaux de cette thèse incluent l’étude et le développement de dispositifs en tentant de prendre en compte ces défis, leurs modélisations et simulation, et leurs expérimentations.

Title: Contribution to the design and development of hybrid Thermal-Vibrational Piezoelectric Energy Harvester

Keywords: Piezoelectric, Vibrational, Thermal, Energy Harvesting,

Abstract: There are several ambient energies in our surroundings, most of which could be “lost” if not scavenged or exploited. Among them, vibrational energy and thermal energy are two of the most widespread ones as their sources are everywhere: engines in cars, walking persons, solar rays, and so on. While scavenging vibrational and thermal energies individually and transforming them into electrical ones have raised many works in the literature, harvesting them simultaneously and with the same single device has provided very few results.

Within the European ITN-ENHANCE project (Piezoelectric Energy Harvesters for Self-Powered Automotive Sensors: from Advanced Lead-Free Materials to Smart Systems), this thesis focuses on the study and development of energy harvesting devices able to simultaneously or individually capture ambient vibrational and thermal energies and converting them into electrical one by using the same harvester device and element.

Called hybrid thermal vibrational energy harvesters, the devices are based on Lithium Niobate piezoelectric materials allowing them to be lead-free and non-toxic. Devoted to power autonomous sensors in vehicles, the challenges faced include the low vibrational frequency as well as the low amplitude and slow temperature fluctuations. The thesis works include studying and developing several designs of hybrid energy harvesters, their modeling, simulation, fabrication, and experimental results.

University Bourgogne Franche-Comté
32, avenue de l'Observatoire
25000 Besançon